Experimental constraints on the real part of the ω-nucleus optical potential

Inaugural-Dissertation
zur Erlangung des Doktorgrades der Naturwissenschaften (Dr. rer. nat.)
der Justus-Liebig-Universität Gießen
im Fachbereich 07
(Mathematik und Informatik, Physik, Geographie)

Juni 2014

vorgelegt von

Stefan Friedrich

aus Lollar

II. Physikalisches Institut
Justus-Liebig-Universität Gießen
Heinrich-Buff-Ring 16
35392 Gießen
Deutschland

Dekan:	Prof. Dr. Peter Jens Klar
Prodekan:	Prof. Dr. Ingo Liefner

Betreuer und 1. Gutachter:	Prof. Dr. Volker Metag
2. Gutachter:	Prof. Dr. Claudia Höhne
3. Prüfer:	Prof. Dr. Ulrich Mosel
4. Prüfer:	Prof. Dr. Stefan Schippers

Tag der mündlichen Prüfung:	07. Juli 2014

Abstract

The existence of a bound pion-nucleus system has been experimentally demonstrated by embedding negatively charged pions in different nuclei. These bound systems are formed by the interplay of the Coulomb and strong interaction. In this thesis the possible formation of ω-mesic states was investigated which are governed solely by the strong interaction since the ω-meson is electrically neutral.

At the electron stretcher ELSA at Bonn the photoproduction of ω-mesons on a liquid hydrogen as well as on a carbon target has been studied for incident photon energies of 1250 - 3110 MeV. The combined setup of the Crystal Barrel and the MiniTAPS detector systems, which form a 4π electromagnetic calorimeter, was used for detecting the possible ω-mesic state via the $\omega \rightarrow \pi^0 + \gamma$ decay mode. The recoiling proton of the γ + p $\rightarrow$ ω + p reaction was identified with an aerogel-threshold-Čerenkov detector in veto-mode and the forward angle spectrometer MiniTAPS, exploiting the characteristic correlation between deposited energy and time-of-flight for protons. Measurements on liquid hydrogen are used as a reference for understanding background reactions and studying systematic uncertainties. Several kinematical cuts have been applied to reduce the background which mainly stems from $\pi^0\pi^0$- and $\pi^0\eta$-production where one of the four decay photons escaped detection.

The kinematics of the reaction channel and the detector acceptance have been calculated based on Monte Carlo simulations. Different incident photon energies, diverse target materials as well as the Fermi momentum of the nucleons in a carbon nucleus have been considered.

Structures in the total energy distribution of the $\pi^0\gamma$-pairs, which would indicate the population and decay of bound ω^{11}B states, are not observed. The differential $\pi^0\gamma$-cross section of 0.3 nb/MeV/sr found in the bound state energy regime between -100 and 0 MeV may be accounted for by yield leaking into the bound state regime be-

cause of the large in-medium width of the ω-meson.
Theoretical predictions exist only for the formation of quantum-mechanical states of ω-mesic nuclei and for quasi-free ω-production. Both, decay and possible final state interaction of the decay products have to be considered for a direct comparison to experimental data. Therefore, calculations with the Giessen Boltzmann-Uehling-Uhlenbeck transport model (GiBUU) have been performed to determine the effective branching ratio of an ω-mesic state into the $\pi^0\gamma$-channel. It turns out that the kinetic energy distribution of the ω-mesons is sensitive to the depth of the optical potential, even in the quasi-free region. Depending on its real part, the peak position is shifted: For an attractive ω-nucleus interaction the ω-meson is slowed down, while for a repulsive interaction the kinetic energy of the ω-meson is increased. A comparison of the measured total energy distribution with calculations, extending into the regime of quasi-free ω-production, suggests the real part V_0 of the optical meson-nucleus potential to be small and only weakly attractive with $V_0(\rho = \rho_0)$ = -15 $\pm$ 35 (stat) $\pm$ 20 (syst) MeV in contrast to several theoretical predictions of attractive potentials with a depth of 100 - 150 MeV.

Zusammenfassung

Die Existenz von gebundenen Pion-Kern-Zuständen wurde durch das Einbringen von negativ geladenen Pionen in verschiedene Atomkerne experimentell nachgewiesen. Diese gebundenen Systeme werden durch die Überlagerung von Coulomb- und starker Wechselwirkung gebildet. In dieser Arbeit wurde die mögliche Bildung von ω-mesischen Zuständen untersucht, welche nur durch die starke Wechselwirkung gebunden werden, da das ω-Meson elektrisch neutral ist.
An der Elektronen-Stretcher-Anlage (ELSA) in Bonn wurde die Photoproduktion von ω-Mesonen sowohl an flüssigem Wasserstoff als auch an Kohlenstoff als Target für einen Einschussenergiebereich von 1250 - 3110 MeV untersucht. Der kombinierte Aufbau des Crystal Barrel und des MiniTAPS Detektor-Systems, welche zusammen ein 4π elektromagnetisches Kalorimeter bildet, wurde zum Nachweis eines möglichen ω-mesischen Zustands im Zerfallskanal $\omega \rightarrow \pi^0 + \gamma$ benutzt. Das Rückstoßproton der Reaktion γ + p $\rightarrow \omega$ + p wurde mithilfe eines Aerogel-Schwellen-Čerenkov-Detektors im Veto-Betrieb im Vorwärtsspektrometer MiniTAPS nachgewiesen, wobei die charakteristische Korrelation zwischen deponierter Energie und Flugzeit für Protonen ausgenutzt wurde. Die Messungen am flüssigen Wasserstoff werden als Referenz für das Verständnis der Untergrund-Reaktionen und für die Bestimmung der systematischen Unsicherheiten verwendet. Verschiedene kinematische Schnitte wurden angewendet, um den Untergrund zu reduzieren, der hauptsächlich von der $\pi^0\pi^0$- und $\pi^0\eta$-Produktion stammt, wobei eines der vier Zerfallsphotonen nicht nachgewiesen wird.
Die Kinematik des Reaktionskanals und die Detektorakzeptanz wurden unter Zuhilfenahme von Monte-Carlo-Simulationen berechnet. Verschiedene Einschussenergien, verschiedene Target-Materialien sowie der Fermi-Impuls der Nukleonen in einem Kohlenstoffatomkern wurden berücksichtigt.

Es wurden keine Strukturen in der Gesamtenergieverteilung der $\pi^0\gamma$-Paare beobachtet, die auf eine Bevölkerung und Zerfall von ω^{11}B-Zuständen hindeuten. Der gemessene $\pi^0\gamma$-Wirkungsquerschnitt von 0,3 nb/MeV/sr im Bereich der gebundenen Zustände von -100 bis 0 MeV kann einer Ausbeute, die in diesen Bereich der gebundenen Zustände hineinreicht, zugeschrieben werden, da die in-Medium-Breite des ω-Mesons sehr groß ist.
Theoretische Vorhersagen existieren nur für die Bildung von quantenmechanischen Zuständen von ω-mesischen Kernen und für quasi-freie ω-Produktion. Da der Zerfall und eine mögliche Endzustandswechselwirkung der Zerfallsprodukte für einen direkten Vergleich mit experimentellen Daten berücksichtigt werden müssen, wurden Rechnungen mit dem Gießen Boltzmann-Uehling-Uhlenbeck Transportmodell (GiBUU) durchgeführt, um das effektive Verzweigungsverhältnis eines ω-mesischen Zustands in den $\pi^0\gamma$-Kanal zu bestimmen. Es stellt sich heraus, dass die kinetische Energieverteilung der ω-Mesonen auch im quasi-freien Bereich empfindlich auf die Tiefe des optischen Potentials ist. Abhängig von dessen Realteil ist die Position des Maximums verschoben: Für eine anziehende ω-Kern-Wechselwirkung werden die ω-Mesonen verlangsamt, während für eine abstoßende Wechselwirkung die kinetische Energie des ω-Mesons erhöht ist. Ein Vergleich der gemessenen Verteilung der Gesamtenergie mit Berechnungen, die sich in den Bereich der quasi-freien Produktion erstrecken, legt einen kleinen Realteil V_0 des optischen Meson-Kern-Potentials nahe und ist somit nur schwach anziehend mit $V_0(\rho = \rho_0)$ = -15 $\pm$ 35 (stat) $\pm$ 20 (syst) MeV. Dies steht im Gegensatz zu einigen theoretischen Vorhersagen eines attraktiven Potentials mit einer Tiefe von 100 - 150 MeV.

Contents

List of Figures

List of Tables

Chapter 1

Introduction

This chapter provides an overview of the Standard Model of elementary particles and its consequences for the dynamics of composite objects like mesons. Furthermore the interaction of hadrons will be described and the effects of the nuclear medium on meson properties. At the end theoretical predictions will be discussed that will be used for the interpretation of the experimental results of this work.

1.1 The Standard Model

The Standard Model of elementary particles consists of 37 particles[1] and integrates three out of four fundamental interactions in nature (fundamental forces). Gravitation, which for humans is - together with the electromagnetic interaction - the most common force to experience in daily life, cannot be explained within the framework of this model.
Gravitation can be described by Albert Einstein's theory of general relativity as curvature of the four-dimensional space-time. It is the reason why masses attract each other and for example planetary systems are formed. On the macroscopic scales in our universe gravitation is by far the predominant force, although on smaller scales it is the weakest! The gravitational force between two protons is only a fraction of

[1]6 quarks + 6 leptons and their anti-particles = 24 particles; 4 electro-weak exchange bosons + 8 gluons = 12 exchange bosons; 1 Higgs-boson

10^{-36} of the electromagnetic repulsion between the two particles. This is the reason why the impact of gravitation can be neglected in particle physics and on the other hand why it is so difficult to measure quantum physical effects of gravitation.
In order to unify all four fundamental forces to one theory of everything the combination of gravitation with quantum physics remains a challenge. This issue becomes very important for the description of physics on very small scales and very high energies.
A quantum-field theory of the electromagnetic interaction was formulated by Feynman, Schwinger and Tomonaga in 1949. This quantum electrodynamics (QED) describes the interaction of electrically charged particles by the exchange of (virtual) photons, the quanta of light. Processes of higher order are the reason of phenomena like the Lamb-shift of atomic energy levels. QED is by now the most precise theory in physics because experimental and theoretically predicted results agree excellently.
The other two fundamental forces of nature are the so called strong and weak force.
For example, the strong interaction is the reason for the binding of nucleons to an atomic nucleus. The elementary constituents of nucleons are the quarks[2]. There are six types of them, but only the two lightest ones contribute to normal matter in the universe. The exchange bosons of this force are the gluons[3]. Without any rest mass, they mediate the strong force between particles carrying color charge. This charge was first introduced into the quark model to fulfill the Pauli principle for all bound systems of quarks (hadrons). The three colors are called red, green and blue. Antiparticles carry anti-colors.
So far, only composite particles have been observed which are colorless ("white"), e.g. the sum of all color charges is white. The gluons themselves also carry color charge, a combination of a color and an anti-color, that is not white. Eight possible combinations of that kind exist. This property leads to a strong self-interaction among gluons that has consequences for the dynamics of quarks. In analogy to QED the quantum-field theory of the strong interaction is called quantum chromodynamics[4] (QCD). Particles consisting out of (anti-)quarks and underlying the strong interaction

[2]The name "quark" originates from a phrase in "Finnegans Wake" by James Joyce: "Three quarks for Muster Mark!"
[3]From English, "glue"
[4]From Greek, "chromos": color

Interaction	Acts on	Exchange boson	Mass [GeV/c^2]
strong	color charge	8 gluons (g)	0
electromagnetic	electrical charge	photon (γ)	0
weak	weak charge	$W^{\pm}$, Z^0	80.4, 91.2
weak		Higgs-boson H^0	125.9

Table 1.1: The interactions of the Standard Model and their exchange bosons [1, 2].

Fermions	Family			Electromagnetic charge [e]	Color charge
Leptons	e	μ	τ	-1	-
	ν_e	ν_μ	ν_τ	0	-
Quarks	up	charm	top	$+\frac{2}{3}$	r, g, b
	down	strange	bottom	$-\frac{1}{3}$	r, g, b

Table 1.2: The fermions of the Standard Model. For each particle there exits an anti-particle with opposite electromagnetic and color charge [1].

are called hadrons. Objects consisting out of three (anti-)quarks are baryons, objects built from a quark anti-quark pair are mesons.

The weak interaction describes the conversion of particles, for example the β-decay of radioactive nuclides. The exchange bosons are the $W^{\pm}$ and the Z^0, which have a rather large rest mass compared to the other elementary particles (see table 1.1). Due to that fact their interaction range is very small. By Heisenberg's uncertainty principle it is about 10^{-2} fm. The weak and electromagnetic interaction can be unified to the electro-weak force, first described by Weinberg and Salam in 1967.

The last elementary particle which was experimentally discovered in 2012 is the Higgs-boson whose coupling to all other fundamental particles gives them their rest mass. Predicted in the 1960's, it required a long experimental effort to produce and detect it.

In general all particles of the Standard Model are fermions (see table 1.2), e.g. particles with a half-integral spin. The exchange particles (see table 1.1) are bosons, e.g. particles with integer spin.

Meson	Mass [MeV/c^2]	Natural width	$c \cdot \tau$	Charge	J^P	I	Quark content
π^0	134.98	7,72 eV	25.5 nm	0	0^-	1	$\frac{1}{\sqrt{2}}\left(u\bar{u} - d\bar{d}\right)$
$\pi^\pm$	139.57	$25.3 \cdot 10^{-9}$ eV	7.80 m	± 1	0^-	1	$(u\bar{d}, d\bar{u})$
η	547.85	1.30 keV	152 pm	0	0^-	0	$\frac{1}{\sqrt{6}}\left(u\bar{u} + d\bar{d} - 2s\bar{s}\right)$
ρ^0, $\rho^\pm$	775	149 MeV	1.3 fm	0, ± 1	1^-	1	$\frac{1}{\sqrt{2}}\left(u\bar{u} - d\bar{d}\right), (u\bar{d}, d\bar{u})$
ω	782.65	8.49 MeV	23.5 fm	0	1^-	0	$\frac{1}{\sqrt{2}}\left(u\bar{u} + d\bar{d}\right)$

Table 1.3: Properties of selected light mesons [1, 3]. The value $c\tau$, the product of lifetime and the speed of light, is a measure for the flight distance before decay. J represents the quantum number of the total spin, P of the parity and I of the isospin.

1.2 Hadrons and their interactions

Under the condition of being colorless, many hadrons can be comprised from quarks whose effective masses are much higher than the bare quark masses. Qualitatively this dynamically generated mass can be explained by the relativistic motion of the quarks and the energy stored within the gluon field. Because of the amount of combinations of quarks with different spin combinations, orbital momentum, isospin etc. a variety of hadronic resonances is known. Via mathematical group theory these mesons and baryons can be ordered in multiplets according to a given spin and intrinsic parity. Within these multiplets, the hadrons are ordered according to their quark content (isospin, strangeness, charm,...). In that way Gell-Mann and Ne'eman could predict the existence and the mass of the Ω^--baryon in 1961. Figure 1.1 shows two examples of multiplets for mesons and baryons, each.

To investigate these excitations one often measures the decay products of these baryons and mesons. Knowing certain rules of conservation of quantities (orbital momentum, parity,..), one can reconstruct the original resonance. Often a simple reconstruction of the invariant mass identifies the hadron, if the mass is known, the width is relatively small and all decay products can be measured. Tables 1.3 and 1.4 give an overview of the properties of some light mesons and baryons, respectively.

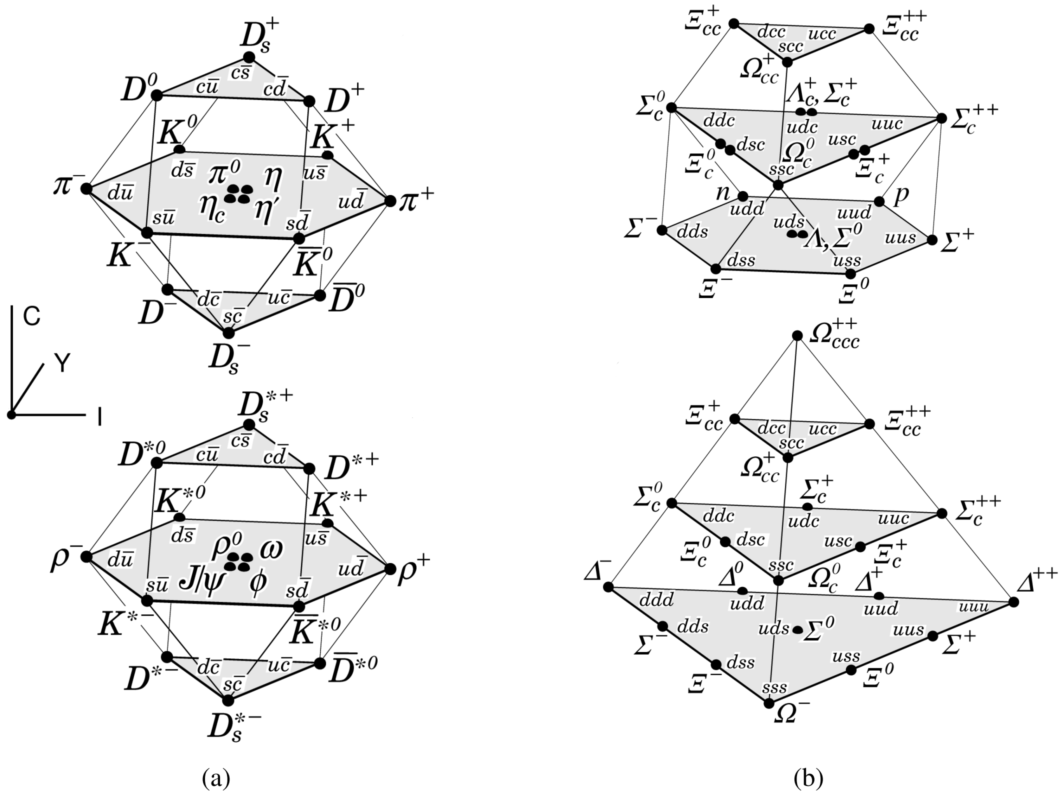

Figure 1.1: (a) Hexadecuplets of pseudoscalar and vector mesons. On the I-, C-, Y-axes the isospin component I_z, the charm quark content C and the hypercharge Y=B+S-C/3 are shown, respectively. (b) Multiplets of baryons. [1]

Baryon	Mass [MeV/c^2]	Natural width	$c \cdot \tau$	Charge	J^P	I	Quark content
proton	938.27	-	∞	+1	$\frac{1}{2}^+$	$\frac{1}{2}$	uud
neutron	939.57	$747 \cdot 10^{-21}$ eV	$264 \cdot 10^6$ km	0	$\frac{1}{2}^+$	$\frac{1}{2}$	udd
N^+(1535) S_{11}	≈1535	≈150 MeV	1.31 fm	+1	$\frac{1}{2}^-$	$\frac{1}{2}$	uud
Δ^{++}	≈1232	≈117 MeV	1.68 fm	+2	$\frac{3}{2}^+$	$\frac{3}{2}$	uuu

Table 1.4: Properties of selected light baryons [1, 3]. The value $c\tau$, the product of the lifetime and the speed of light, is a measure for the flight distance before its decay. J represents the quantum number of the total spin, P of the parity and I of the isospin.

1.2.1 Chiral symmetry

Helicity describes the orientation of the spin of a particle relatively to the direction of its momentum:

$$H = \frac{\vec{s} \cdot \vec{p}}{\mid \vec{s} \mid \mid \vec{p} \mid} \tag{1.1}$$

The chirality is a fundamental symmetry of QCD in the limit of vanishing quark masses. For massless particles, the helicity can be only H = ± 1 and is then equal to chirality. Fermions can be right-handed (spin and momentum pointing to the same direction) or left-handed (spin and momentum pointing to the opposite direction). Gluons do not distinguish between left- and right-handed particles, thus they do not change helicity. If the particles are massless, their chirality cannot be changed, it is conserved.

However even the light quarks (u, d, s) have non-zero rest masses. At small particle masses, the chiral symmetry is an approximate symmetry. This means, that as long as the masses are small compared to the relevant scale of the theory (the energy scale of the QCD, $\Lambda_{QCD} \approx 200\,\mathrm{MeV}$), the prediction under the assumption of the symmetry should be reasonably close to the actual results. The masses of the lightest three quarks fulfill this requirements [1]:

$$\frac{m_u c^2}{\Lambda_{QCD}} \approx 1.5 \cdot 10^{-2}, \frac{m_d c^2}{\Lambda_{QCD}} \approx 2.5 \cdot 10^{-2}, \frac{m_s c^2}{\Lambda_{QCD}} \approx 5 \cdot 10^{-1} \tag{1.2}$$

If the same symmetry were to hold in the hadronic sector the chiral partners linked by the parity transformation should be degenerate in mass: m_{J^+} = m_{J^-} (due to the approximate behavior the masses should have small differences). This is not observed in nature (see figure 1.2). The mass differences between chiral partners in the hadronic sector are not negligible, but even of the same order as the mass of the hadrons. This directly shows that chiral symmetry is spontaneously broken within the hadronic sector.

A symmetry is spontaneously broken if the symmetry of the Hamiltonian is not realized in the ground state of the system. The features are illustrated in figure 1.3. For this type of a potential, the symmetry is spontaneously broken by choosing a cer-

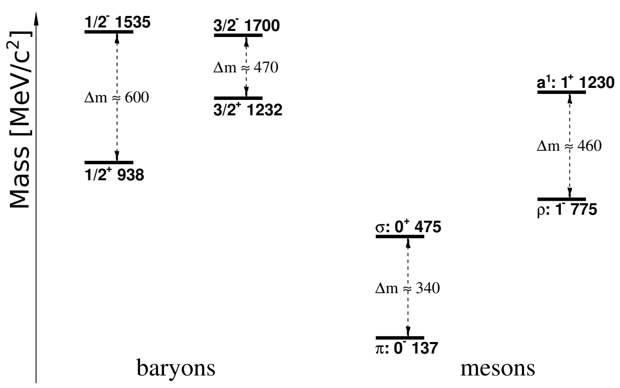

Figure 1.2: Masses of selected hadrons and their chiral partners (not to scale) [1]. The mass-split between the chiral partners is comparable to the masses of the hadrons.

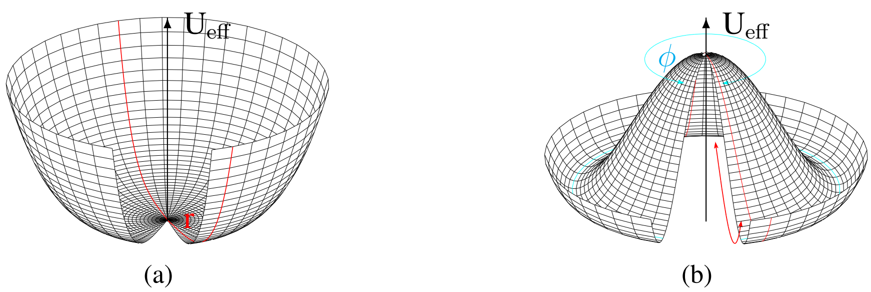

Figure 1.3: In figure (a) (restored symmetry), the minimum of the potential is in the center, therefore the ground state is invariant under rotation (no spontaneous breaking of the symmetry), while in figure (b) (spontaneously broken symmetry) the ground state is located at a finite distance from the center where the potential actually has a local minimum. The red lines represent the radial excitation, the cyan line the rotational mode. [4]

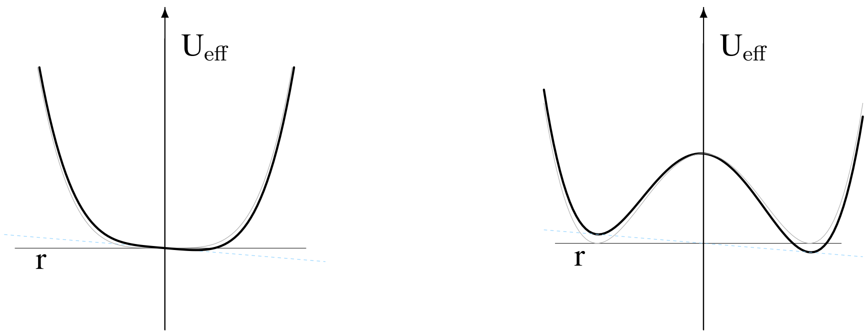

(a) (b)

Figure 1.4: Explicit breaking of the chiral symmetry. The thin gray line represents the symmetric Lagrangian. The thin cyan line shows the explicit symmetry breaking term ($-m\overline{\phi_q}\phi_q$), the black line is the full Lagrangian. [4]

tain direction to realize the ground state. However, an effect of the symmetry is still present. Moving around the valley costs no energy, whereas radial motion involves the change of kinetic to potential energy. An important consequence of the spontaneously broken symmetry is the existence of a massless mode (rotational mode), the so called Goldstone boson of the broken symmetry. In QCD - if only the two lightest quarks (u, d) are considered - the pion-triplet (π^+, π^-, π^0) is identified as Goldstone bosons. Generally, it is assumed that the QCD-Hamiltonian at zero temperature has a similar form as in figure 1.3(b) where the r and ϕ coordinates are replaced by σ- (massive) and π- (massless) fields. However, the mass of the pions are not zero. The non-zero masses of the quark can lead to a non-zero mass of the pions by breaking the chiral symmetry explicitly. In contrast to the spontaneous symmetry breaking where the Lagrangian is symmetric, in the case of explicit symmetry breaking the Lagrangian is not symmetric. It means that the Lagrangian of QCD loses its symmetry if a quark mass term is included ($\delta\mathcal{L} = -m\overline{\phi_q}\phi_q$). Using the example above (see figure 1.3), the extra mass term tilts the potential. This is visualized by the cross section of the “Mexican hat” potential (see figure 1.4). In this configuration, the rotational mode (pion field) also costs energy, hence the Goldstone bosons are massive. As long as the potential is tilted only slightly, rotational excitations are considerably smaller than the radial ones, which is also reflected in the small π-masses.
In terms of quark degrees of freedom, one order parameter to measure the violation of chiral symmetry is the chiral condensate that has a value of $\langle q\overline{q}\rangle \approx$ (-250

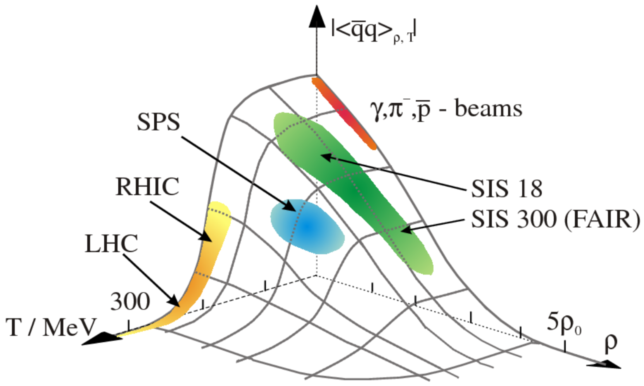

Figure 1.5: Dependence of the chiral condensate on density and temperature. Indicated are the areas where modern accelators can probe the chiral condensate. [5]

MeV)$^3 \pm 10\%$ in vacuum. Another order parameter is the decay constant of the pion which has a value of $f_{\pi^0} \approx 94\,\mathrm{MeV}$ in vacuum . The link between the two quantities is given by the Gell-Mann-Oaks-Renner (GOR) relation:

$$m_{\pi^0}^2 = \frac{1}{f_\pi^2} \cdot \underbrace{\frac{m_u + m_d}{2}}_{\text{explicit symmetry breaking}} \cdot \overbrace{(\langle u\overline{u}\rangle + \langle d\overline{d}\rangle)}^{\text{sponteneous symmetry breaking}} + \mathcal{O}(m_{u,d}^2), \tag{1.3}$$

where f_π is the decay constant of the pion, and $m_{u,d}$ are the quark masses. The right part of the GOR expression carries information on both explicit symmetry breaking through the quark masses and spontaneous breaking of the symmetry through the expression of the chiral condensate $\langle q\overline{q}\rangle$. The order parameter for the chiral symmetry breaking shows dependence on temperature and density. A prediction of this dependence is shown of the figure 1.5.

As it can be seen in figure 1.5, at sufficiently high temperatures (kT $> 200\,\mathrm{MeV}$) the chiral condensate drops suddenly, while with increasing density, the chiral condensate decreases linearly down to zero at to high densities ($\rho \geq 5\rho_0$)[5]. Consequently, the chiral symmetry should at least partially be restored. This effect is not unique in physics. The phase transition of ferromagnets at the Curie point to paramagnetic

[5] ρ_0 is the normal nuclear matter density, $\rho_0 = 0.17/\mathrm{fm}^3$

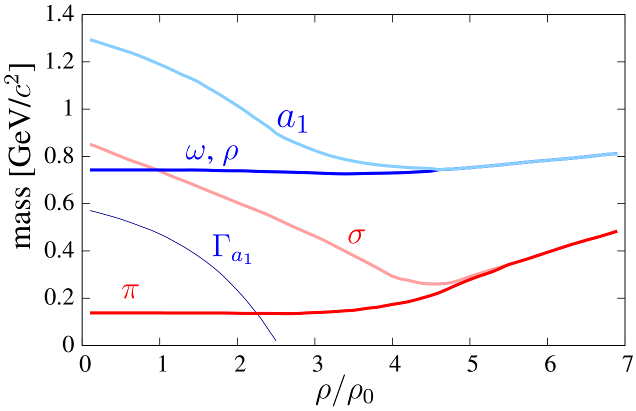

Figure 1.6: Prediction of the NJL model for meson masses as function of density. The decay width $a_1 \rightarrow \bar{q}q$ is also shown. Beyond a critical density the chiral partners (π, σ) and (ρ, a_1) are degenerate in mass. [6]

material is the similar form of transition. But contrary to the magnetism (the order parameter of the transition), the chiral condensate and the decay constant of the pion are not observables. The connection between the order parameter (quark condensate) and hadronic observable (spectral function) is given by the QCD Sum Rules. While a general consensus exists concerning how the chiral condensate behaves in a thermal bath or in a dense medium, the effect of chiral restoration on hadronic observables is much less clear.

1.2.2 In-medium modifications of mesons

There are many models predicting modifications of the properties of mesons in the nuclear medium. Some models and their predictions will be mentioned here.

The constituent quark mass m_q originates mainly from the spontaneous breaking of chiral symmetry as proposed by Nambu and Jona-Lasinio (NJL) [7]. If one assumes that the vector meson mass is just given by the additive rule, then it will be of the order of $2m_q$. As chiral symmetry is restored, the constituent mass drops, therefore a drop in the mass of the vector meson is expected. More elaborate models using the NJL approach at finite temperatures and density were proposed in the late 1980's [6]. It is interesting to note that the masses of the pion and the vector mesons are almost

not changing with density. Mass degeneracy between the σ- and the π-meson, the ρ- and the a_1-meson is reached by a strong mass drop of the σ- and the $_1$-meson in dense matter where chiral symmetry is restored ($\rho \approx 5\rho_0$) (see figure 1.6).
The QCD sum rule method can relate the QCD condensate to the hadronic spectral functions. QCD sum rules in the medium provide useful constraints evaluating the weighted average of the spectral functions. Hatsuda and Lee [8] have predicted that the mass of the vector mesons drops linearly with the density:

$$\frac{m_V^*}{m_V} = \left(1 - \alpha \frac{\rho}{\rho_0}\right), \tag{1.4}$$

where ρ_0 is the normal nuclear density (0.17/fm^3) and $\alpha \approx 0.18 \pm 0.06$ for V = ρ, ω and $\alpha \approx 0.15 \cdot S$ for V = ϕ (S is the nucleon strangeness content). In contrast the Brown-Rho scaling [9] assumes that the masses of light vector mesons (ρ, ω) scale universally as a function of density and/or temperature:

$$\frac{m^*}{m} \sim \frac{f_{\pi^0}^*}{f_{\pi^0}} \sim 0.8(\rho \sim \rho_0) \tag{1.5}$$

The Quark-Meson Coupling model (QMC) is a phenomenological theory in which quarks interact by the exchange of mesons. In the medium, baryons composed of three valence quarks feel both scalar and vector potentials with opposite sign, while the mesons composed of quark and anti-quark only feel the scalar potential and obey a universal scaling law (figure 1.7). It is interesting to note that at normal nuclear density (ρ_0), the ρ- and ω-masses drop by $\approx$15%, the nucleon-mass drops by $\approx 20\%$ and the D-meson mass drops by $\approx 3\%$.

Hadronic models use a purely hadronic description of mesons in the medium. These models provide much "richer" information about the in-medium properties of the mesons. The spectral functions are modified in non-trivial manners such as spectral shifts, spectral broadening and new spectral peaks. The in-medium self-energy of the meson receives contributions from low-energy particle-hole excitations and high energy nucleon-anti nucleon excitations. As it propagates in nuclear matter, the vector meson feels not only the nucleons but also resonance excitations such as Δ and N^*. Figure 1.8 shows the predictions of different hadronic models for the ρ- and

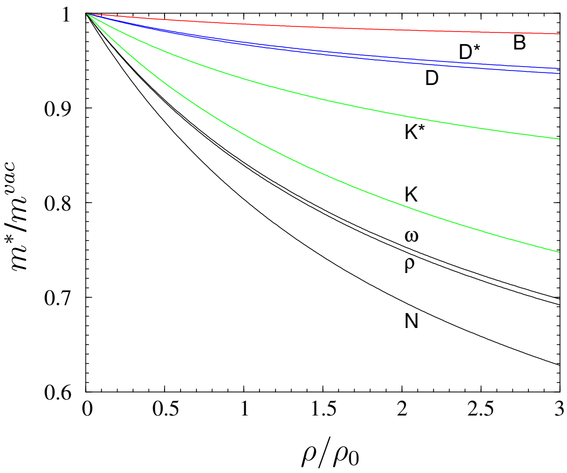

Figure 1.7: Prediction of the QMC model for meson masses as function of density. [10]

ω-mesons inside the nuclear medium at different densities [11].

All these models make measurable predictions even at normal nuclear matter densities (mass shift, broadening, extra peaks, etc.). For now, these effective theories are the best available models until Lattice QCD calculations produce reliable results at finite density and temperature.
On the experimental side, a collisional broadening inside nuclear matter has been observed for the ω-meson [12]. This result has been obtained by measuring the transparency ratio T_A (see equation 1.6) on four different nuclei: ^{12}C, ^{40}Ca, ^{93}Nb, ^{208}Pb.

$$T = \frac{\sigma_{\gamma A \to VX}}{A\sigma_{\gamma N \to VX}} \tag{1.6}$$

To avoid systematic uncertainties when comparing to theoretical models, e.g. due to the unknown ω-production cross section on the neutron or secondary production processes, the transparency ratio has been normalized to carbon data:

$$T = \frac{12\sigma_{\gamma A \to VX}}{A\sigma_{\gamma^{12}C \to VX}} \tag{1.7}$$

In figure 1.9(a) the measured transparency ratio of calcium, niobium and lead as

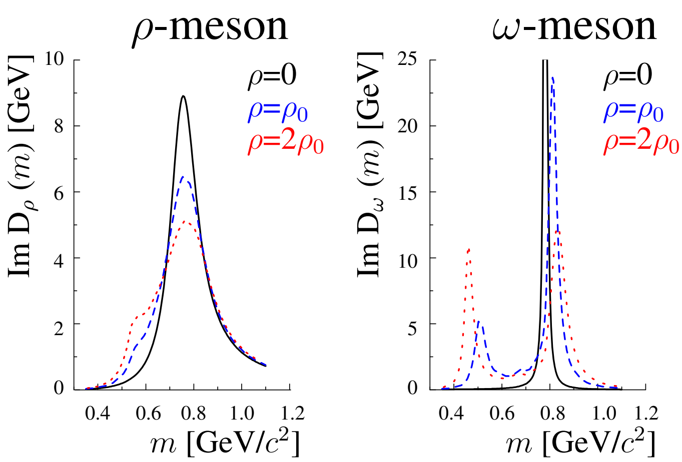

Figure 1.8: Prediction of a hadronic model [11] for the imaginary part of the ρ- and ω-meson spectral functions inside nuclear matter at $\rho = 0$, $\rho = \rho_0$ and $\rho = 2\rho_0$.

function of the mass number A is shown together with Giessen Boltzmann-Uehling-Uhlenbeck transport model calculations (GiBUU, see chapter 6) for different absorption widths Γ at a fixed ω-momentum of 1.1 GeV/c. The comparison yields an in-medium width of 130 - 150 MeV. In figure 1.9(b) the transparency ratio is shown for the three different nuclei as function of the ω-momentum. From the transparency ratio one can determine the inelastic cross section σ_0 as well as the inelastic width Γ_0 at nuclear matter density via a Glauber analysis. In low density approximation, where

$$\Gamma_0(p, \rho) = \Gamma_0(p) \cdot \frac{\rho}{\rho_0} \tag{1.8}$$

holds true, the inelastic cross section and the in-medium width are related by:

$$\Gamma(\rho) = \hbar \cdot c \cdot \beta \cdot \sigma_0 \cdot \rho \tag{1.9}$$

Figure 1.10 shows the result together with theoretical assumptions. The momentum dependence of the in-medium width is very important for the interpretation of experimental results. Theoretical calculations try to model such a dependence. As an example for a hadronic many-body approach figure 1.11 shows the in-medium width as a function of momentum [13].

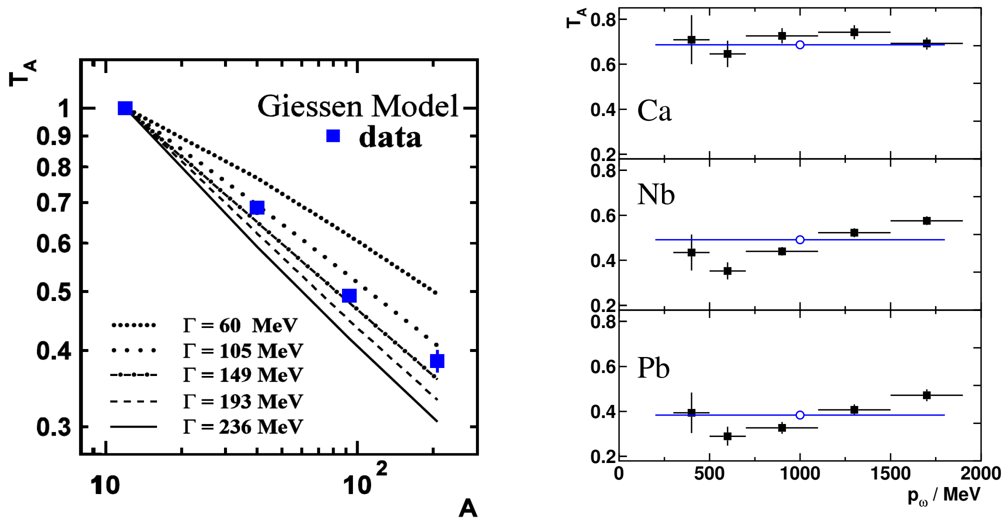

(a) (b)

Figure 1.9: (a) Experimentally determined transparency ratio in comparison with GiBUU calculations for different widths at 1.1 GeV/c ω-momentum. (b) Momentum dependent transparency ratio for three different targets as full squares. The open points show the value for all momenta. [12]

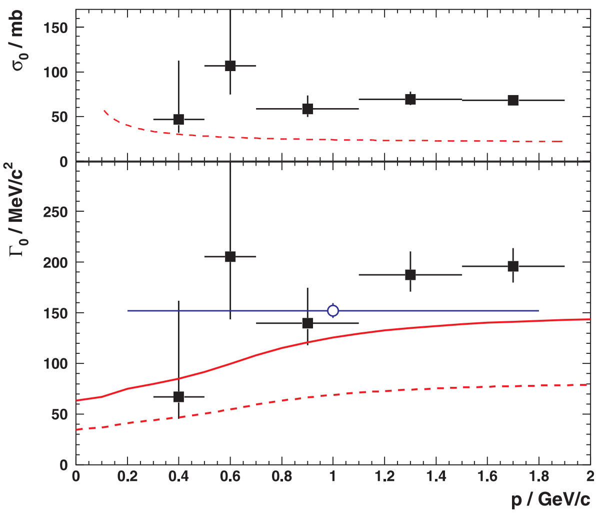

Figure 1.10: Upper part: The inelastic ωN cross section extracted from the Glauber analysis in comparison to the cross section used in GiBUU. Lower part: Measured widths of the ω-meson inside the nuclear medium as a function of the ω-momentum in comparison to the GiBUU model calculations (red dashed line), and after a fit to the data (solid red line). [12]

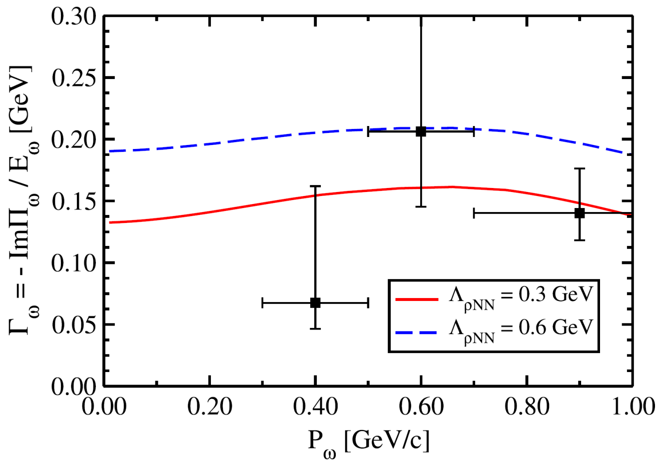

Figure 1.11: Momentum dependence of $\Gamma_{\omega\to\rho\pi}$ at saturation density for on-shell ω-mesons compared to data from [12]. [13]

1.3 Meson-nucleus bound states

Hadrons interact via the strong force and additionally via the electromagnetic force, if they are electrically charged. The lightest and easiest to produce meson is the pion. The negatively charged π^--meson can be bound to an atomic nucleus by replacing an electron in one of the atomic shells. If the meson is captured in a high shell, it will cascade down to lower shells by emitting x-ray photons. Since the higher orbitals do not overlap with the nucleus, only the electromagnetic interaction plays a role. As soon as the populated state has overlap with the nucleus the strong force can lead to an absorption of the meson. To populate these deeply bound states, where electromagnetic and strong interaction are involved, one has to produce the π^--meson directly in these states in order to investigate the pion in-medium properties. Figure 1.12(a) shows the potentials of the two forces as function of the distance to the nucleus for the lead isotope ^{207}Pb. Figure 1.12(b) shows a schematic view of the energy level for negatively charged pions. The attractive electromagnetic potential overlaps with the strong interaction potential which is repulsive for low momentum pions in the s-state. This yields a pocket-like structure leading to a halo-like π^--distribution around the nucleus. These states can be populated by recoilless production, for instance with a pickup reaction ^{208}Pb(d,^{3}He)^{207}Pb. After first experiments on lead isotopes [14, 15] an experiment at the fragment separator at GSI in Darmstadt was performed to mea-

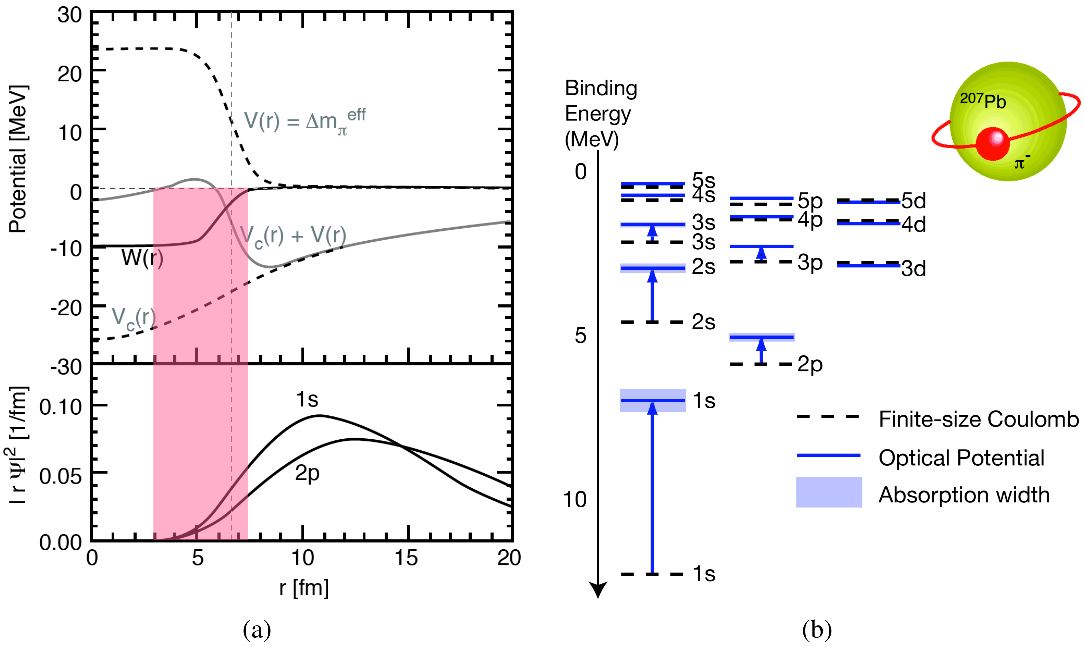

Figure 1.12: (a) Upper panel: Decomposition of the pion-nucleus potential for ^{207}Pb into the Coulomb potential V_C and the real and imaginary s-wave potential $(V,\ W)$ [14, 15]. Lower panel: Pionic density distribution for 1s- and 2p-states. (b) Calculated level scheme of pionic ^{207}Pb. Level shifts and widths are indicated by vertical arrows and shaded areas [17].

sure inclusively deeply bound pionic states on different isotopes [16]. The optical model parameters were determined from energy and width of the bound $(1s)_{\pi^-}$-states. As a result, the first evidence for a lowering of the chiral condensate in the nuclear medium was observed. The widths of these states have been found to be 1/10 of the binding energy which is essential for their experimental observation, since then these states show up as peaks in the energy and mass spectra. Figure 1.13 shows the measured cross sections of these pionic states as function of the kinetic energy of the outgoing Helium nucleus, which is directly related to the excitation energy of the meson-nucleus system. The interesting question arises whether a neutral meson that only interacts strongly can form a meson-nucleus bound state. In the next section theoretical predictions for such an ω-bound state will be discussed.

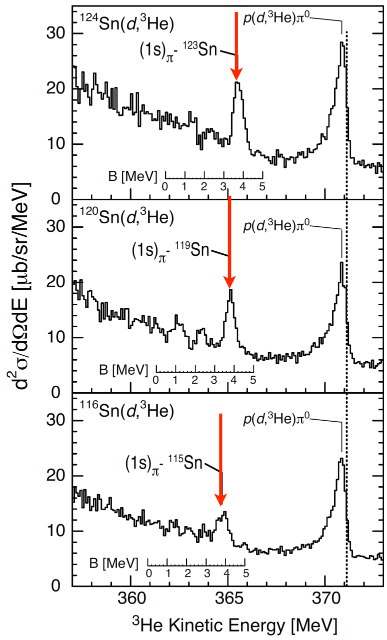

Figure 1.13: Double differential cross section for pionic tin isotopes as function of the kinetic energy of the outgoing Helium nucleus. The arrows indicate the deeply bound pions in the 1s-state. [16]

1.4 Theoretical predictions for ω-mesic nuclei

1.4.1 Predictions by Marco and Weise

The calculation of Marco and Weise was performed using an effective Lagrangian based on chiral SU(3) symmetry and vector meson dominance to construct the ω-nucleus potential. A downward mass shift of 15% and in-medium width of 40 MeV at normal nuclear density was assumed in the calculation. The calculation was performed for the case when the ω-meson is produced at rest in the nucleus. The corresponding photon energy is E_{beam} = 2.75 GeV, the knocked-out proton goes to Θ_p^{lab} = $0°$. The missing energy spectrum,

$$E_\gamma + m_p - E_p - m_\omega = E_\omega - m_\omega + |B_p|, \tag{1.10}$$

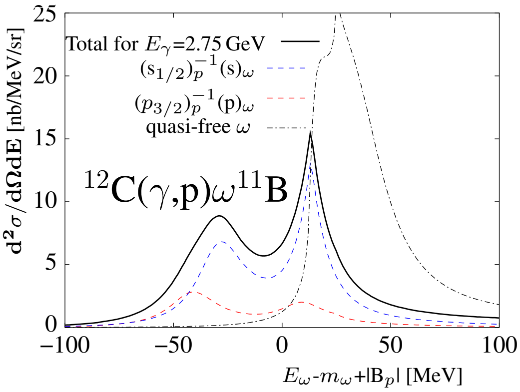

(a)

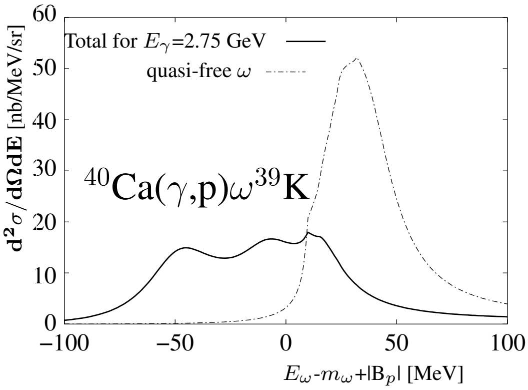

(b)

Figure 1.14: Missing energy spectra at E_γ = 2.75 GeV for the (a) ^{12}C(γ,p)ω^{11}B reaction and (b) for the ^{40}Ca(γ,p)ω^{39}K reaction ($|B_p|$ is the binding energy of the bound initial proton) [19].

for a carbon and a calcium target is shown in figure 1.14. For the carbon target a pronounced peak can be seen at ≈-30 MeV while for the calcium target an access at negative energies without pronounced structure is predicted. These predictions are very similar to the calculations by Nagahiro et al. [18].

1.4.2 Predictions by Nagahiro et al.

Nagahiro et al. [18] use the Green's function method to calculate formation cross sections of the η- and the ω-nucleus systems in photoproduction on a nucleus. The method starts with a separation of the reaction cross section into the nuclear reponse function $S(E)$ and the elementary cross section which is taken from experiment (see equation 1.11, where φ denotes the η- or ω-meson):

$$\left(\frac{d^2\sigma}{d\Omega dE}\right)_{A(\gamma,p)(A-1)\otimes\varphi} = (\frac{d\sigma}{d\Omega})^{lab}_{p(\gamma,p)\varphi} \times S(E) \qquad (1.11)$$

The calculation of the nuclear response function with the complex potential is formulated by Morimatsu and Yzaki [20, 21] in a generic form as equation 1.12 shows:

$$S(E) = -\frac{1}{\pi} \,\mathrm{Im} \sum_f \mathcal{T}_f^\dagger G(E) \mathcal{T}_f \tag{1.12}$$

with

$$\mathcal{T}_f(\vec{r}) = \chi_f^*(\vec{r}) \xi_{1/2,m_s}^* [Y_{l_\varphi}^*(\hat{r}) \otimes \psi_{j_p}(\vec{r})]_{JM} \chi_i(\vec{r}) \tag{1.13}$$

$$G(E;\vec{r},\vec{r}\,') = \langle p^{-1} | \phi_\varphi(\vec{r}) \frac{1}{E - H_\varphi + i\epsilon} \phi_\varphi^\dagger(\vec{r}\,') | p^{-1} \rangle \tag{1.14}$$

The summation runs over all possible final states. The amplitude $\mathcal{T}_f$ denotes the transition of the incident particle to the proton hole and the outgoing ejectile, involving the proton hole wavefunction ψ_{j_p} and the distorted waves χ_i and χ_j of the projectile and ejectile. The appropriate treatment of the spin is shown in equation 1.13 with the meson angular wavefunction $Y_{l_\varphi}(\hat{r})$ and the spin wavefunction $\xi_{1/2,m_s}$ of the ejectile. The Green function $G(E)$ is obtained by solving the Klein-Gordon equation using the meson-nucleus optical potential as shown in equation 1.14. The nuclear reponse S(E) is then obtained by numerical integration.
Calculations for different mesons at a fixed incoming photon energy are shown in figure 1.15 for an attractive (figure 1.15(a)) and a repulsive ω-potential (figure 1.15(b)). One clearly sees that the ω-yield below the free production threshold vanishes in the repulsive case. Only for an attractive potential structures can be seen below threshold. In order to match the experimental conditions to the specific experimental setup described in this work, dedicated calculations were performed [22]. The resulting spectra for ω-mesic states are shown for a potential (V_0, W_0) =(-156, 70) MeV in figure 1.16 and for a potential (V_0, W_0) =(0, 70) MeV in figure 1.17 .

These calculated spectra have to be integrated over angle and averaged in energy to be comparable with the experimental results of this work. In addition an energy resolution has to be folded in. To integrate over the angles we start from:

$$\frac{d\sigma}{dE} = \int \frac{d^2\sigma}{dE d\Omega} \, d\Omega \tag{1.15}$$

with dΩ = $2\pi \cdot \sin(\Theta)$ dΘ for an integrand independant of Φ. The integral is replaced

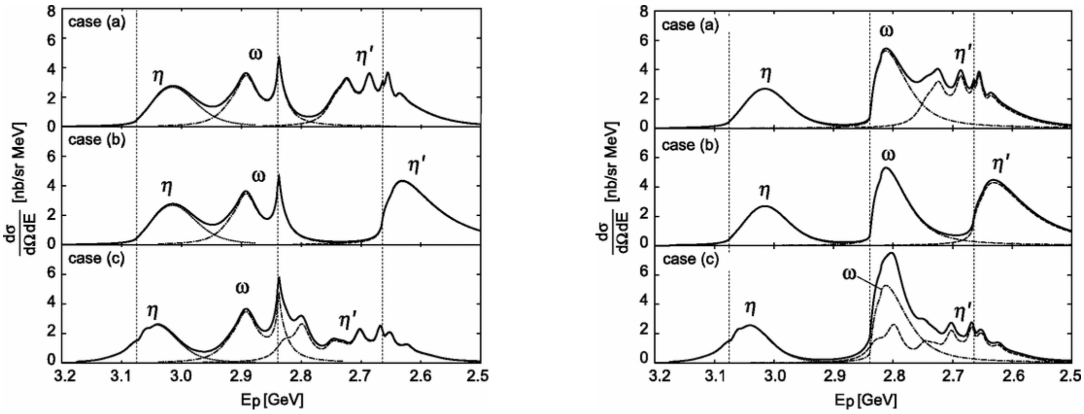

(a) (b)

Figure 1.15: Calculated spectra of ^{12}C(γ,p) reactions for η-, ω- and η'-mesic nucleus formation at E_γ = 2.7 GeV are shown as functions of the emitted proton energies in the final states. The vertical dashed lines indicate the production thresholds of the η-, ω- and η'-mesons. The ω-nucleus potential is assumed to be (a) attractive and (b) repulsive. [23]

by a sum:

$$\frac{d\sigma}{dE} = 2\pi \cdot \int \frac{d^2\sigma}{dEd\Theta} \sin(\Theta)\, d\Theta \tag{1.16}$$

$$= 2\pi \cdot \sum_{i=1}^{3} \frac{d^2\sigma}{dEd\Theta_i} \sin(\Theta_i)\, \Delta\Theta \tag{1.17}$$

for the three angle Θ_i = (1°, 5°, 10°) we assume average angles $\langle\Theta\rangle_i$ = (1.75°, 5.25°, 8.75°). The step size is $\Delta\Theta$ = 3.5° $\hat{=}$ 0.061 rad. This yields:

$$\frac{d\sigma}{dE} = 0.384 \cdot \sum_{i=1}^{3} \frac{d^2\sigma}{dEd\Theta_i} \sin(\langle\Theta\rangle_i) \tag{1.18}$$

The result is shown for two different potentials in figure 1.18(a) and 1.18(c). For adding the spectra for the three different energies E_i = (1.25 GeV, 2.0 GeV, 3.1 GeV) , they are weighted with w_i=1/E_i according to their relative intensity in the

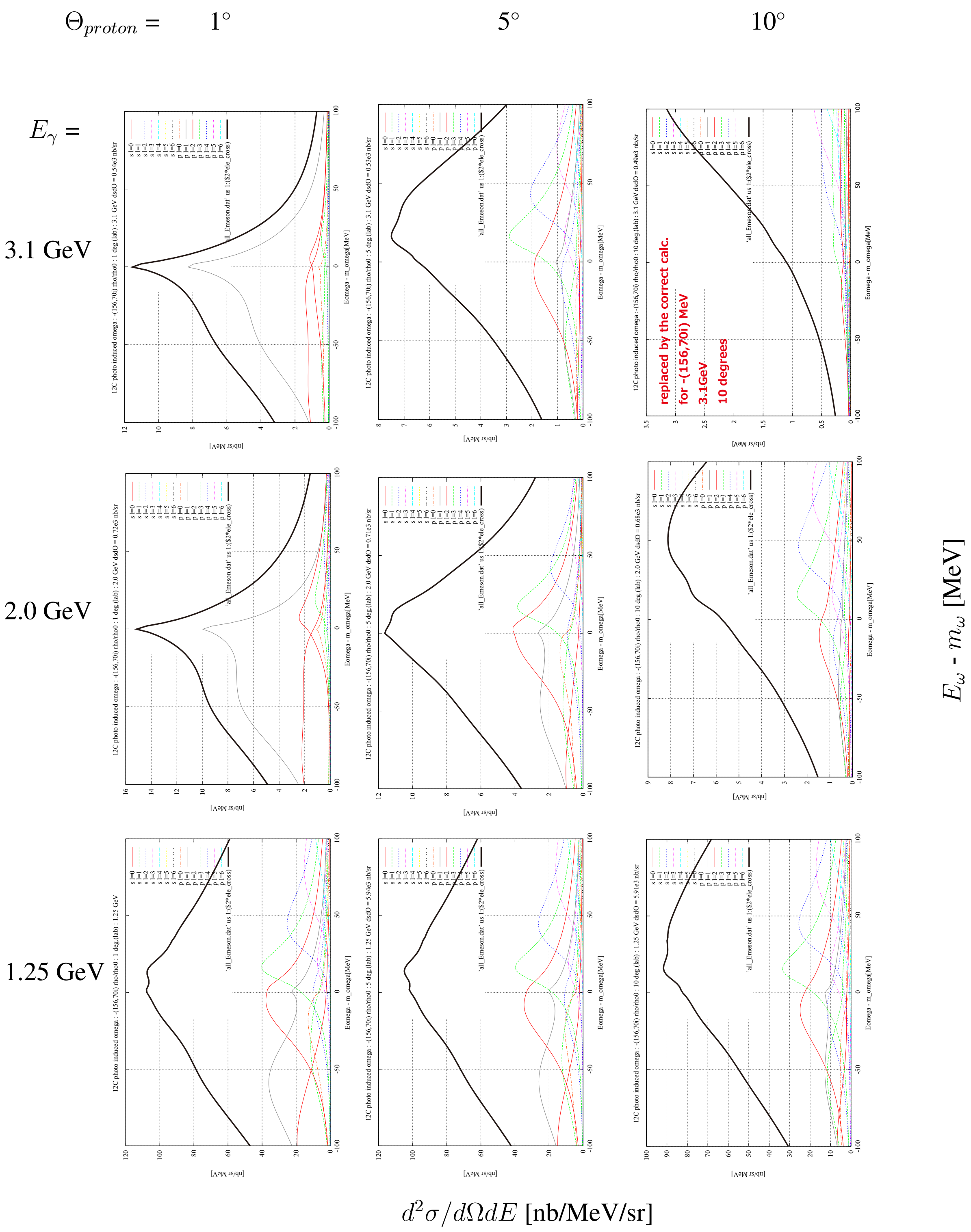

Figure 1.16: Calculated spectra of the ^{12}C(γ,p) reactions for ω-mesic nucleus formation as function of the kinetic energy of the ω-meson for three different energies and three different angles of the outgoing proton for a potential of (V_0, W_0) = (-156, 70) MeV. Individual states are indicated by the colored lines. The sum is drawn in black. [22]

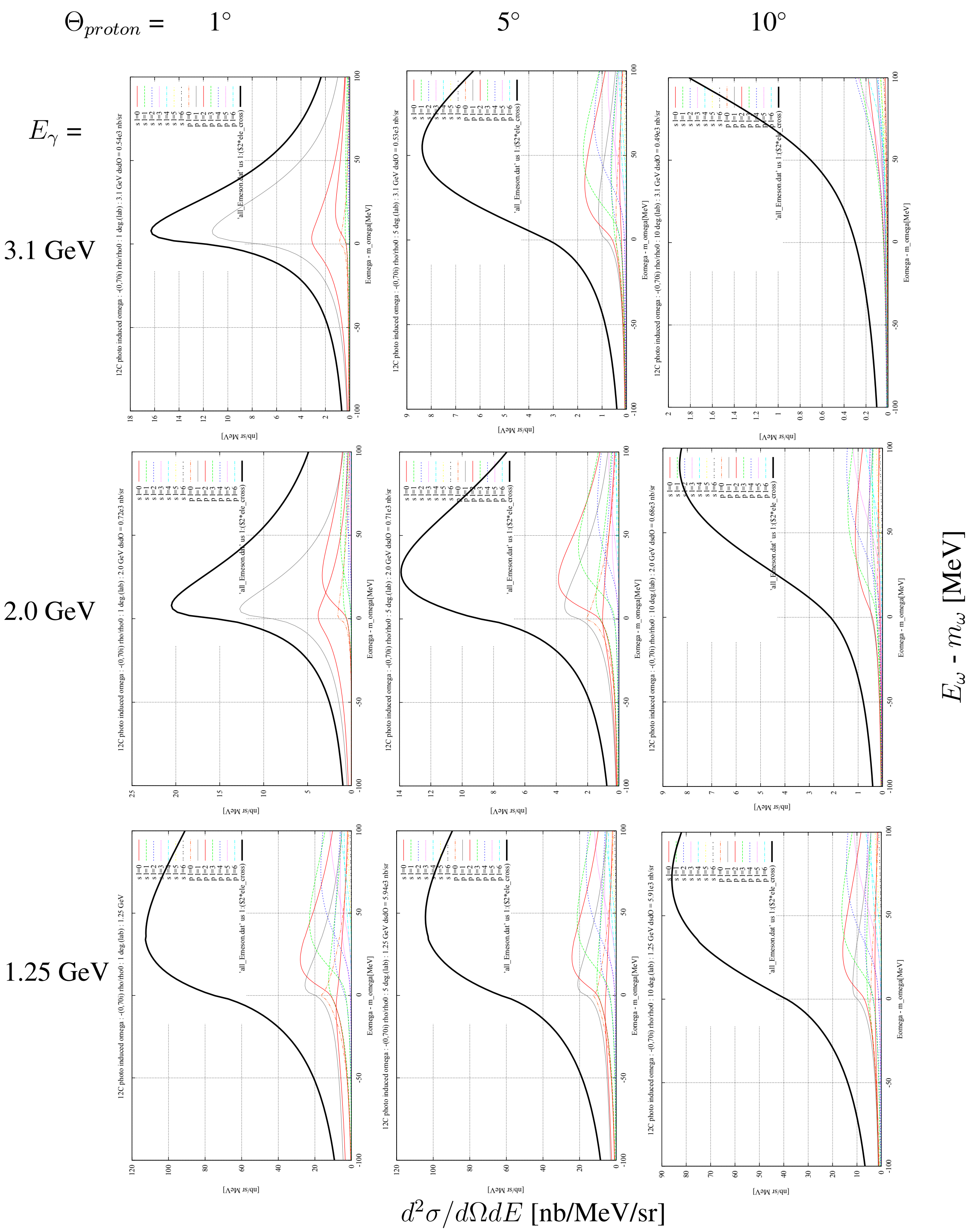

Figure 1.17: Calculated spectra of the ^{12}C(γ,p) reactions for the ω-mesic nucleus formation as function of the kinetic energy of the ω-meson for three different energies and three different angles of the outgoing proton for a potential of (V_0, W_0) = (0, 70) MeV. Individual states are indicated by the colored lines. The sum is drawn in black. [22]

bremsstrahlung spectrum in the experiment (see section 2.3.1).

$$\frac{d\sigma}{d\Omega} = \int \frac{d^2\sigma}{dEd\Omega}\, dE \tag{1.19}$$

$$= \frac{\sum_{i=1}^{3} \frac{d^2\sigma}{dE_i d\Omega}\, w_i}{\sum_{i=1}^{3} w_i} \tag{1.20}$$

The resulting spectra for two different potentials are shown in 1.18(b) and 1.18(d).

The last step is the combination of integration and adding. This yields the spectra shown in figure 1.19(a). After folding with the experimental energy resolution of σ = 17 MeV, the spectra change to figure 1.19(b).

It is important to note, that all these calculations only take into account the population of quantum-mechanical states. Neither decay of the states nor the propagation of the decay products inside the nucleus is included. This is the reason for determining a correction factor for these calculations with the GiBUU transport code in order to estimate the influence of the decays and final state interaction on the experimental results (see section 6.3).

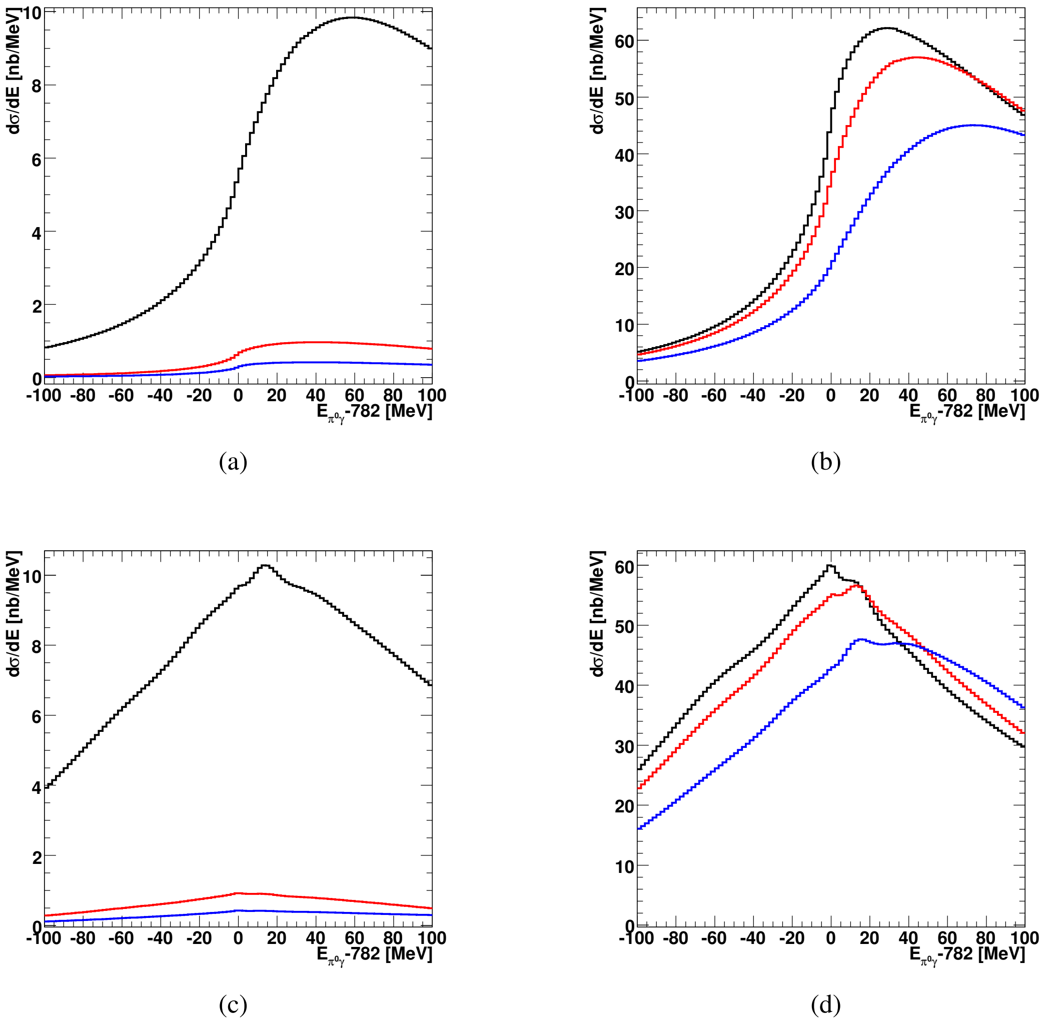

Figure 1.18: (a) and (c): Spectra integrated over angle for three different incoming photon energies: 1.25 GeV (black), 2.0 GeV (red), 3.1 GeV (blue). (b) and (d): Spectra averaged for three different angles: 1°(black), 5° (red), 10° (blue). (a) and (b) are for a zero potential of (V_0, W_0) = (0, 70) MeV (see figure 1.17). (c) and (d) are for a strongly attractive potential (V_0, W_0) = (-156, 70) MeV (see figure 1.16). The cross sections fall off strongly with increasing energy while they decrease with increasing proton angle.

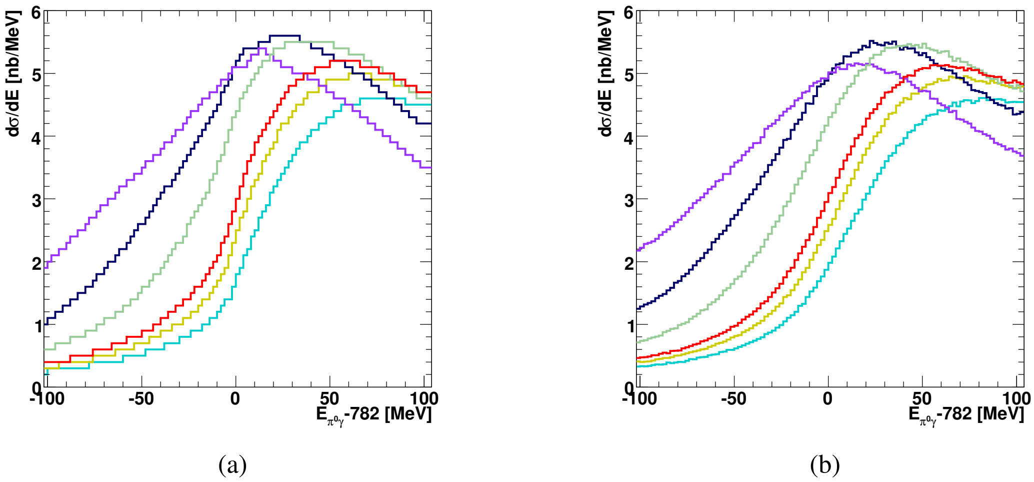

Figure 1.19: Calculated spectra from figures 1.16, 1.17 and appendix B; integrated over angle and summed over energy. The curves are shown for an imaginary part of the potential of W_0 = 70 MeV and different real parts V_0: -156 MeV (violet), -100 MeV (dark blue), -50 MeV (green), 0 MeV (red), +20 MeV (yellow), +50 MeV (light blue). (a) Without energy resolution, (b) with energy resolution of σ = 17 MeV.

Chapter 2

Experimental setup

In this chapter the CBELSA/TAPS experiment at the tagged photon facility ELSA at Bonn, Germany, will be described. First, general principles concerning the detector components will be explained, then a description will be given of the accelerator and the individual detectors.

2.1 The electron accelerator ELSA

The **El**ectron **S**tretcher **A**ccelerator ELSA (see figure 2.1) provides two electron sources and further accelerates the electrons in three stages. While the first electron source emits unpolarized electrons from a 48 keV thermal source, the second one ejects longitudinally polarized electrons, which are needed for production of circularly polarized photons. These polarized electrons are produced using a circularly polarized laser beam directed at a GaAs crystal which leads to photoemission. A polarization degree of 80% is achieved that is measured with the Mott polarimeter. The produced electrons (with small initial energy) are injected into LINACs (**LIN**ear **AC**celerator). At ELSA there are two LINACs. One of these, the so called LINAC 1, provides unpolarized electrons, while the other (LINAC 2) is used to provide linearly polarized electrons. Inside the LINACs the electrons are pre-accelerated up to 20 MeV or 26 MeV, respectively. The pre-accelerated electron beam is sent into the booster synchrotron, accelerating the electrons to 0.5 - 1.6 GeV and sending the electron bunches to the stretcher ring. The Booster Synchrotron has a circumference of $\approx$ 70 m; while the electron energy is increasing, the magnetic field of the bending magnets has to be increased synchronously. It is composed of 12 magnets which serve as bending as well as focussing magnets. The acceleration mechanism leads to a pulsed beam with a duty factor of 5 to 10%

The electrons reach an energy of 1.6 GeV before being injected into the stretcher ring as a pulsed beam with a frequency of 50 Hz. The stretcher ring consists of 16 FODO-cells[1] arranged on a circumference of 164.4 m. It can be operated in three different modes: In the stretcher mode the electrons are slowly extracted to the experimental area without further acceleration delivering a quasi-continuous beam. The second mode is the so called post-accelerator mode. Thereby, the electron bunches are accumulated, stretched and accelerated again up to a maximum energy of 3.5 GeV. The CBELSA/TAPS experiment is run by this mode. During the third mode (storage mode), the electron beam is kept for several hours in the stretcher ring with a constant energy in order to study synchrotron-radiation. At the moment, only the post-accelerator mode is used.

2.2 The photon beam

The photon beam is produced by bremsstrahlung of electrons colliding with atomic nuclei in a radiator (copper, diamond,...). These electrons interact via Coulomb interaction with the nuclei of the foil and emit photons according to the bremsstrahlung process that produces a real photon in the electric field of a nucleus in the radiator material: e + A$\rightarrow$ e$'$ + A + γ.

The maximum energy of the photons produced in this way, with the electron energy E_0, is given by

$$E_{max} = E_0 - m_e c^2 \tag{2.1}$$

[1] One cell is made of a horizontally focussing quadrupole (F) and either a drift pathway or a dipole magnet (O), followed by a horizontally defocussing quadrupole (D) and another drift pathway (O). Thus, focussing of the beam in both horizontal and vertical plane is achieved.

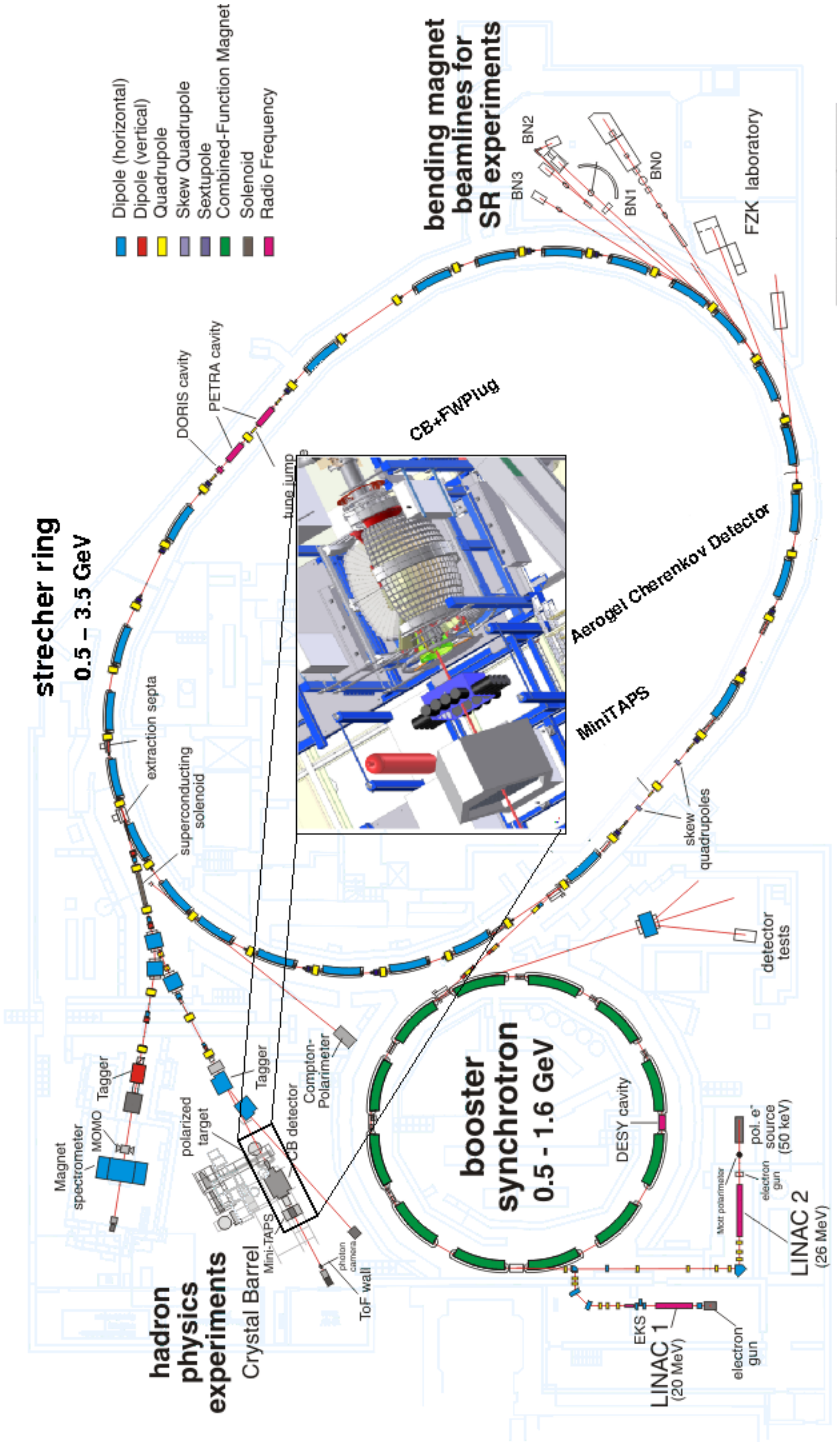

Figure 2.1: Floor plan of ELSA [4].

and their energy distribution in the region $0 < E_\gamma \lesssim 0.8\,\frac{h \cdot f}{E_{max}}$ can be described reasonably well with the expression

$$N_{E_\gamma} \sim \frac{1}{E_\gamma} \tag{2.2}$$

The average half-angle of the emitted photons can be written as

$$\sqrt{\langle \Theta^2 \rangle} = \frac{1}{\gamma} = \frac{m_e c^2}{E} \tag{2.3}$$

This half angle at typical ELSA energies is less than 0.5 mrad, consequently the generated photon beam points into the direction of the electron beam and is collimated quite well.

2.3 Detector components

2.3.1 Tagging system

The tagging system determines the energy of the photons produced via bremsstrahlung of the incoming electrons. Since the energy of the incoming electron beam is known and the momentum transfer of the electrons to the radiator nuclei is negligible [24], the following equation holds true for the energy-momentum conservation for each event [25]:

$$E_{\mathrm{e}^-}^{\mathrm{before}} = E_\gamma + E_{\mathrm{e}^-}^{\mathrm{after}} \tag{2.4}$$

The electron energy is known with high precision ($\frac{\Delta E}{E} = 0.09\%$ at 3.5 GeV). Multiple scattering can be significantly reduced by decreasing the width of the radiator foil. By the choice of a thin radiator foil, the gamma intensity reached is, however, also reduced. For this reason foil thicknesses of 50 μm and 150 μm were chosen: here the intensity remains high (tagger rate of $\approx$ 10 MHz) and most of the multiple scattering is strongly suppressed.

Equation (2.4) expresses that the energy of the bremsstrahlung-photon equals the

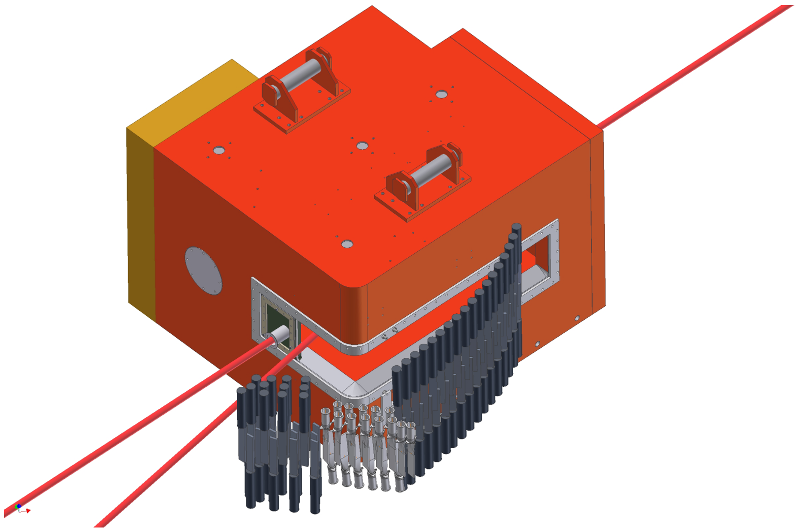

Figure 2.2: CAD of tagger magnet (orange) and the 96 partly overlapping scintillator tagger bars. The electrons arrive from the right side and are deflected towards the scintillator bars. [26]

energy loss of the electron. The remaining energy of electron can be measured with a magnetic electron-spectrometer (the so called tagger, see figure 2.2).

In the relativistic case, the energy of the electron is roughly equal to the momentum of the electron

$$E_{e\prime} = p \cdot c = B \cdot r \cdot c \cdot q_e \tag{2.5}$$

With known magnetic field ($\vec{B}$) and bending radius of the electron track (r) the energy of the deflected electron can be extracted. If the the initial energy of the electrons is also known, the energy of the generated photon can also be calculated:

$$E_\gamma = E_{\mathrm{e}^-}^{\mathrm{accelerator}} - E_{\mathrm{e}^-}^{\mathrm{measured}} \tag{2.6}$$

Deflected electrons are detected by the tagging system consisting of 96 plastic scintillator bars which are read out by PMTs. The bars overlap each other to reduce the noise and cover the energy between 18% and 96% of the electron-beam energy (see figure 2.3).The energy resolution for the bars varies between 14% for small photon

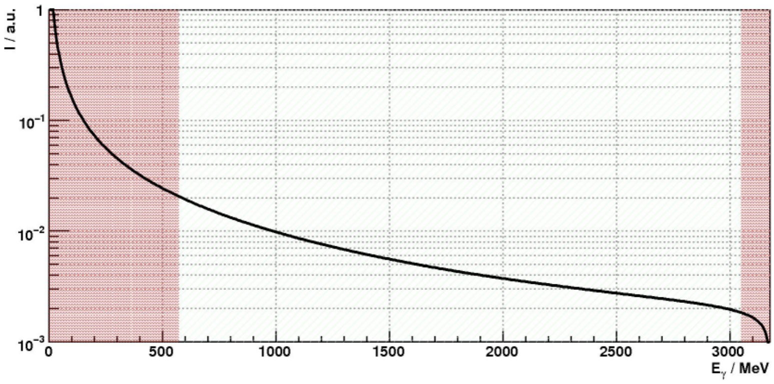

Figure 2.3: Energy coverage of the tagger for an incident electron energy of 3.2 GeV. The shaded energy regions are not tagged. [27]

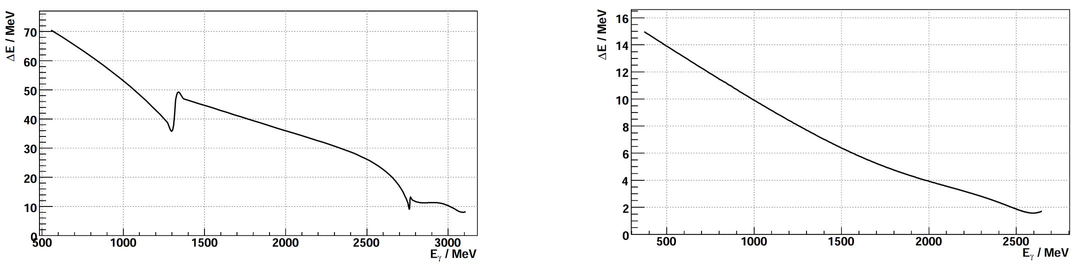

(a)

(b)

Figure 2.4: Energy resolution of the tagger-bars (a) and -fibers (b) for an incident electron energy of 3.2 GeV [27].

energies and 0.3% for the highest energies (shown in figure 2.4(a)). The energy resolution for the tagger fibers is much better, it varies from 3.9% to 0.07% for the highest energies (see figure 2.4(b)).

In order to derive the real photon energy from the bar/fiber hit by the deflected electron, the tagger has to be calibrated. This was done during the commissioning of the detector setup. Figure 2.5 shows the dependence of the photon energy on the bar/fiber number.

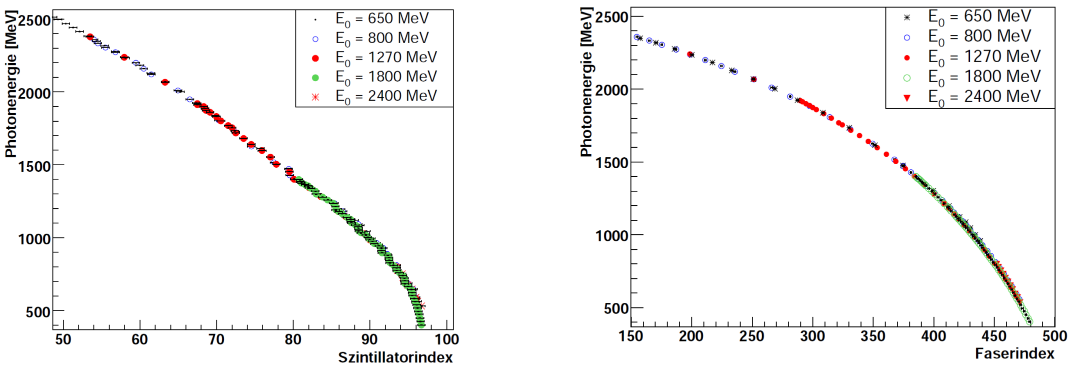

(a) (b)

Figure 2.5: Energy calibration of the tagger-bars (a) and -fibers (b) [27].

2.3.2 Inner Detector

The Crystal Barrel detector is not suited to distinguish between charged and neutral particles. To allow a charged/neutral particle separation, the Inner Detector is installed inside the CB. The Inner Detector consists of 513 scintillating fibers with a diameter of 2 mm, which are arranged cylindrically in three layers around an aluminum frame. Two layers of the fibers run with +25.7° and -24.5° inclination to the beam direction, while the third one runs parallel to the beam. These fibers are read out with 16 channel multi-anode photomultiplier tubes. This detector provides time and - if more than one fiber fires - position information. Energy is not read out [28]. The detector absorbs the low energetic electromagnetic background as well as protons with moderate kinetic energy up to 35 MeV [29]. In addition, protons with kinetic energies lower than 90 MeV cannot reach the EMC because of absorption in the Inner Detector and in the holding frame of the Crystal Barrel. The detector is 40 cm long and covers the complete 2π azimuth angle and polar angles between 16° and 164°[28].

2.3.3 Crystal Barrel detector

The Crystal Barrel detector (CB) is a high resolution system for charged particles and photons, with nearly complete coverage of the solid angle. It was built to detect

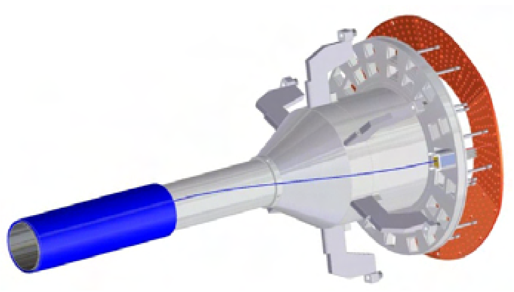

Figure 2.6: Schematic view of the Inner Detector [26].

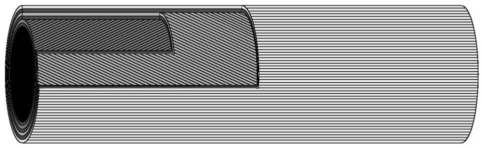

Figure 2.7: Arrangement of the layers of the Inner Detector [26].

photons and charged particles with high efficiency, good energy- and spatial resolution over a wide energy range from 20 MeV to 2 GeV. The spatial resolution of the detector is better than 1.5° and the energy resolution is parametrized by

$$\frac{\sigma}{E_\gamma} = \frac{2.5\,\%}{\sqrt[4]{E_\gamma/\mathrm{GeV}}} \tag{2.7}$$

[30, 31].

CB covers polar angles from 30° to 156° and full 360° in azimuthal angles. It consists of 1230 CsI crystals with Tl doping in order to improve the light output. Each crystal has a length of 30 cm corresponding to about 16 radiation lengths X_0.
The crystals are arranged in 20 rings of 60 crystals each and one ring of 30 crystals at the most backward angle.
The deliberately introduced thallium impurities act as wave length shifter for the emitted scintillation light and due to this effect the light output is “increased” because the reabsorption of the wavelength-shifted light in the crystal is suppressed [32].
Every crystal is mounted in a titanium case for mechanical stability and wrapped in Kapton foil for electric insulation. The crystals are read out with pin-photodiodes. To match the wavelength of the scintillation light to the spectral sensitivity of the photodiode, a wavelength-shifting plastic foil of 3 mm thickness is placed between crystal backface and photodiode. Due to the long rise-time of the signal (2 μs), time information from the CB detector is not used. For ensuring the stability of the gain

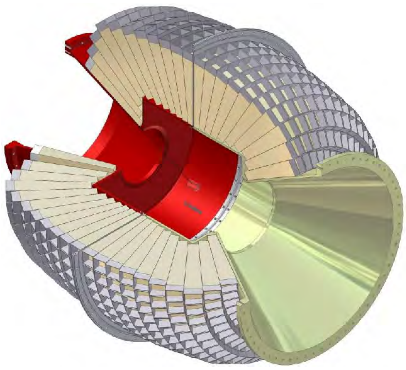

Figure 2.8: CAD of the Crystal Barrel detector [26].

1. Titanium case, 2. Wavelength shifter,
3. Photodiode, 4. Preamplifier, 5. Optical fiber,
6. Case cover

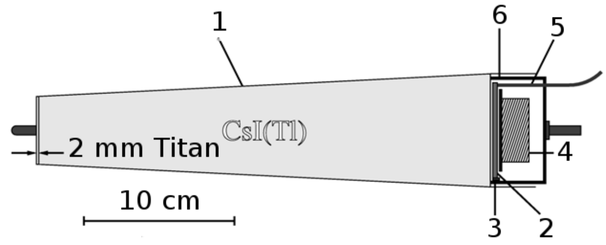

Figure 2.9: Composition of one Crystal Barrel module [33].

each crystal is irradiated with a xenon-flashlight based light-pulser system which runs several times per day as dedicated runs.
In order to allow access to target and Inner Detector, the Crystal Barrel is divided into two independent halves.

2.3.4 Forward Plug detector

The Forward Plug detector (FwPlug), consisting of 90 Tl-doped CsI crystals (same type as CB crystals) in 3 rings, covers the 12°-30° polar angles and 0°-360° azimuthal angles. In front of the crystals, scintillator-plates are installed in order to enable a discrimination between charged and neutral particles. The scintillation-light is read out with PMTs coupled to the crystals by plastic light-guides. The detector provides spatial-, energy- and time information.

2.3.5 MiniTAPS detector

The Mini Two Arm Photon Spectrometer (MiniTAPS) detector covers the most forward angles from 1° to 10°-12° degrees[2]. The detector was designed to reach the following goals: First, it should be able to detect photons (the decay products of neu-

[2] This value depends on the distance between the detector and the target.

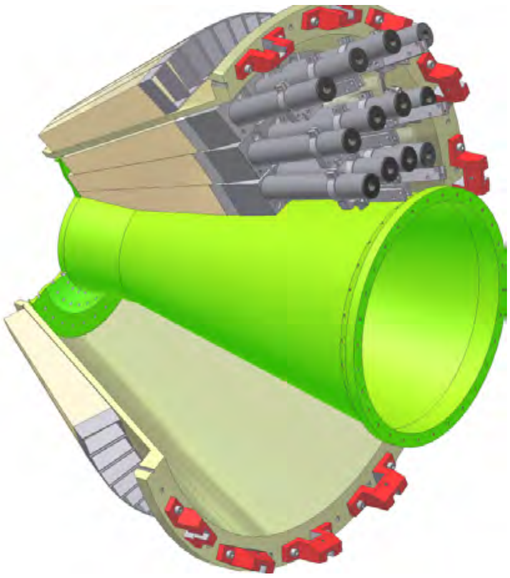

Figure 2.10: CAD of the Forward Plug detector [26].

tral mesons) with great efficiency and good energy- and time-resolution. It also has to detect charged particles. To fulfill these requirements MiniTAPS is built out of BaF_2 crystals with a plastic scintillator in front. The BaF_2 has a good energy resolution in the energy range between 45 and 790MeV [34], parametrized by

$$\frac{\sigma}{E_\gamma} = \frac{0.59\,\%}{\sqrt{E_\gamma/\mathrm{GeV}}} + 1.9\,\% \tag{2.8}$$

for 2 μs integration gate for the scintillation light and a time-resolution of Δt = 160 ps FWHM[3] at 43.5 MeV [35]. BaF_2 has two different scintillation components, a fast one and a slow (see table 2.1). Because the amount of produced scintillation light depends on the ionization density and since different particle types populate the luminescence centers with different probability, this behavior allows the use of BaF_2 for particle identification via pulse shape anylysis, i.e. by the ratio of the intensity in the fast and slow component within a fixed time gate.

MiniTAPS consists of 216 individual detector modules. Each module is made up of a BaF_2 crystal and a plastic veto for identification of charged particles (see figure 2.11). The crystals have two parts: a cylindrical part with a length of 25 mm and

[3] **F**ull **W**idth of **H**alf **M**aximum

Scintillation component	Decay constant [ns]	Mean wavelength [nm]	Light output
slow	630	300	21%
fast	0.9	220	2.7%

Table 2.1: Properties of the slow and fast component of the BaF_2 scintillation light. The light output is given relatively to the light output of NaI(Tl). [36]

a diameter of 54 mm for the connection to the PMT and the hexagonal part where most of the light-generation occurs. The hexagonal part is 225 mm long. The total lengths is 250 mm which corresponds to 12 radiation lengths and its diameter measures 59 mm. To decrease the loss of scintillation photons, each crystal is wrapped in several layers of Teflon foil (Tetratex PTFE, 1.5 mil) and one layer of aluminum foil. In order to achieve a better optical connection between crystal and PMT, optical grease (Baysilone 300000) is used. Crystals and the PMTs are mechanically tied together by heat-shrinking tubes. Altogether there is about 1 mm passive material between adjacent crystals. Each PMT is covered with Mu-metal to shield it from magnetic fields that can affect the electron collection mechanism of the PMTs.
The veto detectors are arranged in a separated wall in front of the crystals. Each plastic veto consists of a 0.5 cm plastic scintillator (NE 102A). To match the scintillation light to the sensitive range of the PMT, wavelength-shifting fibers (Bichron BFC92) are used to transfer the light of the plastic scintillator to the 16 channel PMT. Since the most forward region has to cope with a very high rate of electromagnetic particles, the middle part of the veto wall is read out with special PMTs designed for standing high particle rates (so called “Booster-base” PMTs).
All 216 detectors are arranged in one big hexagon-shaped wall configuration where the longitudinal crystal axes are parallel to each other and to the photon beam (see figure 2.12).

2.3.6 Aerogel-Čerenkov detector

In this section the aerogel-threshold-Čerenkov detector will be described which was built for the CBELSA/TAPS experiment. For measurements of ω-mesic nuclei, for-

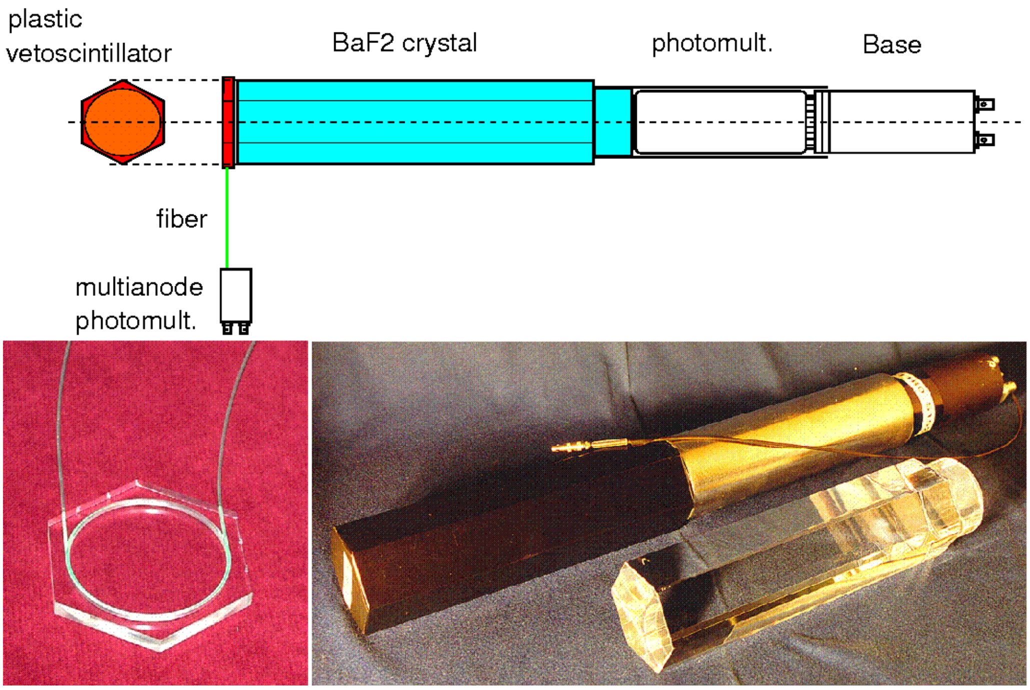

Figure 2.11: Schematic view (above [37]) and photograph (below) of one MiniTAPS module consisting of a BaF_2 crystal and a plastic veto.

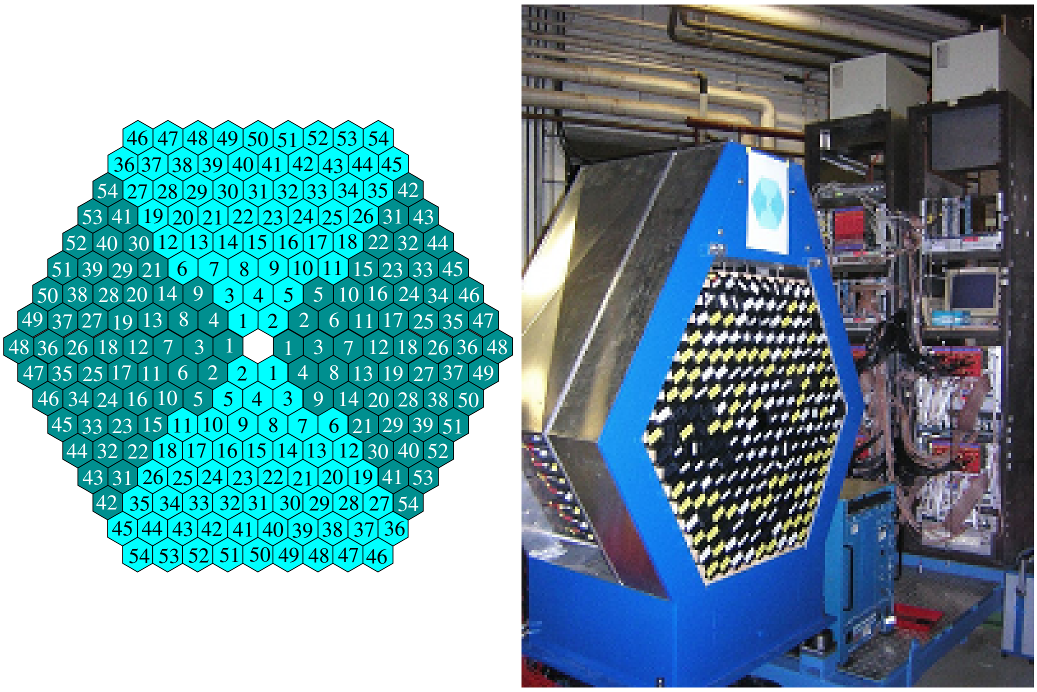

Figure 2.12: Arrangement of crystals inside the MiniTAPS wall. One crystal is removed from the center of the setup. Photons which did not generate hadronic reactions will leave the setup through this hole.

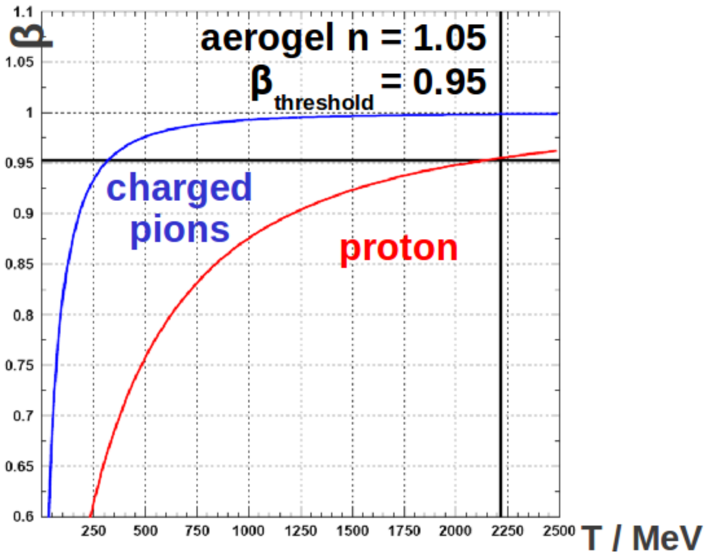

Figure 2.13: Plot of the β-factor ($\beta = v/c$) of charged pions and protons as function of the kinetic energy [38]. The threshold β_{thrsh} for the used aerogel and the threshold energy for protons are shown.

ward going protons have to be identified unambiguously (see Chapter 1.4): One has to discriminate protons from charged pions and electrons/positrons. The kinematical conditions in the given setup are such that the use of a threshold Čerenkov detector with aerogel as active radiator material is the best choice. For this reason, the detector was built by II. Physikalisches Institut, Justus-Liebig-University Giessen in collaboration with the group of Hartmut Schmieden of the Physikalisches Institut, University of Bonn. The efficiency determination concerning the detection of highly energetic electrons was performed within the diploma thesis of Stefan Materne [39]. A further test to determine the efficiency for highly energetic charged pions was performed by me at the GSI facility within my diploma thesis [40]. Both independently obtained efficiencies are higher than 99%.

The detector consists of a box which is painted inside with a diffusely reflecting paint manufactured by Labsphere (*Spectraflect*). The reflectivity of this paint is 0.94-0.97 in the wavelength range of 250 - 1000 nm. On the narrow sides of the detector box twelve photomultiplier tubes (PMT) are attached (see figure 2.14). Six of them are manufactured by the company Burle, the other six by Philips. 88 tiles of aerogel radiator (for details see [39, 40]) were arranged in a wall of 5 cm thickness and 47 $\times$

Figure 2.14: Aerogel-Čerenkov detector [44]. Twelve photomultipier tubes are located at the narrow sides of the quadratic box containing the aerogel radiator.

47 cm^2 area (see figure 2.15). The chosen thickness of the active volume was a compromise between Rayleigh-scattering and light yield. In the center of the wall there is a small hole of 2 cm radius for the photon beam of the experiment. The aerogel is inside a special insertion which is put in the outer box. The front and the rear panel consist out of 1 mm thick aluminum sheets (see figure 2.15).
The aerogel itself is produced by Matsushita Electric Work from Japan. This highly porous, non-hygroscopic material has a density of 0.18 g/cm^3 and an index of refraction of 1.05 (for details see [41, 42, 43]). This means that a charged particle must have at least a β-factor of β_{thr}=$\frac{1}{n}$ $\approx$ 0.95 in order to produce Čerenkov-light. The PMTs have a 5 inch diameter, UV-transparent glass entrance windows and have a quantum efficiency of about 22.5% at 385 nm (Burle) and 25% at 400 nm (Philips), respectively. These special entrance windows are mandatory since the intensity maximum of the emitted Čerenkov-light lies in the UV range.

(a) Without aerogel.

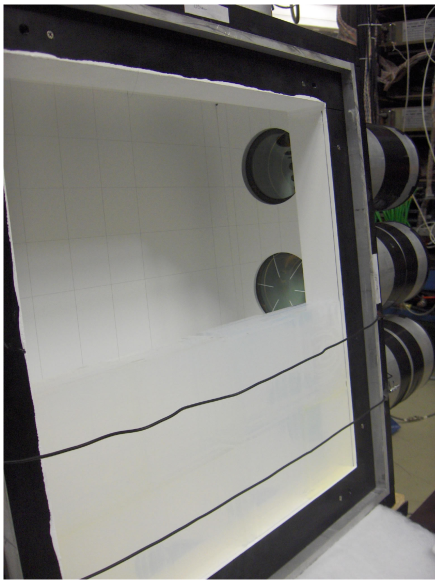

(b) With several aerogel-tiles in the foreground.

Figure 2.15: View of the inside of the aerogel-Čerenkov detector [44]. The PMTs can be recognized at the sides.

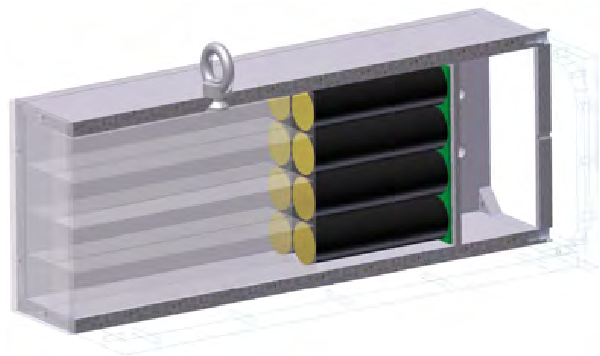

Figure 2.16: CAD of the Gamma Intensity Monitor [26].

2.3.7 Gamma Intensity Monitor

The gamma intensity monitor is located behind the MiniTAPS detector. It was designed to detect photons not interacting in the target. The measurement of the photon flux is an essential information for cross section measurements.
The detector consists of a 4x4 PbF_2 crystal block (see figure 2.16). Incident photons generate electromagnetic showers inside the PbF_2-array. In turn, the shower particles, i.e. electrons and positrons generate Čerenkov light. This light is collected by PMTs.

2.4 Trigger logic

The data acquisition system is not fast enough to record all events registered by the detectors, and many events originate from background processes like photon conversion, δ-electrons, etc. Therefore, a dedicated trigger system has to decide on line whether an event is worth storing on disk. Incorrect definitions cannot be revoked and therefore can cause a drastic reduction of statistics and large acceptance holes. The main trigger used in the experiment consists of two levels, described in the following.

2.4.1 First-level trigger

This is the first basic, fast part of the decision taking on a timescale of less than 100 ns. Whether the digitization of all values starts, depends on this decision. The first level trigger is made by the tagger in coincidence with the Forward Plug and/or the MiniTAPS. The Crystal Barrel cannot contribute to the first level trigger because of the slow signal rise-time of the Cs(Tl) scintillators. As a consequence, the Crystal Barrel response can be included into the second level trigger.
The Forward Plug provides two signals:

FwPlug1: At least one particle hit was registered in the Forward Plug with an energy higher than the LED[4] threshold.

FwPlug2: At least two particle hits were registered in the Forward Plug.

The MiniTAPS provides two signals:

MiniTAPS (LED 1): At least 1 particle hit was registered in MiniTAPS with an energy higher than the LED (high) threshold.

MiniTAPS (LED 2): At least 2 particle hits were registered in MiniTAPS, each with an energy higher than the LED (low) threshold.

An overview of the MiniTAPS trigger scheme is given in appendix C. The first level trigger is generated by the combination of these signals in coincidence with the tagger.

2.4.2 Second-level trigger

Due to the long rise-time of the Cs(Tl) scintillator signal, the Crystal Barrel cannot be used in the first level trigger. During digitization, more time is available for the second-level trigger to decide whether or not to read out the event. This longer time span ensures that the second-level trigger can be more complex. The number of registered hits in the CB is determined by the **FA**st **C**luster **E**ncoder (FACE). The FACE algorithm needs approximately 10 μs, therefore it is fast enough to contribute to the

[4]**L**eading **E**dge **D**iscriminator

Length l	5.1 cm
Radius r	1.5 cm
Density (standard) ρ	0.0708 g/cm^3
Surface density $\sigma = \rho \cdot l$	0.361 g/cm^2
Radiation length X_0	63.04 g/cm^2
σ/X_0	0.57%

Table 2.2: Properties of the LH_2 target.

second level trigger, but too slow for pre-triggering purpose. During the beamtimes several types of triggers were applied. Since the final state of interest in our case consists out of three photons and one proton, mainly trigger conditions with at least three or at least four particle hits were applied (see chapter 3). The detailed trigger conditions can be found in appendix D.

2.4.3 Stand-alone trigger

Before the beamtimes, a special trigger condition was used to collect cosmic muon data for calibration purposes of MiniTAPS (see also appendix C). If the read-out energy exceeded the low LED trigger-threshold in any of the crystals or the pedestal pulser was firing, then a trigger was generated.

2.5 Targets

In this section the main properties of the targets, used in the beamtimes, are listed.

2.5.1 Liquid hydrogen

The target cell for the liquid hydrogen (LH_2) is made of Kapton. Table 2.2 shows its main properties. For determining the cross section the number of target nuclei per

Mass (measured) m	17.70 g
Length l	1.5 cm
Radius r	1.5 cm
Density (measured) ρ	1.6694 g/cm^3
Surface density $\sigma = \rho \cdot l$	2.5041 g/cm^2
Radiation length X_0	42.70 g/cm^2
σ/X_0	5.9%

Table 2.3: Properties of the carbon target.

cm^2 is needed. It can be calculated via:

$$n_{target}^{LH_2} = \rho \cdot l \cdot \frac{N_A}{M_A} \tag{2.9}$$
$$= 0.0708 \frac{\mathrm{g}}{\mathrm{cm}^3} \cdot 5.1\,\mathrm{cm} \cdot \frac{6.022 \cdot 10^{23}\,\mathrm{mol}^{-1}}{1.00794 \frac{\mathrm{g}}{\mathrm{mol}}} \tag{2.10}$$
$$= 2.157 \cdot 10^{23} \frac{1}{\mathrm{cm}^2} \tag{2.11}$$

2.5.2 Carbon

To place the carbon target in the beam pipe, an aluminum extension was attached to the beam-pipe. The target - a carbon disk with a diameter of 3 cm and a thickness of 1.5 cm - was held in the center of the CB via a Rohacell frame and was placed inside a carbon-fiber tube. This tube was attached to the aluminum extension. Table 2.3 shows its main properties.

$$n_{target}^{C} = \rho \cdot l \cdot \frac{N_A}{M_A} \tag{2.12}$$
$$= 1.6694 \frac{\mathrm{g}}{\mathrm{cm}^3} \cdot 1.5\,\mathrm{cm} \cdot \frac{6.022 \cdot 10^{23}\,\mathrm{mol}^{-1}}{12.0107 \frac{\mathrm{g}}{\mathrm{mol}}} \tag{2.13}$$
$$= 1.26 \cdot 10^{23} \frac{1}{\mathrm{cm}^2} \tag{2.14}$$

Chapter 3

Overview of beamtimes

In this section an overview of the beamtimes performed at the electron stretcher accelerator ELSA in Bonn is given.

3.1 Carbon beamtime in March 2007

This beamtime took place from 4^{th} to 26^{th} of March 2007. The data acquisition collected data files for about 297 hours (internal CBELSA/TAPS run number 100385 - 102381). The beam current delivered by the accelerator was on average 0.140 nA at an electron beam energy of 3.25 GeV. Table 3.1 shows the number of data files for each trigger condition. For the complete beamtime (except a few runs for testing purposes) a copper radiator of 50 μm thickness was used. All photon energies from 650 - 3110 MeV were tagged because, in contrast to a free proton, on a nucleus ω-mesons can be produced below the threshold of 1108 MeV as a consequence of the Fermi motion of the nucleons. To collimate the photon beam a tungsten collimator of

Trigger	Files	Time
carbon_omega	320	86 h
carbon_omega_prime	1117	212 h
total	1437	298 h

Table 3.1: Collected data files during the carbon beamtime (March 2007).

MiniTAPS crystal	LED 1 (high)	LED 2 (low)
1^{st} ring	600-1200 MeV	600-1200 MeV
2^{nd} ring	120 MeV	80 MeV
other rings	120 MeV	80 MeV
FwPlug crystal	LED	
	25 MeV	

Table 3.2: LED thresholds during the carbon beamtime (March 2007).

7 mm diameter was installed in the beamline. The distance of MiniTAPS to the target center was 235 cm. Table 3.2 shows the LED thresholds of the MiniTAPS detector chosen for the beamtime. Since it was the first beamtime after a long break, not every subdetector was optimally working.

An overview of the typical count rates during the beamtime in the various detectors is given in table 3.3.

3.2 LH_2 beamtime in October 2008

This beamtime took place from 20^{th} to 28^{th} of October 2008. The data acqusition collected data files for about 140 hours (internal CBELSA/TAPS run number 120204 - 120836). The beam current delivered by the accelerator was on average 600 pA at an electron beam energy of 3.25 GeV. At the beginning of the beamtime a copper radiator of 50 μm was used (run number 120204 -120235), afterwards it was replaced by a copper radiator with a thickness of 150 μm to increase the photon flux impinging on the target. The tagger bars 89-96, which correspond to photon energies lower than 1000 MeV, were switched off, since the free production threshold for ω-mesons is at 1108 MeV. To collimate the photon beam a tungsten collimator of 4 mm diameter was installed in the beamline. Very important for the correct reconstruction of particle four-vectors in the analysis is the position of the MiniTAPS detector in beam direction. Up to run number 120278 the detector was 210 cm away from the target center, which is the standard position. Afterwards it was moved downstream to a distance of 235 cm because in the former beamtime of March 2007 it stood at this position. This allowed a better comparison of the results of the two beamtimes. In

Trigger:	carbon_omega_prime
Radiator:	Cu-50
Beam current:	0.140 nA
Detector	Rate
Tagger	5.3 MHz
GIM	4.4 MHz
Tagger & GIM	3.2 MHz
Inner Detector	190 kHz
FwPlug Veto	275 kHz
FwPlug (1 particle)	8000 Hz
FwPlug (2 particles)	760 Hz
MiniTAPS (LED 1)	33 kHz
MiniTAPS (LED 2)	15 kHz
Fast reset	5 kHz
Event rate	425 Hz
Live time	30%

Table 3.3: Typical count rates during the carbon beamtime (March 2007) for a copper radiator of 50 μm and thresholds given as in table 3.2 for the main trigger condition *carbon_omega_prime*.

Trigger	Files	Time
omega_prime	462	131 h
trig41	46	6.5 h
omega	7	1.2 h
trig42c	4	0.5 h
total	519	140 h

Table 3.4: Collected data files during the LH_2 beamtime (October 2008).

MiniTAPS crystal	LED 1 (high)	LED 2 (low)	File number
1^{st} ring	600-1200 MeV	600-1200 MeV	120326-120836
2^{nd} ring	120 MeV	80 MeV	120326-120836
other rings	120 MeV	80 MeV	120326-120836
FwPlug crystal	LED		File number
	25 MeV		120326-120836

Table 3.5: LED thresholds during the LH_2 beamtime (October 2008).

this thesis only the files with a MiniTAPS distance of 235 cm are analyzed. The table 3.4 shows how many data files for each trigger condition were taken. The table 3.5 shows the chosen LED thresholds of the MiniTAPS detector for the beamtime.

An overview of the typical count rates during the beamtime in the various detectors is given in table 3.6.

3.3 LH_2 beamtime in November 2008

This beamtime took place from 6^{th} to 27^{th} of November 2008. The data acqusition collected data files for about 308 hours (internal CBELSA/TAPS run number 121537 - 122906). The energy of the electron beam was set to 2.35 GeV. Table 3.7 shows how many data files for each trigger condition were taken. This run was for experiments with circularly polarized beam photons produced via Møller-Scattering. The position of the MiniTAPS detector was at the position 210 cm downstream of the center of the target. Table 3.8 shows the chosen LED thresholds of the MiniTAPS detector for the beamtime. An overview of the typical count rates during the beamtime in the various detectors is given in table 3.9.

3.4 Carbon beamtime in January 2009

This beamtime took place from 26^{th} of January to 25^{th} of February 2009. The data acqusition collected data files for about 525 hours (internal CBELSA/TAPS run number 124710 - 127247). This beamtime was performed to increase the statistics of the

Trigger:	omega_prime
Radiator:	Cu-150
Beam current:	0.6 nA
Detector	Rate
Tagger	>10 MHz
GIM	7.5 MHz
Tagger & GIM	5.5 MHz
Inner Detector	40 kHz
FwPlug Veto	90 kHz
FwPlug (1 particle)	5000 Hz
FwPlug (2 particles)	650 Hz
Aerogel-Čerenkov	2 MHz
MiniTAPS (LED 1)	20 kHz
MiniTAPS (LED 2)	2500 Hz
Fast reset	8000 Hz
Event rate	450 Hz
Live time	10 - 40%

Table 3.6: Typical count rates during LH_2 beamtime (October 2008) for a copper radiator of 150 μm and the thresholds given as in table 3.5 for the main trigger condition *omega_prime*.

Trigger	Files	Time
trig41	261	77 h
trig42c	718	231 h
total	979	308 h

Table 3.7: Collected data files during the LH_2 beamtime (November 2008).

MiniTAPS crystal	LED 1 (high)	LED 2 (low)
1^{st} ring	400-1000 MeV	400-1000 MeV
2^{nd} ring	80 MeV	80 MeV
other rings	80 MeV	80 MeV
FwPlug crystal	LED	
	25 MeV	

Table 3.8: LED thresholds during the LH_2 beamtime (November 2008).

Trigger:	trig_42c
Radiator:	Møller
Detector	Rate
Tagger	6.5 MHz
GIM	5.0 MHz
Tagger & GIM	4.0 MHz
Inner Detector	6.5 kHz
FwPlug Veto	25 kHz
FwPlug (1 particle)	800 Hz
FwPlug (2 particles)	100 Hz
Gas-Čerenkov	0.2 MHz
MiniTAPS (LED 1)	2.5 kHz
MiniTAPS (LED 2)	300 Hz
Fast reset	2500 Hz
Event rate	300 Hz
Live time	30 - 60%

Table 3.9: Typical count rates during LH_2 beamtime (November 2008) for the Møller-polarimeter for the main trigger condition *trig_42c*.

Trigger	Files	Time
eta4	1125	368 h
eta4nc	456	120 h
trig41	229	36.5 h
total	1810	525 h

Table 3.10: Collected data files during the carbon beamtime (January 2009).

carbon beamtime of March 2007. So, it was tried to reproduce similar conditions as in the March 2007 beamtime for detector settings, thresholds and beam intensity.
The beam current delivered by the accelerator was on average 600 pA at an electron beam energy of 3.25 GeV. The table 3.10 shows how many data files for each trigger condition were collected. For the complete beamtime a copper radiator of 50 μm was used, since the count rates in several detectors were already at their upper limit. All photon energies from 650 - 3110 MeV were tagged. To collimate the photon beam a tungsten collimator of 7 mm diameter was installed in the beamline. The distance of MiniTAPS to the target center was 235 cm as in the LH_2 and the former carbon beamtime. The table 3.11 shows the chosen LED thresholds of the MiniTAPS detec-

MiniTAPS crystal	LED 1 (high)	LED 2 (low)	File number
1^{st} ring	180 MeV	120 MeV	125062 - 127247
2^{nd} ring	140 MeV	80 MeV	125062 - 127247
other rings	100 MeV	80 MeV	125062 - 127247
FwPlug crystal	LED		File number
	25 MeV		125062 - 127247

Table 3.11: LED thresholds during the carbon beamtime (January 2009).

tor for the beamtime. Starting with file 125062 the aerogel-Čerenkov detector was used as a hardware veto trigger so that the trigger condition *eta4* could be used.

An overview of the typical count rates during the beamtime in the various detectors is given in table 3.12.

Trigger:	eta4
Radiator:	Cu-50
Beam current:	0.6 nA
Detector	Rate
Tagger	7.1 MHz
GIM	6.4 MHz
Tagger & GIM	5.0 MHz
Inner Detector	90 kHz
FwPlug Veto	200 kHz
FwPlug (1 particle)	5000 Hz
FwPlug (2 particles)	550 Hz
Aerogel-Čerenkov	1.2 MHz
MiniTAPS (LED 1)	165 kHz
MiniTAPS (LED 2)	30 kHz
Fast reset	10 kHz
Event rate	300 Hz
Live time	55%

Table 3.12: Typical count rates during carbon beamtime (January 2009) for a copper radiator of 50 μm and the thresholds given as in table 3.11 for the main trigger condition *eta4*.

Chapter 4

Data analysis

In this chapter details of the data analysis will be presented, beginning with time and energy calibration.

4.1 EXPLORA framework

All data files taken during the beamtimes (see chapter 3) have been stored as ZEBRA-file and have been analyzed with the software EXPLORA [45]. EXPLORA has been developed at Bonn for the CBELSA/TAPS experiment. It is written in C++ as object-oriented framework, based on the ROOT framework developed at CERN [46]. Due to its modular structure a further development and extensions via plug-ins are possible. The data analysis is controlled by XML-files.

4.2 Time calibration

Purpose of the time calibration is to convert the digital values from the **t**ime-to-**d**igital-**c**onverter (TDC) into physical time units, and to align the time information of different detectors in order to ensure a coincidence which involves those events occuring at the same time within a narrow time window. To achieve this goal the following parameters have to be determined:

- The conversion factor between the TDC output and the time unit (ns). This factor is basically defined by the electronics. However, higher accuracy can be reached through fine-tuning of this factor [47].
- The calibration offset that compensates the different signal times due to different cable lengths.

As a first step of the time-calibration, an appropriate time relation to a global time-reference has to be found. Using the trigger as time-reference is insufficient, because different trigger conditions take different decision times. For example the trigger is generated within 300 ns if a particle arrives at the MiniTAPS and/or Forward Plug detectors, which are part of the first level trigger. The Crystal Barrel detector cannot provide time information, thus it cannot contribute to the generation of the first level trigger. The second level trigger is generated by FACE within a time up to 6 μs.
To eliminate the uncertainty in the time measurement caused by the trigger, a reference detector has to be used, and all detector channels have to be aligned to this detector according to:

$$(t_{\text{detector}} - t_{\text{trigger}}) - (t_{\text{detector}_{\text{ref}}} - t_{\text{trigger}}) = (t_{\text{detector}} - t_{\text{detector}_{\text{ref}}}) \tag{4.1}$$

To have a reference detector with a good time resolution, finally every detector channel is calibrated to the 96 scintillator bars of the tagger. Plotting the time difference between all channels of the well calibrated tagger and the channels of the detector, the offsets can be determined (see figure 4.1). This calibration step is carried out for every single detector and detector channel.

4.3 Energy calibration

Electromagnetic calorimeters measure the amount of scintillation or Čerenkov light generated by an incident particle, which is proportional to the deposited energy and finally transformed into a digital signal. During the calibration, the uncalibrated digital values are transformed into calibrated physical energies.

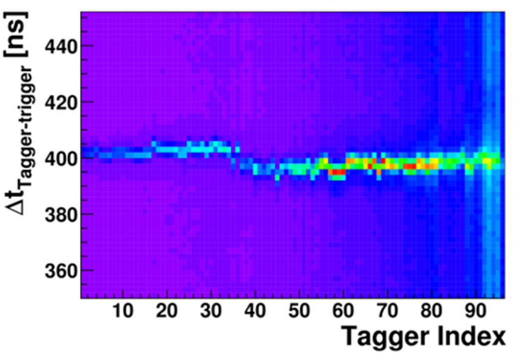

(a)

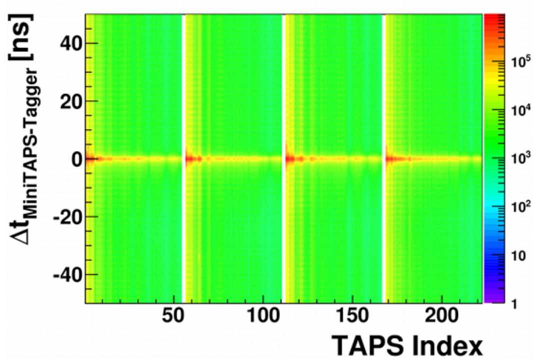

(b)

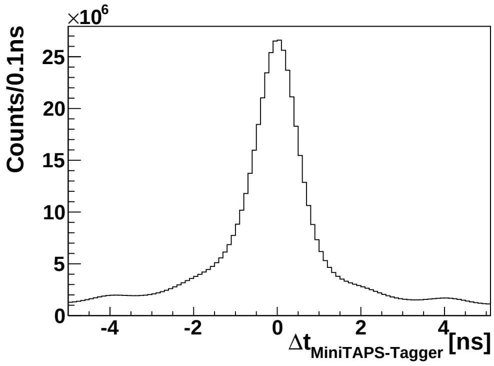

(c)

Figure 4.1: (a) $\Delta t_{\text{tagger-trigger}}$ time spectrum before the first iteration of the alignment using the trigger (the z-scale is linear).
(b) $\Delta t_{\text{MiniTAPS-tagger}}$ time spectrum after the last iteration of the alignment using the aligned tagger (the z-scale is logarithmic).
(c) Projection for all detectors showing a sharp peak with time resolution of $\sigma = 0.6$ ns in the $\Delta t_{\text{MiniTAPS-tagger}}$ spectrum. [4]

The calibration has four steps:

1. Pedestal determination for measuring the response of the electronics to a zero energy signal.
2. Cosmic calibration/preliminary alignment, to provide a rough calibration for the data taking, and setting the dynamic range of all channels to approximately the same value.
3. π^0-calibration to have a more accurate linear correlation between the QDC channel number and the energy.
4. η-calibration to check the stability of the calibration as a function of the photon energy.

4.3.1 Pedestal determination of MiniTAPS

e To find the channel number that corresponds to the zero energy, called pedestal, the detector modules have to be read-out regardless of any real physical events. In this case there will be no light generation in the scintillation crystals, and the response of the electronics to the zero energy event can be found. In order to find events without light generation, triggers were generated periodically by a digital pulser, independently of the detector status. As a consequence, the read out energy most probably will be zero in the majority of the modules. This does unfortunately not hold for detectors at extreme forward angles, which suffer from extremly high background rates due to electromagnetic processes. Whenever an artificial trigger happens, a flag will be set in the data stream to label this event.

4.3.2 Cosmic calibration

In the initial raw form, the energy response of the detector modules are unrelated, and they can give very different responses for the same stimulus. To achieve an alignment, the high voltage of the detector elements is set in a way that they respond similarly to the same stimuli. As a result of this procedure, the same dynamic range (which is

the energy range between zero energy and the largest energy that the electronics can process) will be set for every detector module and the alignment will serve as a good starting point for a high-precision calibration.
Cosmic muons were used for the alignment of the detector modules in MiniTAPS (see figure 4.2). Since all crystals of the MiniTAPS are oriented horizontally, the minimum ionizing particles (MIP) deposit most probably the same amount of energy. The cosmic muons are minimum ionizing particles and most probably they travel from up to down and deposit an energy of about 37.7 MeV while passing through laterally in every crystal [48]. If a dynamic range between zero and X is needed, the cosmic peak has to be set via High Voltage on the PMTs with the help of the expression

$$\frac{Ch_{\text{cosmic peak}} - Ch_{\text{pedestal}}}{4096 - Ch_{\text{pedestal}}} = \frac{37.7\,\text{MeV}}{X}, \tag{4.2}$$

where $Ch_{\text{cosmic peak}}$ refers to the channel number of the QDC at the maximum of the cosmic peak while Ch_{pedestal} stands for the position of the pedestal peak expressed by the channel numbers. The linear relation between the deposited energy and the measured QDC channel number allows the conversion of each QDC channel number into an energy E_i expressed by the relation:

$$E_i = (Ch_{\text{i}} - Ch_{\text{pedestal}})\,\frac{37.7\,\text{MeV}}{Ch_{\text{cosmic peak}} - Ch_{\text{pedestal}}} \tag{4.3}$$

where Ch_{i} is the channel number at the unknown energy. Cosmic calibration has to be done before every beamtime to check the gain on every crystal and, if it is necessary, to compensate them.

The gain set by cosmic calibration is not very accurate for the following reasons:

- The position of the peak is determined by fitting the data with the sum of an exponential background and a Gaussian peak-function. This parametrization is not precise enough to use the resulting gain in a high-precision data analysis.
- The described procedure is based on the energy deposit of the minimum ionizing cosmic muons, but the resulting gain has be used for photons that are not

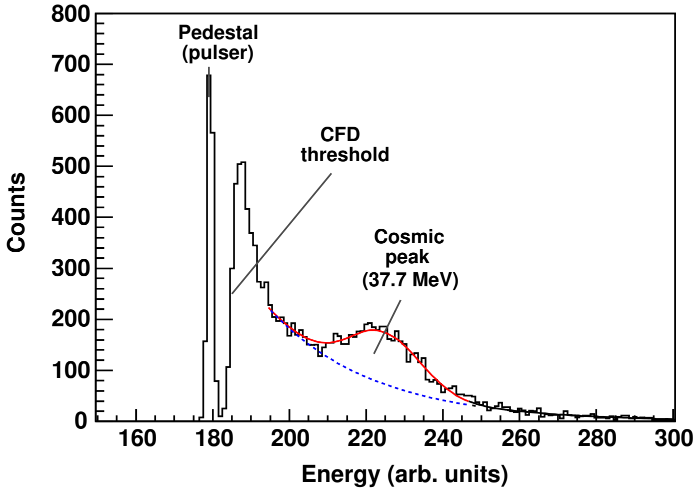

Figure 4.2: Typical cosmic muon spectrum obtained with MiniTAPS. The pedestal peak (zero energy peak), the CFD threshold and the minimum ionizing peak of cosmic muons are clearly recognizable. [49]

minimum ionizing particles.

- The linear dependence of the energy on the QDC channels was proven up to 790 MeV photon energy [34]. At ELSA, photons with much higher energies have to be measured. The use of only two low energetic data points (pedestal: 0 MeV, cosmic peak: 37.7 MeV) is not sufficient to cover the whole dynamic range up to 1.8 GeV per crystal.
- Shower leakage due to insufficient detector volume and finite thresholds leads to systematic errors in the measurement. While shower leakage affects the energy measurement of high energetic photons, the finite CFD[1] threshold has a larger impact when the energy deposit is smaller. These effects also have to be compensated during the calibration.

4.3.3 Reconstruction of primary particles

Before calibration of the electromagnetic calorimeters in energy according to the invariant mass of mesons will be explained in sections 4.3.4 and 4.3.5, the reconstruc-

[1] **C**onstant **F**raction **D**iscriminator

tion of the four-vectors of measured particles is described. The lifetime of neutral mesons, e.g. π^0-, η-, ω- and η'-mesons is so short that they decay before reaching the detector. However, these short-lived mesons can be reconstructed through their decay products, which will be registered. To reconstruct a meson from its decay photons, the deposited energy and the direction of these photons have to be measured with the greatest possible accuracy. Energetic photons, electrons and positrons generate electromagnetic showers and produce signals in several adjacent crystals. This will give rise to a local maximum in the detector. A group of responding crystals which measures the deposited energy of one single particle is called **P**article **E**nergy **D**eposit (PED). This is called a cluster. If one cluster is produced by the energy deposit of one single particle, then the names PED and cluster are interchangeable. To sum up the energy in a cluster, one element of the cluster has to be found and consecutively all its neighboring elements with energy deposition have to be added to the cluster. In order to suppress the influence of noise and artificial clusters, so called split-offs, an energy threshold is set on the crystals and in addition on the whole cluster energy (see table 4.2). Finally, if time information is available, all hits in the cluster should belong together not only in space, but also in time. In a general case, several particles can hit the detector close to each other and create adjacent groups of responding crystals. If more than one PED are registered in one cluster, the energy content of the involved crystals (first of all the crystals being located between two maxima) has to be recalculated because in these detector elements the energy deposit originates from two or more PEDs. In order to separate them, the lateral distribution of the electromagnetic shower is approximated by an exponential function whose parameters depend on the energy of the primary particle and the detector material (via its Molière radius[2]). In this case the deposited energy in the cluster can be determined by varying the positions and the total deposited energies of the contributing PEDs [50]. This method can only be applied if the shower development is symmetric, because this is the only case when the shape of the shower can be described with only one free parameter (namely the energy of the particle). In the MiniTAPS detector this symmetry requirement is not fulfilled because of the arrangement of the crystals (figure 2.12), consequently this method cannot be used there. Fortunately, inside MiniTAPS only an extremely

[2]On average only 10 % of the energy lies outside the cylinder with radius R_M and 1 % outside the cylinder with radius $3.5 \cdot R_M$.

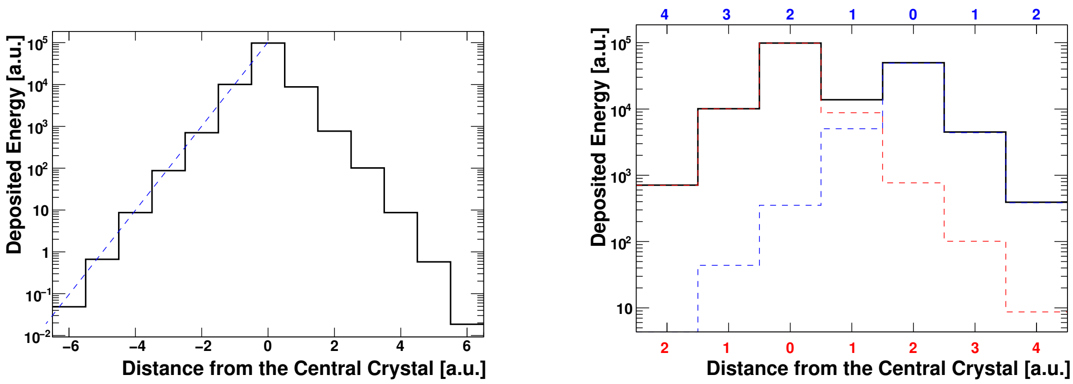

(a) The lateral energy distribution of the shower is approximated by an exponential function.

(b) Two overlapping PEDs can be resolved using an exponential approximation for the lateral shower distribution.

Figure 4.3: Separation of two PEDs in a multi-PED cluster by using exponential functions to describe the lateral shower distributions [50].

low number of multi-PED cluster is registered [51], which can be safely discarded. After determination of the correct energy content of the PED, it is possible to reconstruct the impact point of the particles. Using the lateral shower energy distribution, the impact point of photons can be reconstructed more precisely than the basic granularity of the detector. In order to determine the x and y coordinates of the impact point, the coordinates of the given crystals in the PED have to be weighted with the energy deposit within that very crystal:

$$x = \frac{\sum_{i=1}^{N} w_i x_i}{\sum_{i=1}^{N} w_i}, \qquad y = \frac{\sum_{i=1}^{N} w_i y_i}{\sum_{i=1}^{N} w_i} \tag{4.4}$$

Here N is the number of the crystals in one PED and $w_i = E_i$. However it turned out that detectors with low energy are weighted too strongly by this method. Therefore as weighting factor not the energy but the logarithm of the PED energy fraction deposited is used [52, 53]:

$$w_i = max\{0, \left[K + \ln\left(\frac{E_i}{\sum_{i=1}^{N} E_i}\right)\right]\} \tag{4.5}$$

The constant K was determined by using a GEANT simulation [49] and found to be K = 4 for BaF_2 crystals and K = 4.25 for CsI(Tl) crystals of the present geometry. Informations of energy and spatial resolution can be found in section 2.3.

4.3.4 Linear calibration

The π^0-calibration uses the precisely known invariant mass of the π^0-meson. For all possible pairs of neutral hits, the invariant mass of two photons is calculated as:

$$m_{\gamma\gamma}c^2 = \sqrt{(P_{\gamma_1} + P_{\gamma_2})^2} = \sqrt{(E_1 + E_2)^2 - (\vec{p}_{\gamma_1}c + \vec{p}_{\gamma_2}c)^2} \tag{4.6}$$

$$m_{\gamma\gamma}c^2 = \sqrt{2E_{\gamma_1}E_{\gamma_2}(1 - \cos\alpha_{\gamma_1\gamma_2})}, \tag{4.7}$$

where $\alpha_{\gamma_1\gamma_2}$ is the opening angle between the two photons, E_{γ_i} their energy, $\vec{p}_{\gamma_i}$ their three-momentum vector and P_{γ_i} their four-momentum vector. By measuring the π^0-invariant mass, the energy measured for the participant photons can be corrected. The choice of the π^0-meson for this purpose is obvious: it has both a large production yield and a high branching ratio for the decay into two photons (BR($\pi^0 \rightarrow 2\gamma$) = 0.988 [1]).
It is assumed that the real energy of the photons is linearly dependent on the measured energy: $E_{calibrated} = C \cdot E_{\text{deposited}}$., The calibration constant can be determined as:

$$C = \left(\frac{m_{\pi^0_{\text{PDG}}}}{m_{\pi^0}}\right)^2, \tag{4.8}$$

where m_{π^0} is the reconstructed π^0-mass.
In the case of the Crystal Barrel detector, events are selected with arbitrary multiplic-

ity and the invariant mass of $m_{\gamma\gamma}$ is calculated for every pair of photons where both of them are registered in this detector.
The same procedure is followed throughout the calibration of MiniTAPS, but here only events with neutral multiplicity from two to four are processed and the invariant mass $m_{\gamma\gamma}$ is calculated only for photon pairs where exactly one of the photons is registered in the MiniTAPS detector (see figure 4.4).
These masses are filled into histograms corresponding to the center crystal of the cluster produced by the given photon. If one specific module is to be calibrated, the other photon can be detected in any other crystals in the setup. Therefore the effect of this second module cancels out on average.
The invariant mass spectrum is fitted in order to determine the position of the π^0-peak. The background of this distribution is fitted by a Chebichev polynomial of the first kind up to the 5^{th} order. Due to the imperfection of the registration of the shower (finite thresholds, energy leakage, etc.), the peak can be described as a Gaussian with a stronger tail on the low-energy side. This asymmetric peak is fitted by the Novosibirsk function usually defined by:

$$f(m) = A \cdot \exp(\tau^2 - 0.5 \cdot \ln^2[1 + \Lambda \cdot \tau \cdot (m - m_0)]/\tau^2), \tag{4.9}$$

where

$$\Lambda = \sinh(\tau\sqrt{\ln 4})/(\sigma\tau\sqrt{\ln 4}) \tag{4.10}$$

In equation 4.9 m_0 is the peak position, its width is denoted by σ and τ represents the tail parameter [54, 55]. This calibration step has to be applied iteratively for each crystal until the mass of the π^0-meson will appear in the required range (see figure 4.5).

4.3.5 Second order calibration

Since the ω-meson has a larger mass than the π^0- or η-meson, it has to be confirmed whether the calibration is correct for photons from the decay of mesons with higher masses.

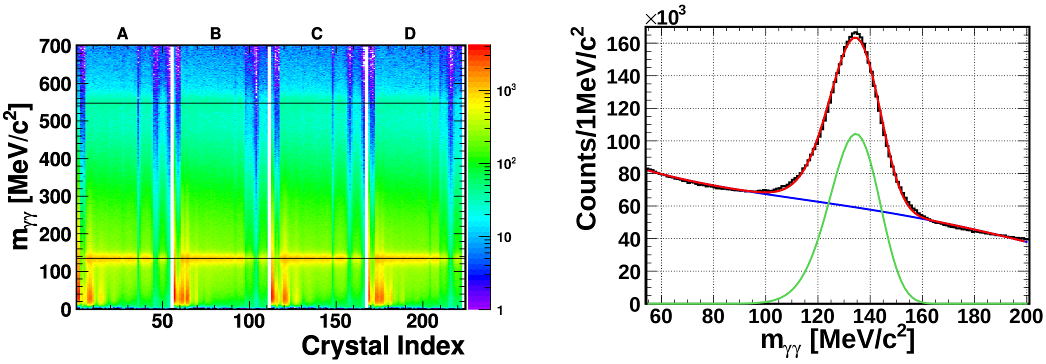

(a) (b)

Figure 4.4: (a) Two-photon invariant mass as function of the crystal index in MiniTAPS. 56 channels belong to one sector, but only 54 are read out. This is the reason why the last two channels of the sectors do not hold any information.
(b) Full projection and fit of the histogram in figure 4.4(a) to the invariant mass axis. The peak appears at 134.5 MeV/c^2 and its FWHM is 22.7 MeV/c^2, corresponding to σ = 9.6 MeV/c^2. [4]

After the proper calibration using the π^0-meson peak, a shift of the mass of the η-meson can be observed (see figure 4.6). To compensate this mass shift, a correction to the π^0-calibration should be applied. This can be the extension of the linear energy dependence to a second-order polynomial.

For the calibration of the data from the beamtimes, a polynomial calibration was applied for the MiniTAPS. The polynomial calibration extends the approximation of the linear energy dependence to a second order polynomial:

$$E_{\mathrm{cal}} = C_1 \cdot E_{dep} + C_2 \cdot E_{\mathrm{dep}}^2 \tag{4.11}$$

Using the precisely known mass of the π^0- and η-mesons, the parameters of the polynomial can be extracted.
In case of the calibration of MiniTAPS the calibration constants are:

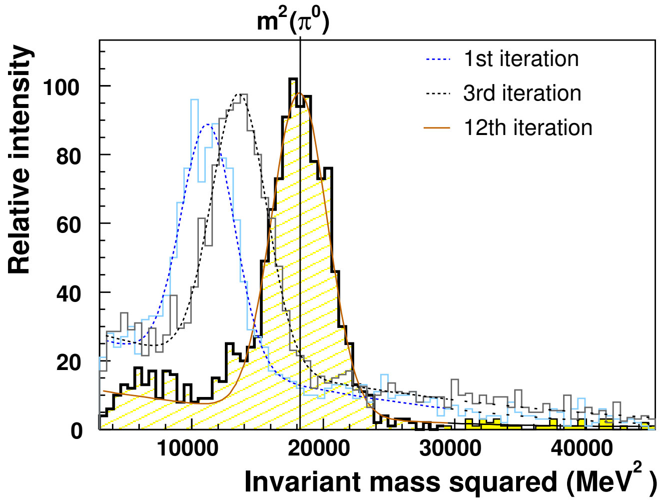

Figure 4.5: Position of the π^0-peak in the Crystal Barrel after several iterations [56].

$$C_1 = \frac{R_{\pi^0}^2 E_\eta - R_{\eta^0}^2 E_{\pi^0}}{E_\eta - E_{\pi^0}} \tag{4.12}$$

$$C_2 = \frac{R_\eta^2 - R_{\pi^0}^2}{E_\eta - E_{\pi^0}} \tag{4.13}$$

$$R_{\pi^0} = \frac{m_{\pi^0_{\mathrm{PDG}}}}{m_{\pi^0}} \tag{4.14}$$

$$R_\eta = \frac{m_{\eta_{\mathrm{PDG}}}}{m_\eta} \tag{4.15}$$

C_1 is close to unity and C_2 is of the order of 10^{-5}-10^{-4}. E_{π^0} and E_η are the measured total energies and m_{π^0} and m_η are the reconstructed masses of π^0- and η-mesons.
If both photons have unknown energies and are measured by the Crystal Barrel detector, the expressions are slightly different. This correction was also used iteratively for each crystal until the invariant mass peaks of both π^0- and η-meson were in the right position.

In the innermost ring the signal-to-noise ratio is very low because of the high rate of forward boosted electromagnetic particles. Hence, these crystals could not be calibrated similarly to the others. Merely an average gain was set, which was deduced from the gain of the calibrated detectors.

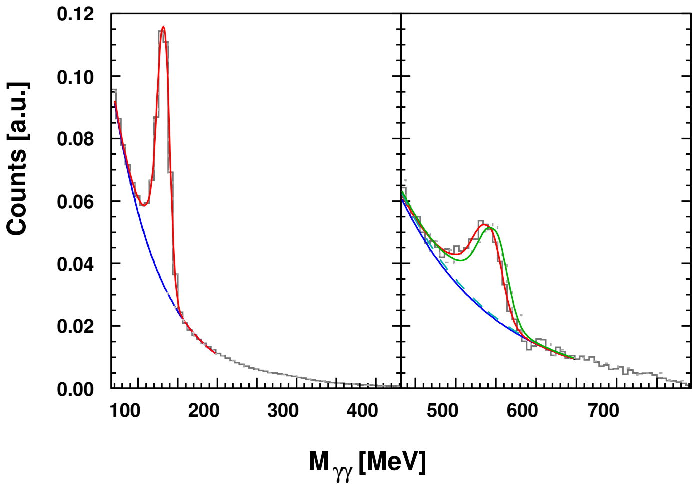

Figure 4.6: The position of the π^0- (left) and η-meson invariant mass (right) before and after polynomial calibration. The blue curve shows the background contribution. The position of the pion is unchanged, while the position of the η-meson is shifted down roughly by 10 MeV/c^2 to the nominal mass of the η-meson. [4]

4.3.6 Final check of the energy calibration

An accurate energy calibration is essential because imprecisely determined energies result in imprecise invariant masses. In figures 4.7 and 4.8 the invariant mass of the π^0- or η-meson as function of the crystal number of the detectors is shown. In figures 4.7(a) and 4.7(b) one finds the case where two photons are registered in the Crystal Barrel and Forward Plug detector. Analogously, figures 4.7(c) and 4.7(d) show the case if one photon is registered in the Crystal Barrel and Forward Plug and the other one in the MiniTAPS detector. For all cases the vast majority of crystals is calibrated within 0.5% relative deviation of the meson mass. As mentioned above, the inner most crystals of MiniTAPS could not be calibrated properly.

Figure 4.8 shows the reconstructed π^0-invariant mass for the case that both photons are registered in the MiniTAPS detector. All crystals are calibrated within a deviation of 1%, except for the inner most ones. Please note that due to angular acceptance and reaction kinematics no η-meson can be reconstructed from photons only in MiniTAPS. The opening angle between the two decay photons is too large.

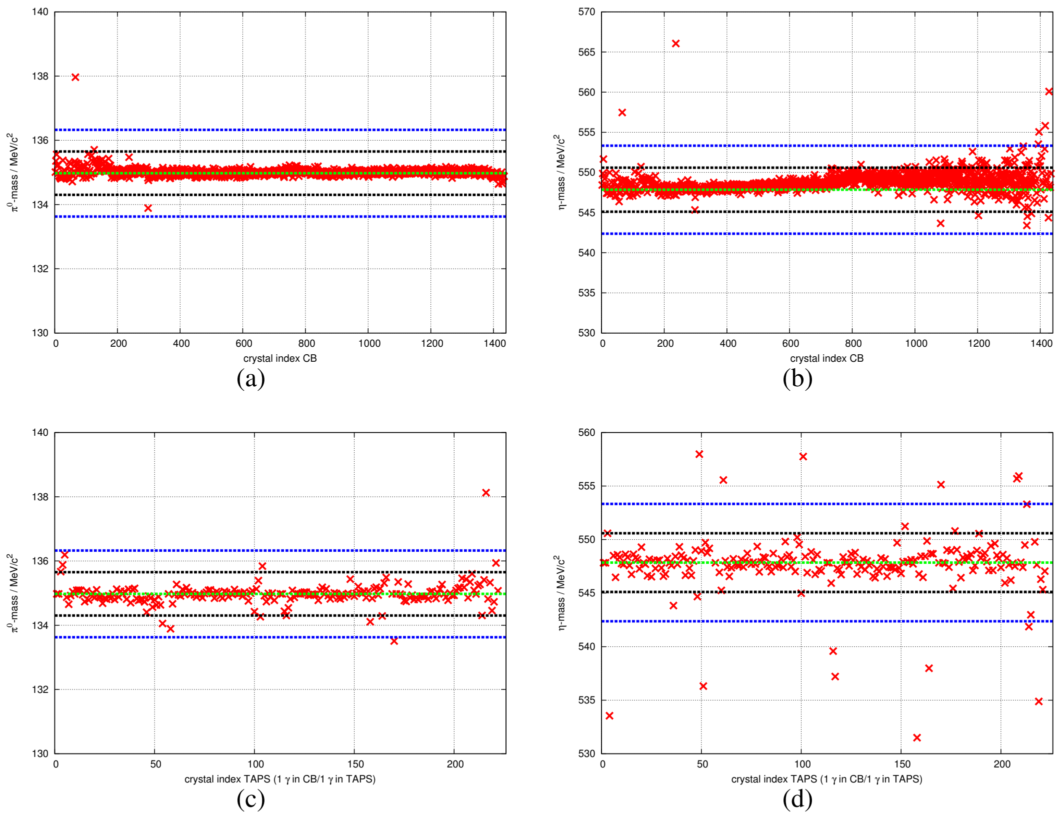

Figure 4.7: Energy calibration check for each crystal (carbon beamtime, January 2009). For figures (a) and (b) the index range between 1 and 180 refers to the Forward Plug. Green lines show the position of the nominal meson masses. The other lines show relative deviations: 0.5% (black) and 1.0% (blue).
(a) and (b): Reconstructed π^0-/η-invariant mass for two photons in CB + FwPlug.
(c) and (d): Reconstructed π^0-/η-invariant mass for one photon in CB + FwPlug and one photon in MiniTAPS.
Except for the most inner crystals in MiniTAPS, all crystals are calibrated within 0.5% relative deviation of the meson mass.
Corresponding figures for the LH_2 data (October 2008) are given in appendix E.

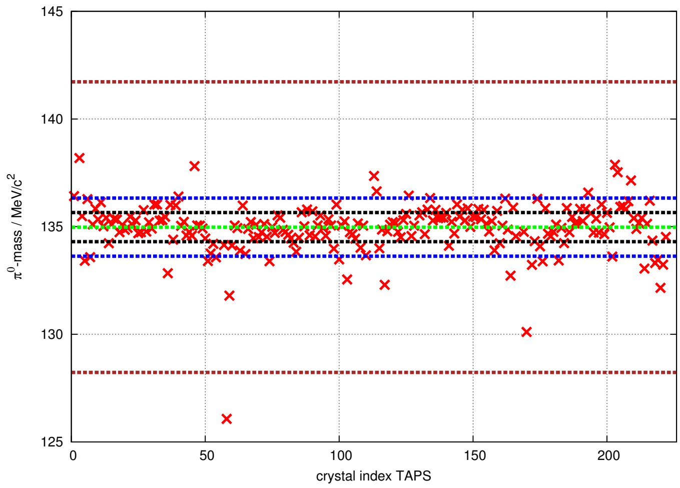

Figure 4.8: Reconstructed π^0-invariant mass for two photons in MiniTAPS (carbon beamtime, January 2009). The green line shows the position of the nominal pion mass. The other lines show relative deviations: 0.5% (black), 1.0% (blue) and 5.0% (brown). Except for the inner most crystals, all crystals are calibrated within 1.0% relative deviation of the pion mass. The corresponding figure for the LH_2 data (October 2008) is given in appendix E.

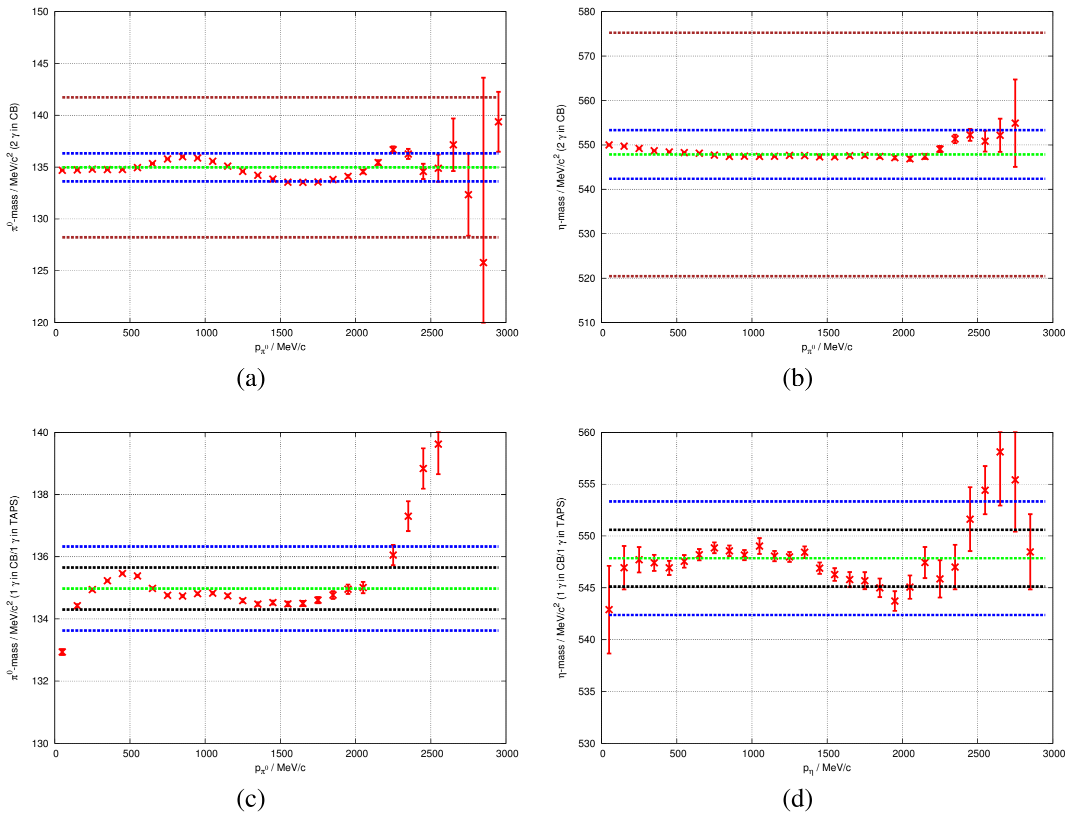

Figure 4.9: Reconstructed π^0-/η-invariant mass as function of the reconstructed meson momentum (carbon beamtime, January 2009). Green lines show the position of the nominal meson masses. The other lines show relative deviations: 0.5% (black) and 1.0% (blue).
(a) and (b): Reconstructed π^0-/η-invariant mass for two photons in CB + FwPlug.
(c) and (d): Reconstructed π^0-/η-invariant mass for one photon in CB + FwPlug and one photon in MiniTAPS.
The invariant masses are stable within $\pm 1.0\%$ in the momentum range of 100 MeV/$c < p_{\gamma\gamma} <$ 2300 MeV/c.
Corresponding figures for the LH_2 data (October 2008) are given in appendix E.

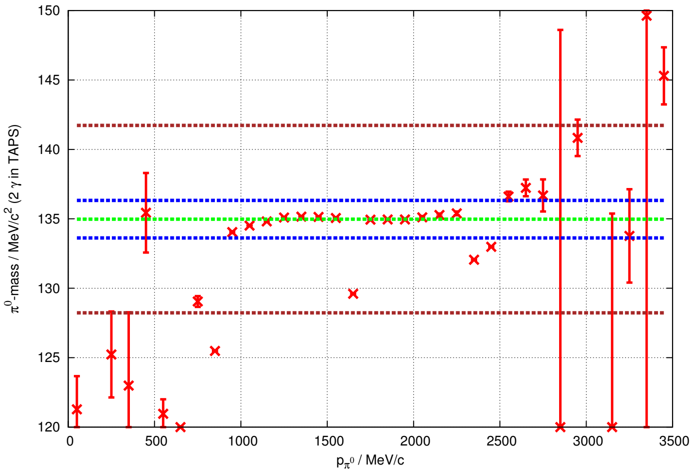

Figure 4.10: Invariant mass of π^0-mesons as a function of their momenta for two photons in MiniTAPS (carbon beamtime, January 2009). The error bars show the fitting error of the peak position. The green line shows the position of the nominal pion mass. The other lines show relative deviations: 0.5% (black) and 1.0% (blue).
The invariant masses are stable within $\pm 0.5\%$ in the momentum range of 900 MeV/c < $p_{\gamma\gamma}$ < 2300 MeV/c.
The corresponding figure for the LH_2 data (October 2008) is given in appendix E.

After properly calibrating every crystal with the second-order polynomial, one has to ensure that the reconstructed meson mass does not depend on its momentum. The invariant mass of two photons as a function of the momentum of the two-photon pair is plotted in figures 4.9 and 4.10. The peak position of the π^0- and η-meson was determined for 100 MeV/c wide momentum slices projected on the invariant mass axis. The positions of the meson masses are within $\pm 1\%$ around the nominal values for momenta between 100 MeV/c and 2400 MeV/c for the cases that both photons are in the Crystal Barrel and Forward Plug or that one photon is in the Crystal Barrel and Forward Plug and one in the MiniTAPS detector. For the case that both photons are in the MiniTAPS detector the reconstructed π^0-invariant mass over momentum is plotted in figure 4.10. The peak positions in the momentum range between 900 MeV/c and 2300 MeV/c are stable within $\pm 0.5\%$. For other momenta the statistics is too poor to allow for a reasonable fit result.

Detector	Type	Applied cut interval [ns]
Tagger	prompt peak	-7 $\leq t \leq$ 4
Inner Detector (+ hit in Crystal Barrel)	charged	-2 $\leq t \leq$ 3
Forward Plug	charged	-3 $\leq t \leq$ 8
Forward Plug	neutral	-3 $\leq t \leq$ 3
MiniTAPS	charged	-1.5 $\leq t \leq$ 20
MiniTAPS	neutral	-1 $\leq t \leq$ 1
Aerogel-Čerenkov	prompt peak (anti-cut)	-20 $\leq t \leq$ 8

Table 4.1: Overview of the applied time cuts.

4.4 Event selection

Since in this work ω-mesons are identified via the $\omega \rightarrow \pi^0\gamma$-decay, events with at least three hits in the detectors are of interest for the analysis. The trigger conditions used in the various beamtimes were chosen such that already events with three or four hits were selected(see chapter 3 and appendix D). In the analysis, events with exactly three neutral and exactly one charged hit were selected. To distinguish between a neutral and a charged hit, the information of the MiniTAPS- and Forward Plug veto detector and the Inner Detector were used, since they react only on charged particles like protons, charged pions or electrons/positrons. For the selection, tight time cuts on detectors which provide time information were applied (see figures 4.11 and 4.12 and table 4.1). The Crystal Barrel detector does not provide time information by itself, but for a charged hit the Inner Detector has responded so a cut on this time spectrum is possible. Strict time cuts are necessary to suppress random coincidences and therefore background. Cuts on the neutral particles can be tight since photons travel with the speed of light and should be prompt. Of course, due to the limited time resolution the contribution of fast neutrons to the prompt peak cannot be completely excluded. The identification of charged hits is hampered by the fact that not every charged particle is registered by the detector.

By application of further cuts the identification probability is very much enhanced that the selected neutral particles are photons and the charged hit is a proton (see below).

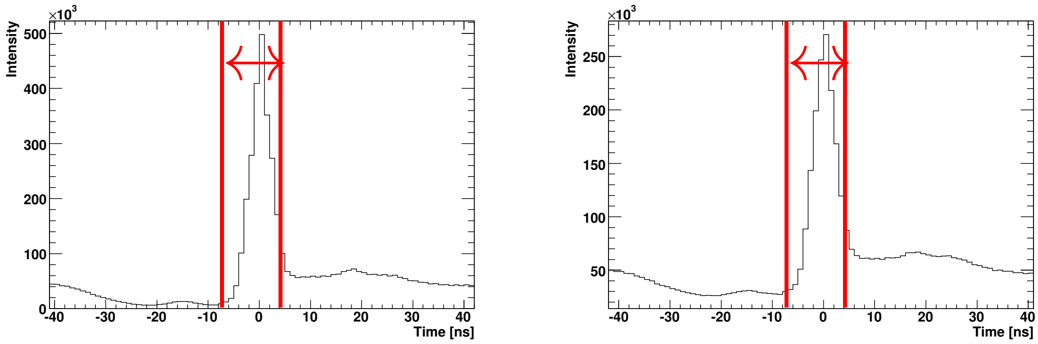

(a) (b)

Figure 4.11: Time distributions of hits in the tagger scintillation detectors: (a) Tagger bars and (b) tagger fibers (LH_2 beamtime, October 2008). The cut limits are shown in table 4.1.

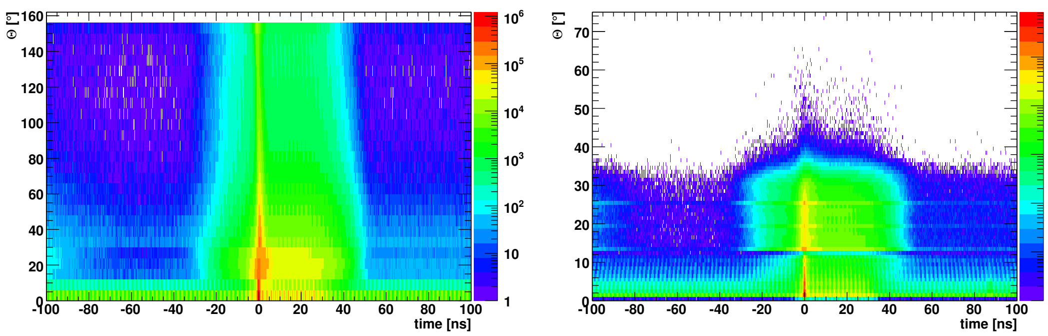

(a) (b)

Figure 4.12: Two-dimensional plot of polar angle vs. calibrated time for particles marked as "charged" or "neutral" depositing energy in the scintillation crystals (LH_2 beamtime, October 2008). For this distinction the readout information of Inner Detector, Forward Plug veto detector and MiniTAPS veto detector are used. Please note that the Crystal Barrel detector itself does not provide time information. The cut limits for the various detectors are shown in table 4.1.

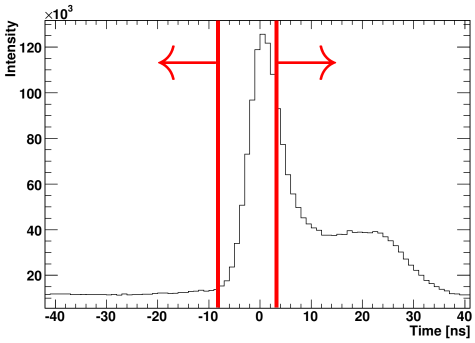

(a)

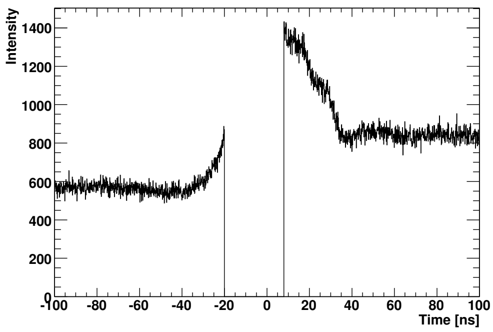

(b)

Figure 4.13: Aerogel-Čerenkov detector time distribution (LH_2 beamtime, October 2008) (a) before the anti-cut and (b) after the anti-cut on the prompt peak.

In section 1.4 it was shown that a forward going proton takes over almost all of the momentum of the incident photon. Consequently, it was required that the charged hit must be in the MiniTAPS detector which covers an angular range in Θ of 1°-11° (see figure 4.14(b)). Since an aerogel-Čerenkov detector was placed in front of the MiniTAPS detector, it was possible to discriminate between electrons, positrons and charged pions (which fire the detector) and protons (which pass the detector unseen) (for details see section 2.3.6). Depending on the beamtime, it was either already requested in the hardware trigger condition that the aerogel-Čerenkov detector has not fired within a certain time window (veto mode) or an anti-cut on the time spectrum of the detector was placed (see figure 4.13). To identify protons positively in the BaF_2 modules, the characteristic correlation of deposited energy and time-of-flight has been exploited. In figure 4.15 one can see the applied proton band cut for events where all other cuts have been applied as well.

For an effective suppression of the background contributions from $\pi^0\pi^0$- and $\pi^0\eta$-channels several kinematical cuts were applied on the selected events. Only events with incident photon energies larger than 1250 MeV were processed (see figure 4.14(a)), because the cross section for $\pi^0\pi^0$-production rises towards lower energies, although the threshold for production on the free nucleon is 1108 MeV. All neutral particles were required to have energies larger than 50 MeV to suppress split-

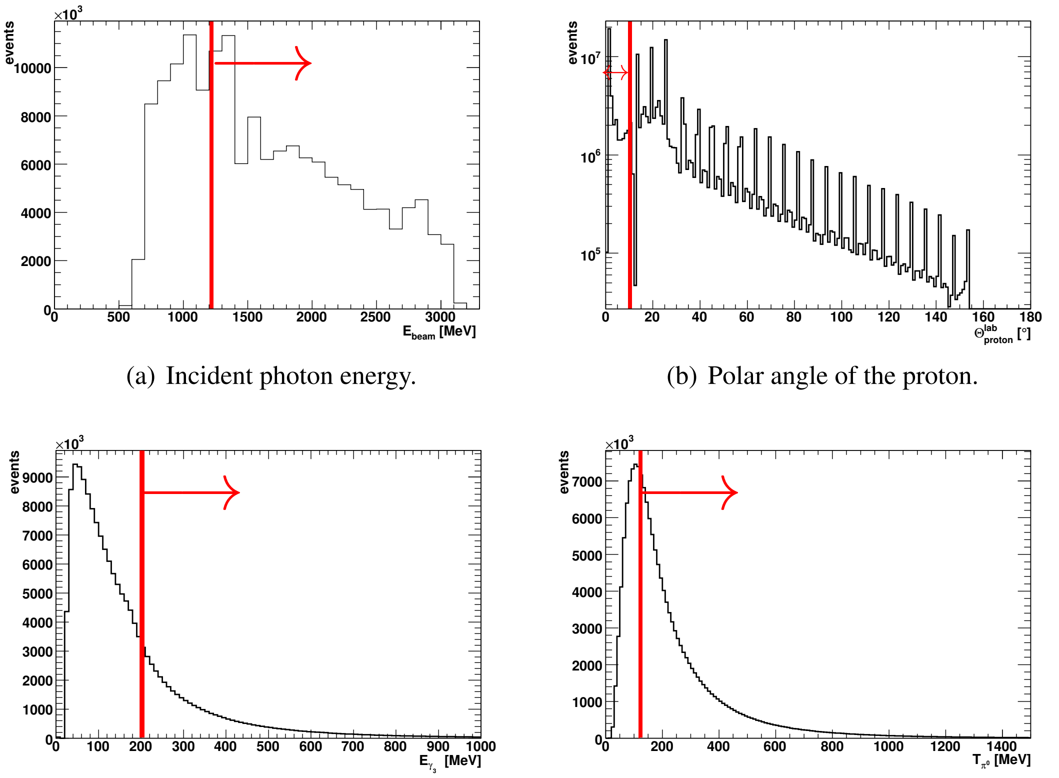

(a) Incident photon energy.

(b) Polar angle of the proton.

(c) Energy of the bachelor photon.

(d) Kinetic energy of the reconstructed pion.

Figure 4.14: Spectra of selected kinematic quantities (carbon data). The cut limits are indicated by red lines and arrows.

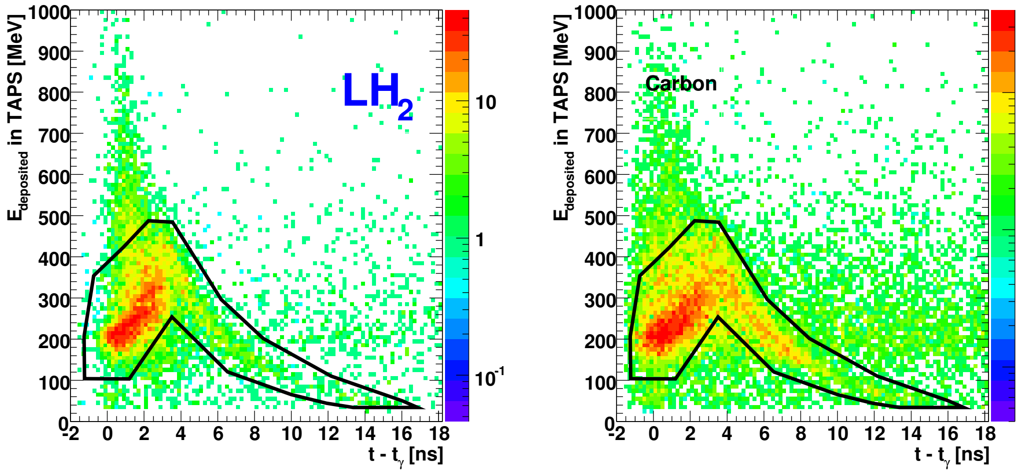

(a) (b)

Figure 4.15: Energy deposited inside the MiniTAPS detectors as a function of the time-of-flight relative to photons. The proton band cut is indicated for (a) LH_2 data and (b) carbon data for events where all other cuts described in table 4.2 are applied. A direct comparison to simulation can be found in figure 5.4.

off events from photons. In order to identify photons more effectively, only those registered in the polar angle range of 14°-156°, which means not in the MiniTAPS detector, were taken. With three photons per event the invariant masses of all photon pairs were calculated and the one closest to the nominal invariant mass of 134.97 MeV/c^2 was taken to emerge from the neutral pion. The remaining bachelor photon has to have an energy of at least 200 MeV (see figure 4.14(c)), since photons from the $\pi^0\pi^0$-decay have in most cases lower energies [57]. Events with rescattered π^0-mesons from the ω-decay within the nucleus were suppressed by requesting the kinetic energy of the pion to be larger than 120 MeV (see figure 4.14(d))[58]. In addition, a missing mass cut MM(γN$\pi^0\gamma$) was applied. The missing particle is a proton; subtracting the rest mass of m_p = 938.27 MeV/c^2 the expectation value is zero. For the hydrogen data a cut from -80 to 100 MeV/c^2 was applied, for the carbon data a cut which linearly widened towards higher incident photon energies (see figures 4.16 and 4.17). The last cut which is used to prepare the signal is a cut in the two-dimensional plane of the polar angle vs. the energy of the third (bachelor) photon from the ω-decay (see figure 4.18). The reason for this is to suppress background contribution from the $\pi^0\pi^0$-decay channel. GEANT3 simulations for this channel have shown that the main contribution lies below the line indicated in figure 4.18 [4]. Figure 4.19 shows the influence of different cuts on the $\pi^0\gamma$-invariant mass spectrum by subsequently applying the cuts. The strongest impact has the restriction on the proton angle and the missing mass cut, since the four-vectors of ω-meson and proton are directly related in free production.

Figure 4.20 shows the yield of the reconstructed $\pi^0\gamma$-pairs in a two-dimensional plot as a function of the $\pi^0\gamma$-invariant mass and the total energy of the $\pi^0\gamma$-pair minus the mass of the free ω-meson of 782.65 MeV/c^2. In the region of an invariant mass of 700-850 MeV/c^2 one can clearly see an ω-signal on a background. As mentioned earlier, this background stems from $\pi^0\pi^0$- and $\pi^0\eta$-decays into four photons where one photon escapes detection. This fact allows to describe the background by the same data set as follows: Events with exactly four neutral and one charged hit are selected and afterwards one neutral is omitted irrespective of angle and energy. All cuts which are described above (see table 4.2) are applied and all four possible combinations of three neutral hits out of four are considered. Thus, four possible three

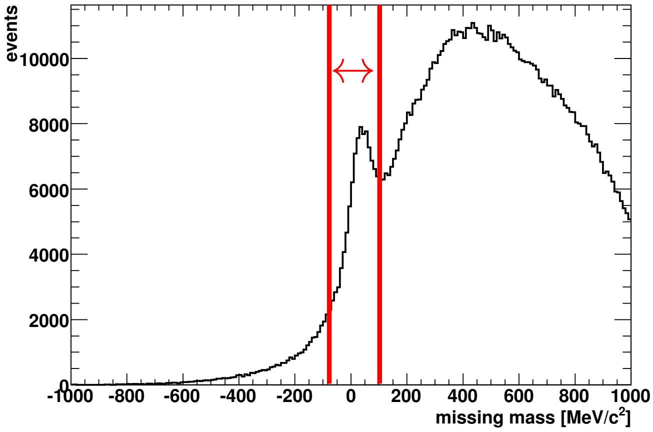

Figure 4.16: Missing mass distribution MM($\gamma N \pi^0 \gamma$) for the LH_2 data. The cut limits are indicated by red lines.

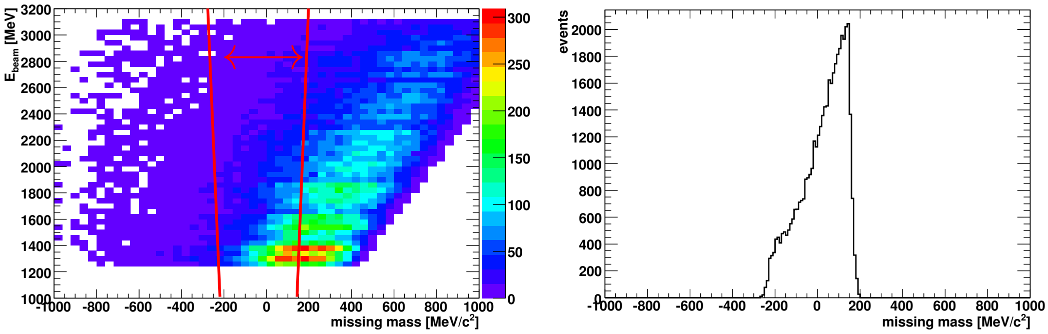

(a) (b)

Figure 4.17: Missing mass distribution MM($\gamma N \pi^0 \gamma$) for the carbon data. (a) Incident photon energy as a function of the missing mass. The cut limits are indicated by red lines.
b) The projection onto the x-axis after the applied cut.

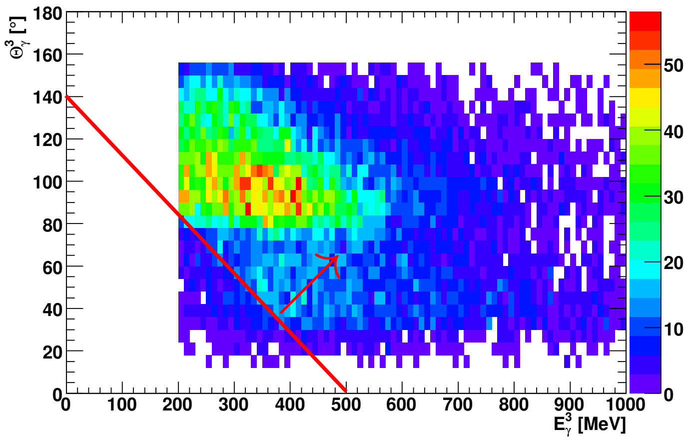

Figure 4.18: Two-dimensional spectrum of the polar angle of the bachelor photon as a function of its energy (carbon data). Events in the area indicated by the arrow are analyzed further.

Cut	Applied restriction	Figure
Incident photon energy	$E_{beam} > 1250$ MeV	4.14(a)
Proton polar angle	$1° < \Theta_{proton} < 11°$	4.14(b)
Identification of proton	proton band cut (ΔE vs. TOF)	4.15
Photon polar angle	$14° < \Theta_\gamma < 156°$	
Photon cluster energy	$E_\gamma > 50$ MeV	
Relative angle of photons	$\sphericalangle\ \gamma_i\gamma_j > 20°$	
Relative angle of photon and proton	$\sphericalangle\ \gamma_i$ proton $> 20°$	
Mass of reconstructed pion	110 MeV/$c^2 < m_{\pi^0} <$ 160 MeV/c^2	
Kinetic energy of reconstructed pion	$T_{\pi^0} > 120$ MeV	4.14(d)
Energy of bachelor decay photon	$E_{\gamma^3} > 200$ MeV	4.14(c)
Correlation of polar angle and energy of bachelor photon	$\Theta_{\gamma^3} >$ -0.28 $\frac{°}{MeV} \cdot E_{\gamma^3}$ +140°	4.18
Missing mass cut (LH_2 data)	-80 MeV/c^2 < MM < 100 MeV/c^2	4.16
Missing mass cut (carbon data)	$E_{beam} >$ -39$c^2 \cdot$ MM - 7500 MeV $\wedge\ E_{beam} > 39c^2 \cdot$ MM - 4600 MeV	4.17

Table 4.2: Overview of the applied kinematic cuts. For details see text and indicated figures.

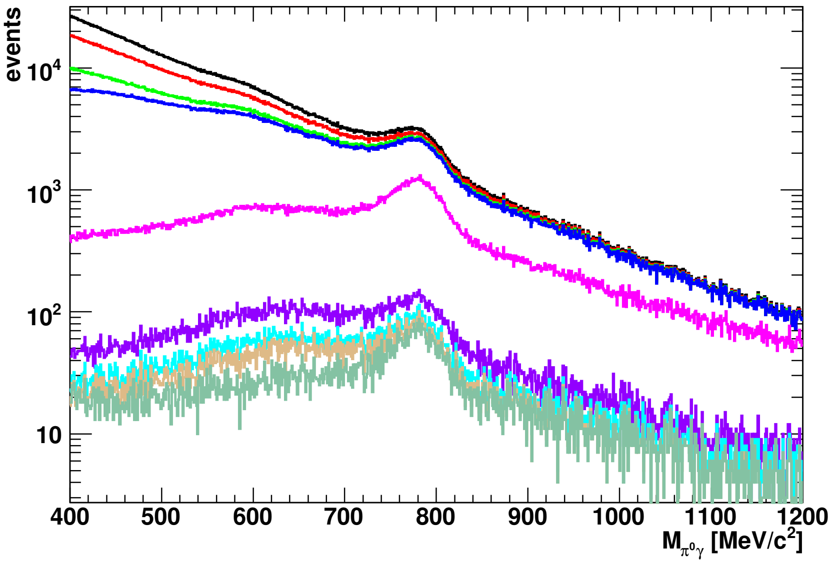

Figure 4.19: $\pi^0\gamma$-invariant mass spectrum after subsequent application of different cuts (carbon data). The first four histograms show the impact of the following cuts: no cut (black), E_{beam} (red), E_{γ^3} (green), T_{π^0} (blue). As a result, the shape of the spectra is hardly changed. In contrast, the missing mass cut drastically reduces the background (pink) and enhances the signal to background ratio. The cut on the proton polar angle reduces the statistics a lot (violet). The proton band cut reduces background since the proton is identified explicitly and not only a "charged" particle (light blue). The beige histogram shows the distribution after additionally applying the cuts on the relative angles, the energies of the single photons and the restriction for photons not to be registered in the MiniTAPS detector. In the last step (grey) the cut on the polar angle vs. energy of the bachelor photon is applied.

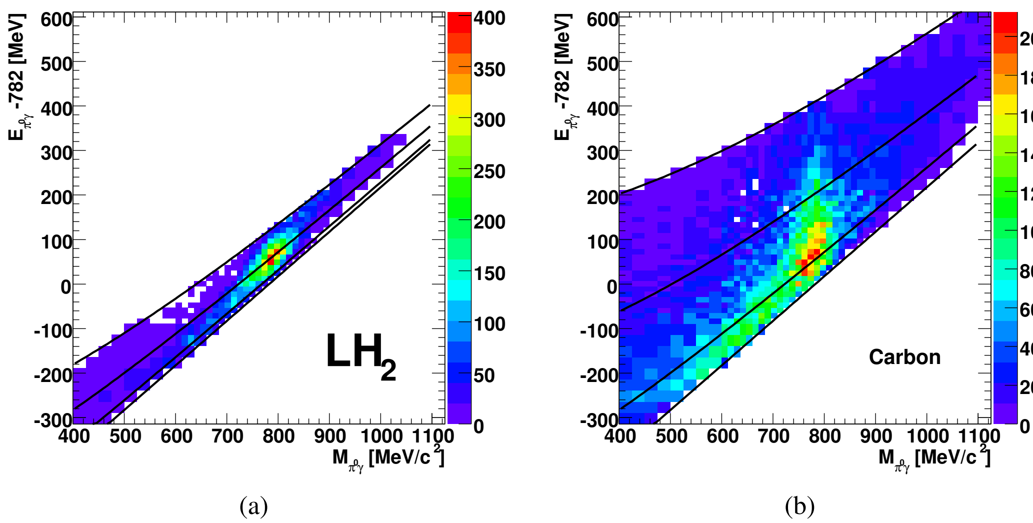

Figure 4.20: Signal spectrum with background contribution.
Two-dimensional plot of total $\pi^0\gamma$-energy minus 782.65 MeV vs. the $\pi^0\gamma$-invariant mass for (a) LH$_2$ data and (b) carbon data. Black lines indicate constant $\pi^0\gamma$-momenta: (a) 0, 150, 300, 450 MeV/c, (b) 0, 300, 600, 900 MeV/c.

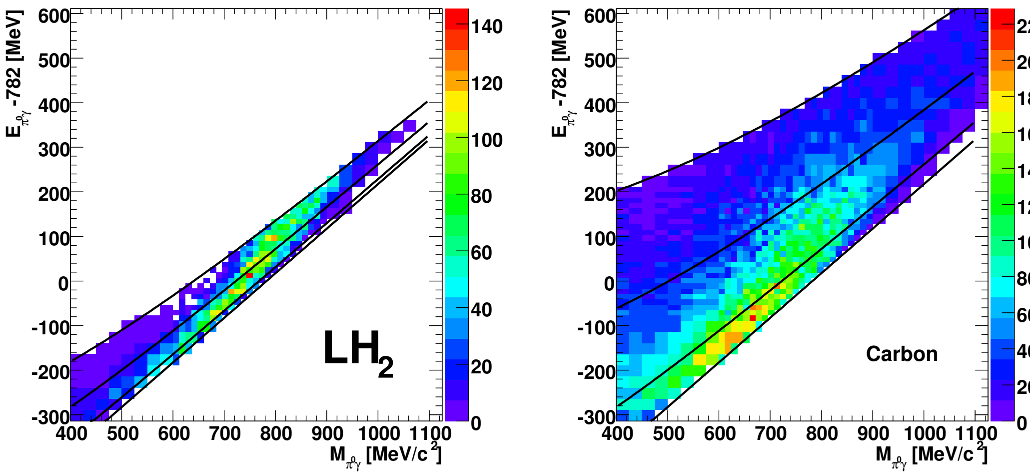

(a) (b)

Figure 4.21: Background spectrum (not scaled): Two-dimensional plot of total $\pi^0\gamma$-energy minus 782.65 MeV vs. the $\pi^0\gamma$-invariant mass for events with four neutral and one charged hit in MiniTAPS for (a) LH_2 data and (b) carbon data. One of the four photons has been omitted in the analysis.

neutral hit events are generated out of one event with four neutral hits. With that procedure one obtains distributions that describe the shape of the background quite well. Figure 4.21 shows the two-dimensional background. The projections onto the axes are plotted in figures 4.22 and 4.23.

In order to subtract the background from the data, one has to scale it since the analysis took all events with four neutral and one charged hit into account. The normalization was done for slices in momenta. In the hydrogen case a region of 0 - 450 MeV/c in 150 MeV/c wide slices was used while for the carbon data a range of 0 - 900 MeV/c in 300 MeV/c wide slices was used. The upper limit for the considered momentum of the $\pi^0\gamma$ is determined by the kinematics of the process and the condition for the polar angle of the proton to be in the MiniTAPS detector, while Fermi motion of the nucleons in carbon allows for a larger range of possible momenta. The width of the slices was limited by the statistics of the data set. The momentum slices (indicated by the black lines in figures 4.21 and 4.24) were normalized to the counts in the signal spectra within the background area of an invariant mass of 400 - 600 MeV/c^2 and

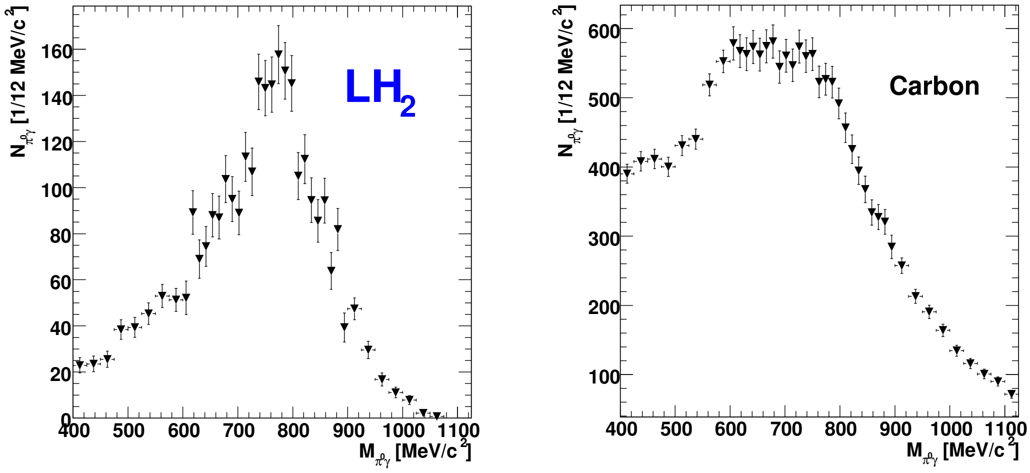

(a) (b)

Figure 4.22: $\pi^0\gamma$-invariant mass background spectrum (not scaled) for (a) LH_2 data and (b) carbon data.

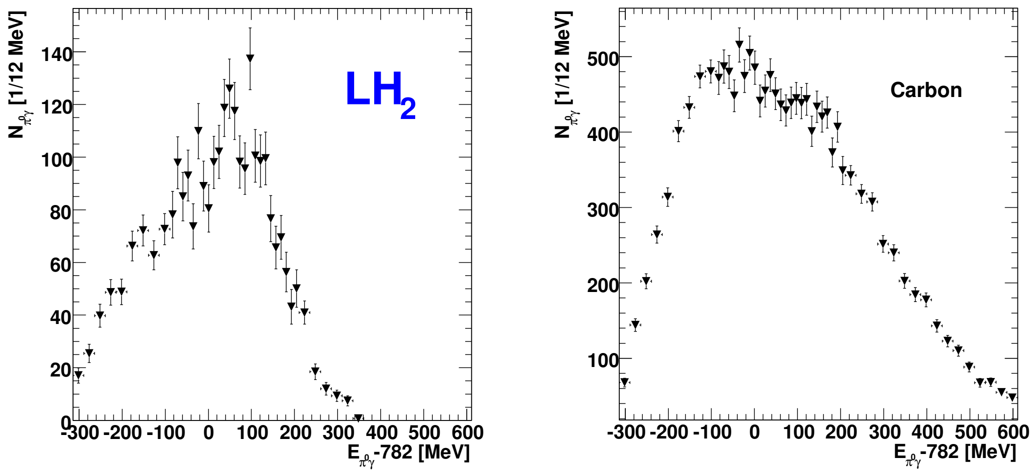

(a) (b)

Figure 4.23: $E_{\pi^0\gamma}$ - 782.65 MeV background spectrum (not scaled) for (a) LH_2 data and (b) carbon data.

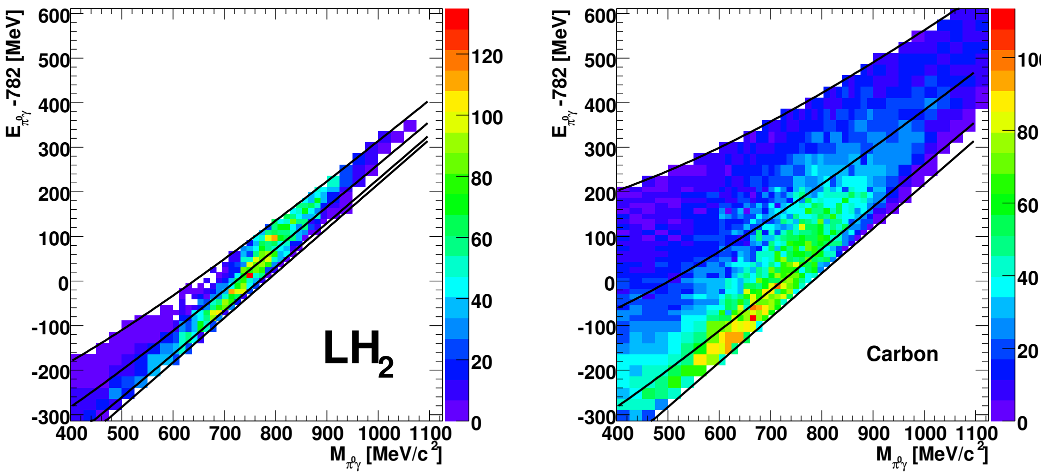

(a) (b)

Figure 4.24: Background spectrum (scaled): Two-dimensional plot of total $\pi^0\gamma$-energy minus 782.65 MeV vs. the $\pi^0\gamma$-invariant mass for events with four neutral and one charged hit in MiniTAPS for (a) LH_2 data and (b) carbon data. One of the four photons has been omitted in the analysis. The spectrum has been scaled within momentum slices (for details see text).

864 - 1200 MeV/c^2; well outside of the ω-meson signal region. The scaling factors for each slice were smoothly decreasing with higher momentum. The result is shown in figure 4.24; the projections onto the invariant mass axis and onto the total energy axis are shown in figure 4.25 and in figure 4.26, respectively.

The background, normalized as described above, can now be subtracted. For the two-dimensional plane the result is shown in figure 4.27. Please note that, because of statistical fluctuations, negative counts are possible. The projections onto the axes yield figures 4.28 and 4.29, respectively. Statistical errors were determined from the signal (S) and the background (B) yields according to the formula ΔS=$\sqrt{S+2B}$. The systematic uncertainties are not included in the errorbars; they will be discussed in section 7.2. These are the resulting spectra of the analysis of the experimental data.

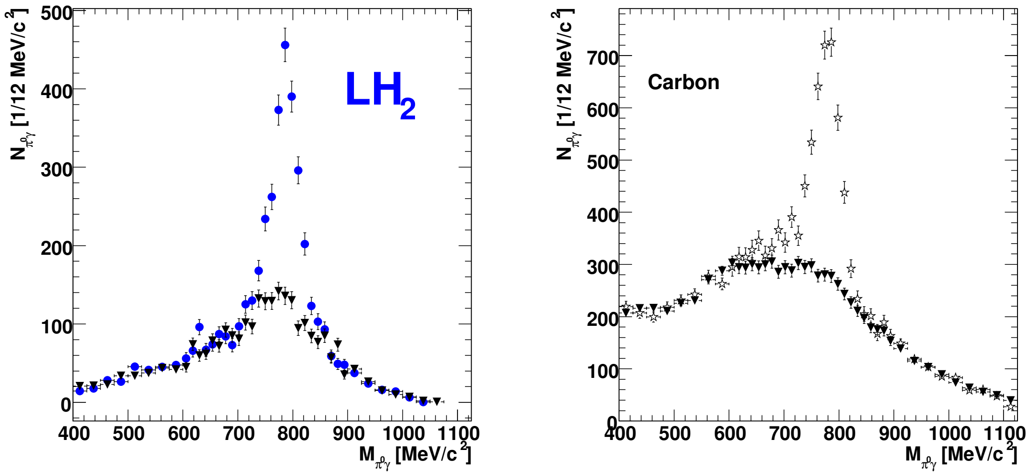

(a) LH_2 data (blue points). (b) Carbon data (black open stars).

Figure 4.25: $\pi^0\gamma$-invariant mass signal with normalized background contribution (scaled, black triangles).

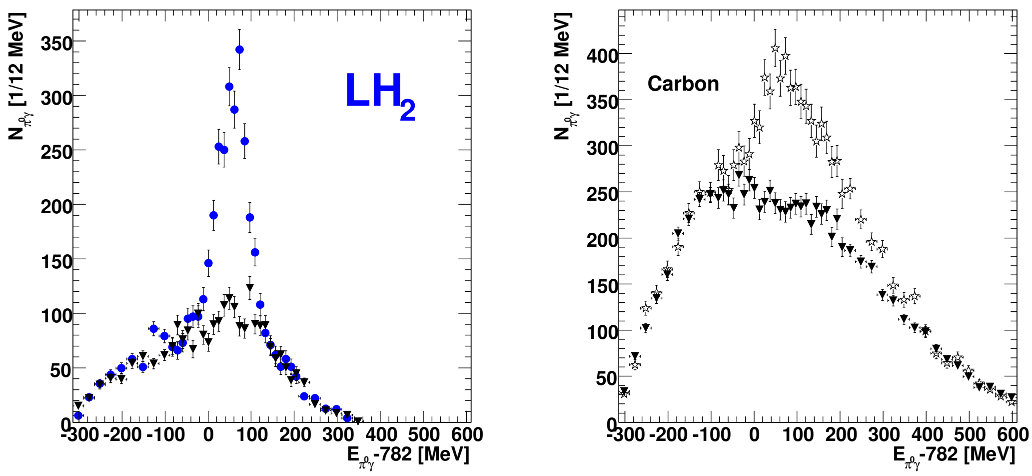

(a) LH_2 data (blue points). (b) Carbon data (black open stars).

Figure 4.26: $E_{\pi^0\gamma}$ - 782.65 MeV signal spectrum with normalized background contribution (scaled, black triangles).

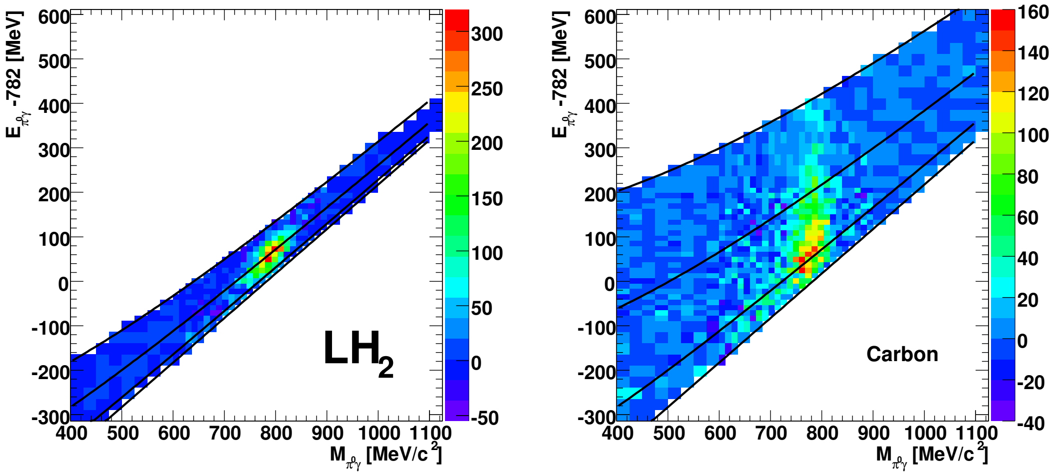

(a) (b)

Figure 4.27: Two-dimensional signal spectrum after background subtraction for (a) LH_2 data and (b) carbon data.

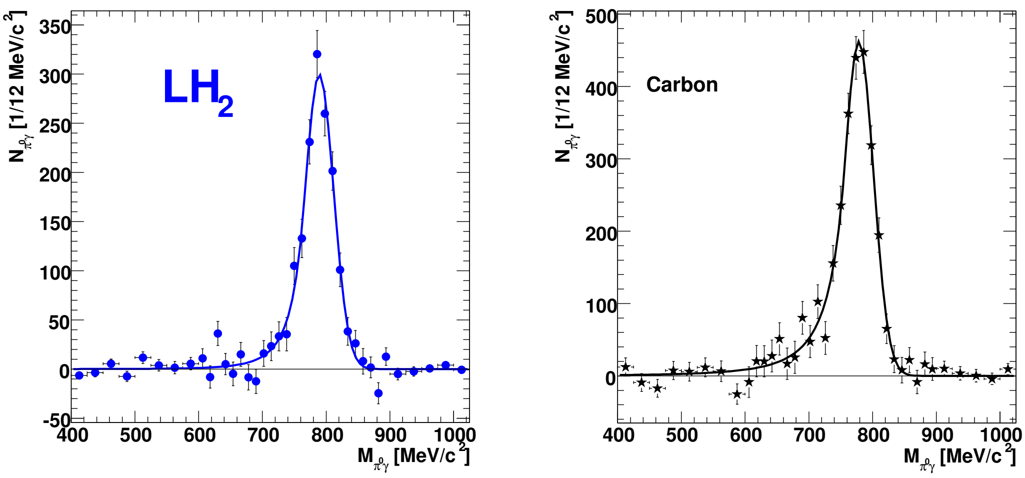

(a) (b)

Figure 4.28: $\pi^0\gamma$-invariant mass signal after background subtraction for (a) LH_2 data and (b) carbon data. Both distributions are fitted with the Crystal Ball function [59]. The widths are $\sigma_{LH_2} = 22.5$ MeV and $\sigma_{carbon} = 23.0$ MeV.

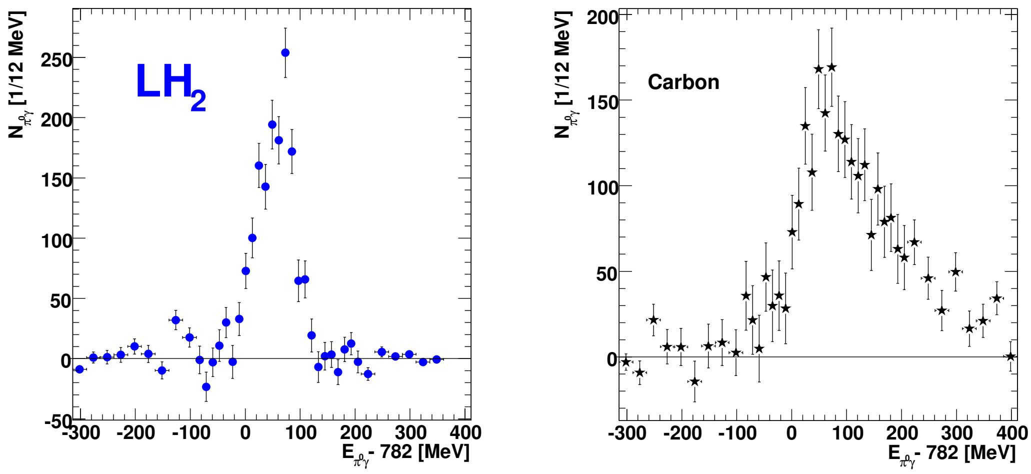

(a) (b)

Figure 4.29: $E_{\pi^0\gamma}$ - 782.65 MeV signal spectrum after background subtraction for (a) LH_2 data and (b) carbon data.

4.5 Photon flux determination

The cross section is calculated according to:

$$\sigma = \frac{N_{event}}{\epsilon \cdot n_{target} \cdot N_\gamma \cdot BR} \tag{4.16}$$

An important experimental quantity to determine an absolute cross section is the flux of the incoming photon beam N_γ on the target (see formula 4.16). Since the tagging efficiency of electrons which emitted bremsstrahlung is not unity and since the photon beam is collimated in front of the target by tungsten collimators of various sizes (4 - 7 mm), one has to determine the experimental tagging efficiency to be able to calculate the real photon flux. In addition, a hadronic reaction can only be registered during the live time of the data acquisition. On the trigger level a hit in one of the tagger bars is already requested, therefore only the fraction of photons which can be tagged should be taken into account. At the end of the CBELSA/TAPS beamline the GIM-detector is positioned (see section 2.3.7). To determine the actual photon flux on the target while the data acquisition system is ready, one has to measure the probability that a produced photon is registered. This value P_γ depends on the collimator size

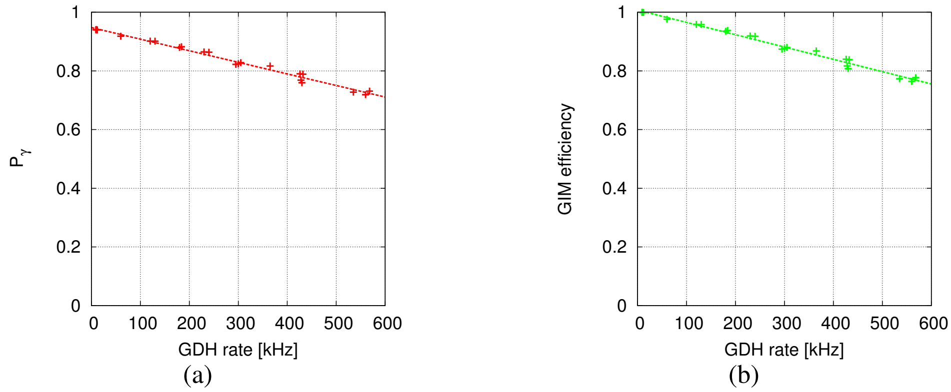

Figure 4.30: Tagger rate dependency for (a) the P_γ-value and (b) deduced GIM efficiency derived by (a) (Niobium beamtime, January 2014).

and on the hit rate of the tagger bars. One has to take into account the efficiency of the GIM detector as well, since this drops with higher rates leading to a reduced detection efficiency for the produced photons. During beamtime in January 2014 on a Niobium target with a slightly different detector setup the tagger rate dependence of the P_γ value was measured in dedicated tagger runs. Figure 4.30(a) shows the dependency of P_γ on different rates in the tagger (the so called GDH rate is the rate on several tagger bars used). It clearly decreases linearly with rate from 95% for a very low intensity down to about 70% for the intensity used for data taking. Assuming that the GIM efficiency is unity for the lowest intensity one derives figure 4.30(b).

In order to determine the P_γ value for the data files one has two possibilities: The first one is to measure with very low beam intensity special tagger runs on a regular time scale (every 4 hours). For flux determination one has to use during data analysis then the P_γ value derived by the tagger run corresponding to each package of data files. For the October 2008 beamtime (LH_2) this procedure was not performed, only one low intensity tagger run was recorded at the end of the beamtime. For the carbon beamtime in January 2009 this was done but later it was found out that the way how the beam intensity was reduced was not ensuring the same beam spot position as for the normal rate runs. However, this is mandatory to determine the correct photon detection efficiency since it depends on it! Therefore, the second method had to be applied: Here one determines the P_γ value directly from the data files with the

Beamtime	Number of photons	Photon energy range
LH_2 (October 2008)	$5.55 \cdot 10^{11}$	1250-3110 MeV
LH_2 (November 2008)	$7.35 \cdot 10^{11}$	1250-2350 MeV
Carbon (March 2007)	$\approx 1.0 \cdot 10^{12}$	1250-3110 MeV
Carbon (January 2009)	$1.66 \cdot 10^{12}$	1250-3110 MeV

Table 4.3: Overview of measured integrated photon fluxes for the different beamtimes used in the analysis.

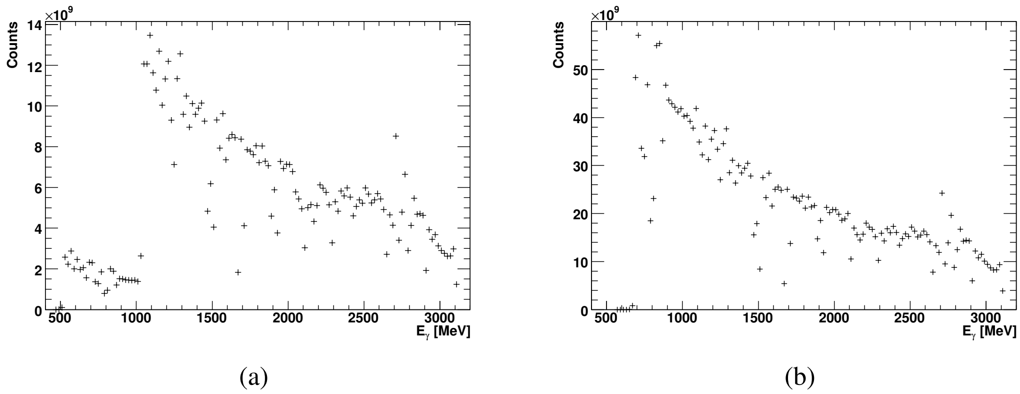

Figure 4.31: Integrated photon flux distributions for the (a) LH_2 (October 2008) and (b) carbon (January 2009) beamtime.

normal tagger rate using a correction factor of 1.1 to take the rate dependence of the GIM efficiency into account. This was done for the three beamtimes: LH_2 (October 2008, November 2008) and carbon (January 2009). For the carbon beamtime in March 2007 a flux determination was not possible. Here an estimate for the flux was given in [4] by using known cross sections for ω- and η-meson production to deduce the photon flux on the target by equation 4.16. Of course, this can only be a rough estimate and introduces a larger systematic uncertainty than the direct determination of the flux from the experimental data as described above.

The number of photons on the target for the data files used in the analysis (see chapter 3) were determined to amount to the values displayed in table 4.3. The photon flux distributions for two beamtimes are shown in figure 4.31. Their shape follows roughly the expected $1/E_\gamma$ behavior.

Chapter 5

Acceptance simulations

Using Monte Carlo simulations is a common method in hadron physics to model reaction kinematics and deriving the efficiency of a given detector setup for a certain physical reaction with respect to physical quantities like momentum, energy etc. or with respect to detector properties, e.g. electronic thresholds, coverage of the solid angle. In order to perform such kinematical as well as efficiency simulations the software GEANT3[1] (version 3.21/14) was used. In the first step an event generator allows the modeling of a certain physics reaction. The second step contains the propagation and interaction of charged and neutral particles through matter. In order to mimic the interaction between the resulting particles with the whole detector setup, one has to insert a detailed description of all detector parts into the simulation. Not only the active areas of a detector, which is meant to interact with certain particles to measure them, but also the passive material like holding structures, wrapping etc. must be considered. For this work all simulations were performed with the CBGEANT software, which contains all relevant details of the present CBELSA/TAPS experimental setup at Bonn (see chapter 2).

[1] **Ge**ometry **an**d **t**racking

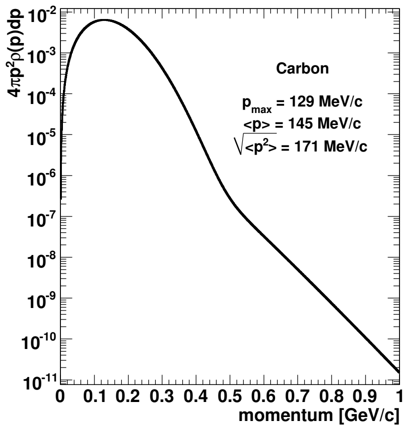

(a) Fermi momentum.

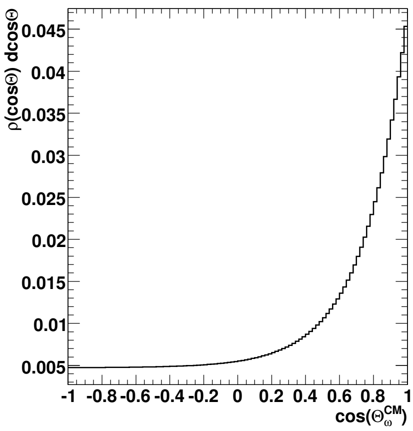

(b) ω-angular distribution.

Figure 5.1: Fermi momentum distribution and angular distribution used for the event generator.

5.1 Event generator

Since the experimental data for this work were taken on a liquid hydrogen target as well as on carbon, the event generator used in the GEANT simulation must contain for the carbon case the effect of Fermi-motion of nucleons inside the target nucleus. It is always assumed that the meson production takes place on one proton with momentum $\vec{p}_f$ within the nucleus (participant nucleon) while the other nucleons are not involved (spectator nucleons). For the calculation is it assumed that the participant nucleon has a momentum distribution as shown in 5.1(a), which is derived by [3]. The nucleon has a Fermi momentum P_F which is connected to the mean square momentum via:

$$P_F^2 = \frac{5}{3}\langle \vec{p}_f^{\,2} \rangle \tag{5.1}$$

For carbon a value P_F = 221 MeV/c is quoted [3].

Due to the presence of Fermi motion the available energy for producing a meson on a given nucleon is smeared out for a given incident photon energy. The total energy of a proton inside a carbon nucleus is:

$$E_p = m_{^{12}C}c^2 - \sqrt{(m_{^{12}C} - m_p)^2 c^4 + \vec{p}_f^{\,2} c^2} \tag{5.2}$$

To fulfill energy conservation, the mass of the proton is not anymore the free rest mass m_p, but:

$$m_p' = \sqrt{E_p^2 - \vec{p}_f^{\,2} c^2}/c^2 \tag{5.3}$$

The center-of-mass energy is the square-root of the Mandelstam variable s.

$$\begin{aligned} s &= (P_\gamma + P_{target})^2 && (5.4)\\ &= (E_\gamma + E_{target})^2 - (\vec{p}_\gamma + \vec{p}_{target})^2 c^2 && (5.5) \end{aligned}$$

with E_{target} = E_p, $\vec{p}_{target}$ = $\vec{p}_f$ and the relation E_γ^2 = $\vec{p}_\gamma^{\,2} c^2$ for massless particles the equation 5.5 yields:

$$\begin{aligned} s &= E_\gamma^2 + E_p^2 + 2E_\gamma E_p - \vec{p}_\gamma^{\,2} c^2 - \vec{p}_f^{\,2} c^2 - 2\vec{p}_\gamma \cdot \vec{p}_f c^2 && (5.6)\\ &= E_p^2 - \vec{p}_f^{\,2} c^2 + 2E_\gamma E_p - 2\vec{p}_\gamma \cdot \vec{p}_f c^2 && (5.7) \end{aligned}$$

This results with equation 5.3 in:

$$\sqrt{s} = \sqrt{m_p'^2 c^4 + 2E_\gamma \sqrt{\vec{p}_f^{\,2} c^2 + m_p'^2 c^4} - 2E_\gamma c \vec{p}_f \cdot \vec{e}_z} \tag{5.8}$$

The reaction can only happen if $\sqrt{s} > (m_p + m_\omega)c^2$. The nucleus is a bound system, thus energy is required to remove a nucleon. In first approximation this removal energy E_{rem} changes equation 5.2 to:

$$E_p = m_{^{12}C}c^2 - \sqrt{(m_{^{12}C}c^2 - m_p c^2 + E_{rem})^2 + \vec{p}_f^{\,2} c^2} \tag{5.9}$$

From nuclear experiments one knows that in reality the potential of the outgoing proton relative to the nucleus is momentum-dependent.
Another feature of the event generator is the possibility to include angular distributions for the produced mesons. Since in most cases the distribution in the center-of-mass frame is not flat in the angle Θ, it is important for any acceptance study to

describe this correctly. The input comes from various measurements on the free proton which is only an approximation for a nuclear target. In case of ω-photoproduction the distribution in figure 5.1(b) was used, which is based on [60].

Another experimental condition was the photon energy range from 1250 to 3100 MeV with the characteristical $1/E_\gamma$- distribution of the incident bremsstrahlung. In the event generator the produced ω-mesons decay always to $\pi^0\gamma$-pairs, whereas the π^0 decays to two photons. Proton and ω-meson are emitted back-to-back in the CM-frame, so there is always a correlation in Φ and Θ of these two particles. This correlation is kept for all the following calculations since the theoretical predictions show only visible effects for positive kinetic energies of the ω-meson (see chapter 1.3). For a bound meson-nucleus system however, this correlation is destroyed. In the analysis of the experimental data a forward going ($1^\circ < \Theta_p < 11^\circ$) proton is always required in coincidence with an ω (see section 4.4). This is the reason why already in the event generator only events with a forward going proton are kept.

The event generator delivers particles that form the start distribution. No detector effect like resolution or angular acceptance is considered. Figure 5.2 shows the influence of the Fermi motion and a finite energy resolution for a simulation with the nominal mass of the ω-meson of 782.65 MeV/c^2. The total energy minus the nominal mass of the free ω-meson is plotted for production on a free proton (blue), on a bound proton with Fermi motion (red) and in addition with a constant proton removal energy E_{rem} of +20 MeV (magenta). Since the proton is required in the angular range of the MiniTAPS detector, the ω-kinetic energy can only have certain values for the case of production off a free proton. Due to the smearing effect of the available energy, the curves with Fermi motion show a smooth distribution over a wider range. The effect of the removal energy has to be considered as negligible in our case because in the region of interest up to 200 MeV a difference to the red curve is not visible. For the interpretation of the data this fact will be important (see chapter 7) If the curves are folded with a Gaussian distribution with σ = 17 MeV width, the differences get less and entries below zero are produced. This shows the effect of an estimated detector resolution in the energy range of the ω-decay photons. The results of full simulations are shown in the next section.

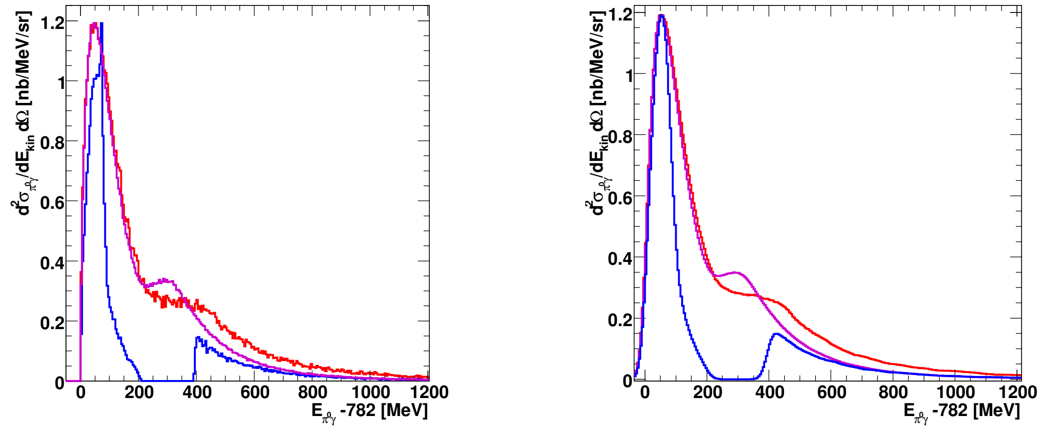

(a) Without energy resolution.

(b) With energy resolution of σ = 17 MeV.

Figure 5.2: $\pi^0\gamma$-kinetic energy start distribution for E_γ = 1250 - 3100 MeV. The kinetic energy of the ω-meson is plotted for production on a free proton (blue), on a bound proton with Fermi motion (red) and in addition with a constant proton removal energy E_{rem} of +20 MeV (magenta) for (a) without energy resolution and (b) with energy resolution of σ = 17 MeV. All curves are scaled to the maximum of the fit to the experimental cross section on carbon (see figures 7.1(a) and 7.3).

5.2 Full simulations

The main feature of the GEANT package is the implementation of all kind of interaction between particles and the detector material. This allows to deduce the detection efficiency of a certain reaction for a given detector setup. One has to distinguish between several efficiencies:

- **Detector acceptance**: This quantity can be deduced from the geometrical setup of the detector. The detector acceptance gives the probability for detecting a particle with certain properties (momentum, direction, type of particle, ...) in a given detector setup. For example an ω-meson potentially can be detected even if it goes towards an acceptance hole[2], because the emission angle of decay products of the meson (three photons) are independent of the direction of the meson[3].
- **Detector efficiency**: Some properties of the detector influence the detection efficiency. For example the finite CFD and LED thresholds cut off low energy hits. This implies that particles which decay into at least one low energy particle cannot be reconstructed.
- **Analysis efficiency**: During the analysis of the data, it is necessary to set certain cuts which not only reduce the background channels, but also reduce the signal to some extent. When these cuts are used they always have to be set in such a way that the cuts should reduce the largest amount of background events while keeping the signal untouched as much as possible.

Since detector geometry, properties of the detector materials and physical processes are included in the simulation package, the same behavior is expected in the simulation as in the real data. The detection efficiency of the ω-meson via three photons in coincidence with a proton ($\epsilon_{\omega,p}$) is given by the ratio of the reconstructed events and

[2]Acceptance hole usually is a direction where no detector is placed. A particle going toward this direction will be lost.

[3]This statement is true in the center-of-mass system if the decay is defined by phase-space only. If the reference frame is not the CM or the decay is not a phase-space decay, the direction of the decay products are not absolutely independent of the direction of the meson.

the generated events.

$$\epsilon_{\omega,\mathrm{p}} = \frac{N^{\mathrm{reconstructed}}_{\omega,\mathrm{p}}}{N^{\mathrm{generated}}_{\omega,\mathrm{p}}} \tag{5.10}$$

The efficiency generally depends on several kinematical values (momentum of the meson, beam energy, ejection angles of the knocked-out proton, etc.).
In a first step GEANT simulations were performed, to understand the kinematical constraints of the production. A calculation for the incident photon energy range 1150 - 3100 MeV with an $1/E_\gamma$ distribution on carbon was performed; the ω-meson has its nominal mass. In figure 5.3 one can see the correlation between the incident photon energy and the kinetic energy of the produced ω-mesons for a forward going proton in MiniTAPS with no further cuts applied. The two branches corresponding to forward and backward going mesons in the CM-system are clearly visible. In order to avoid distortions by the high energetic branch for the kinetic energy distribution, a cut on the beam energy of E_γ > 1250 MeV has been applied. Since the beam energy range is rather wide, one has to check if the data need an acceptance correction which is beam energy dependent. For that reason, full GEANT3 simulations were performed for beam energy intervals of 200 MeV. The experimental data are available after background subtraction in a two-dimensional plane (see section 7.1). In order to have an accurate cross section determination, the acceptance correction is performed in the same plane (kinetic energy of the $\pi^0\gamma$-pair vs. invariant mass of the $\pi^0\gamma$-pair). Therefore the simulated $\pi^0\gamma$-pairs have invariant masses between 400 and 1200 MeV/c^2.
The GEANT output is stored in the same format (list-mode data) as the measured data and can be processed by the same analysis code. Nevertheless, in the simulated one it is exactly known which reactions are involved. The same software (EXPLORA framework) is used and the same cuts are applied (for details see section 4.4). Even a cut on the time-of-flight of the proton is possible, since from the start distribution the total energy is known which can be used to determine this quantity. In figure 5.4 the spectra for the deposited energy in the MiniTAPS crystals vs. the time-of-flight is shown for the reconstructed distributions.

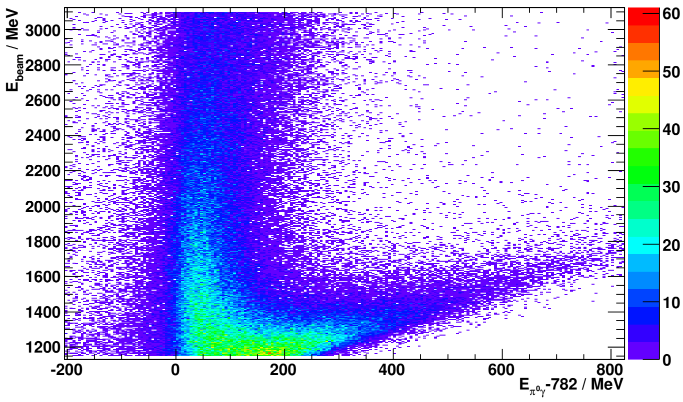

Figure 5.3: Correlation between kinetic energy and beam energy for ω-mesons for recoil protons in MiniTAPS ($1° < \Theta_p < 11°$). The plot shows two different branches of the produced mesons: One where the mesons go forward and one where they go backward in the CM-system. By applying a cut on the beam energy one can separate the two branches in the projection on the kinetic energy. To determine the peak position of this distribution only the branch with the low energy mesons should be taken.

The figures 5.5(a), 5.6(a) and 5.7(a) show the start and the figures 5.5(b), 5.6(b) and 5.7(b) the reconstructed distribution for three energy bins on a carbon target with Fermi motion. The resulting acceptances are shown in figures 5.5(c), 5.6(c) and 5.7(c). Differences are small, especially in the invariant mass region around 782 MeV/c^2. The acceptance gradually drops from about 40%, over 25% to 15% in average in the highest bin. In addition, within the momentum range of interest (0 - 900 MeV/c) indicated by the black lines, there is a large area of acceptance in the two-dimensional plane for every beam energy bin.

Finally, figure 5.8 shows the distribution for the full energy range on a carbon target. In comparison the spectra for a free proton is shown in figure 5.9. To avoid distortions from bins with low statistics, large relative statistical uncertainties or very small or unphysical values, only bins with an acceptance of 0.04 < ϵ <1.0 and a relative statistical error less than 10% in the hydrogen case and less than 3.5% in the carbon case are taken into account.

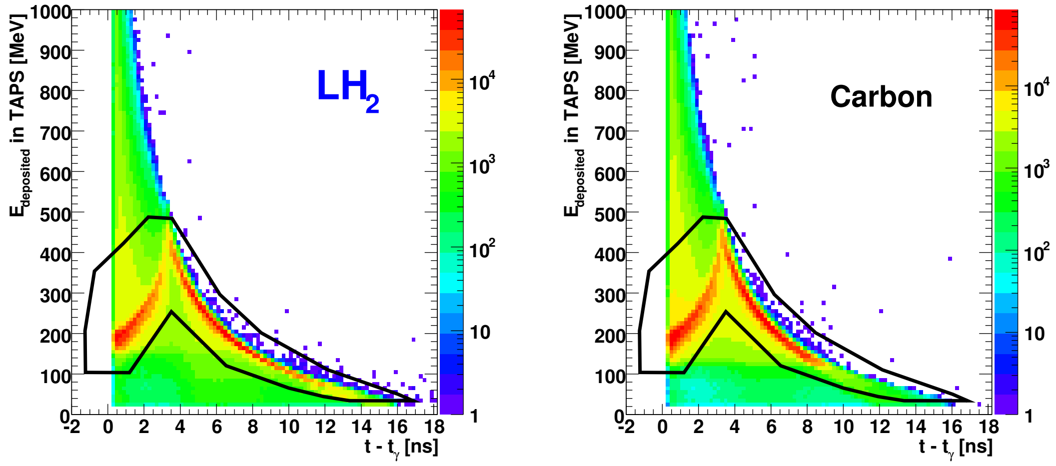

(a) (b)

Figure 5.4: Reconstructed distribution: Energy deposited in the MiniTAPS detectors as a function of the time-of-flight. The proton band cut is indicated for a simulation on (a) free proton and (b) carbon target. No time resolution has been folded in.

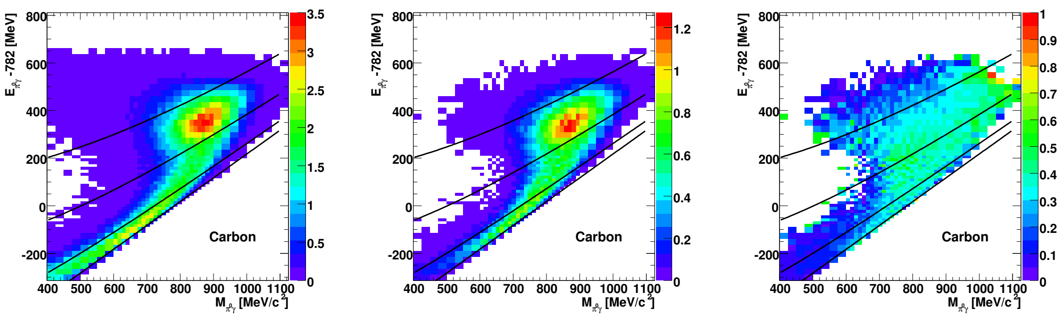

(a) Start distribution. (b) Reconstructed distribution. (c) Acceptance.

Figure 5.5: $\pi^0\gamma$-simulation for E_γ = 1250 - 1450 MeV on carbon.

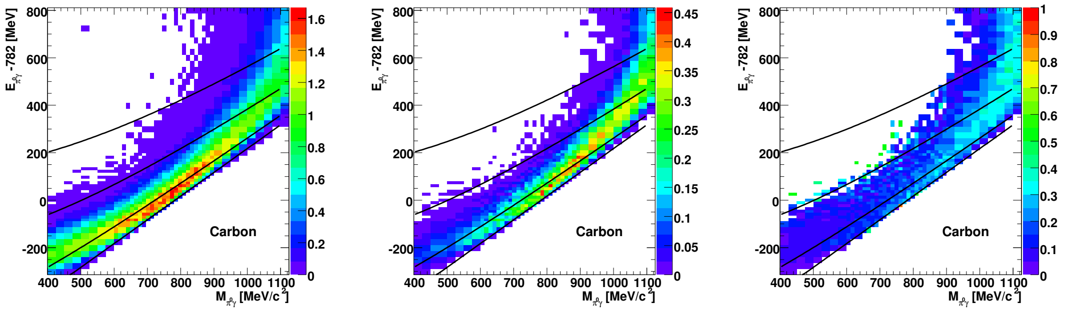

(a) Start distribution. (b) Reconstructed distribution. (c) Acceptance.

Figure 5.6: $\pi^0\gamma$-simulation for E_γ = 2050 - 2250 MeV on carbon.

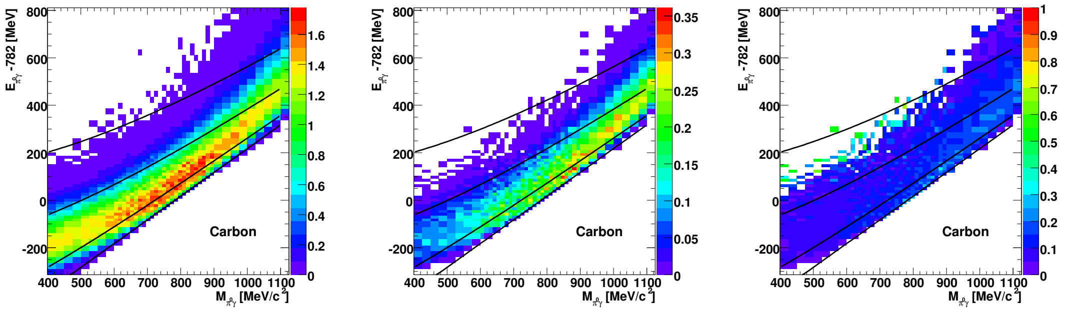

(a) Start distribution. (b) Reconstructed distribution. (c) Acceptance.

Figure 5.7: $\pi^0\gamma$-simulation for E_γ = 2850 - 3100 MeV on carbon.

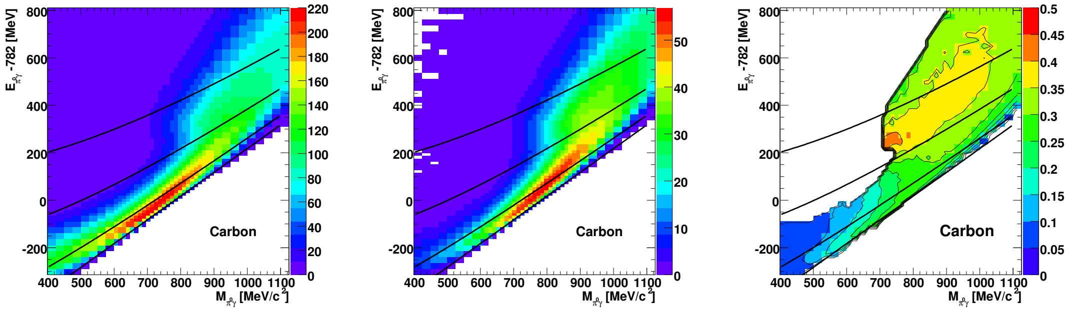

(a) Start distribution. (b) Reconstructed distribution. (c) Acceptance.

Figure 5.8: $\pi^0\gamma$-simulation for E_γ = 1250 - 3100 MeV on carbon.

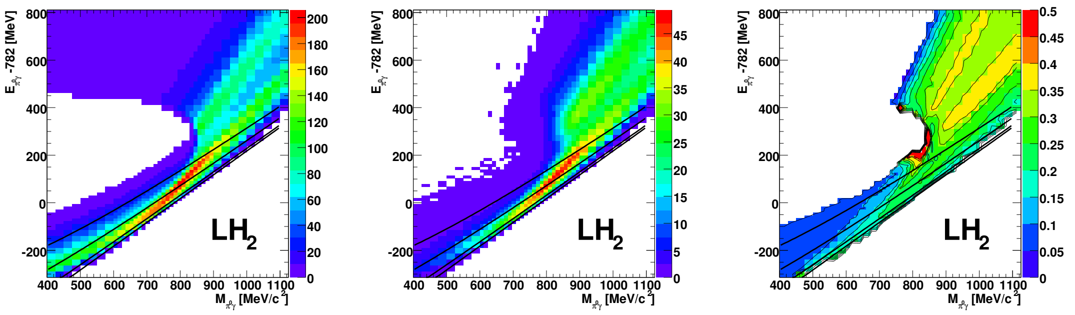

(a) Start distribution. (b) Reconstructed distribution. (c) Acceptance.

Figure 5.9: $\pi^0\gamma$-simulation for E_γ = 1250 - 3100 MeV on a free proton.

With an acceptance determined carefully under the same constraints like for the experimental data, especially applying the same trigger conditions and implementing the extended target materials with the correct dimensions, it is possible to obtain a cross section.

Chapter 6

GiBUU transport calculations

This chapter describes the use of the Giessen Boltzmann-Uehling-Uhlenbeck transport model (GiBUU) to predict experimental observables for ω-photoproduction in general and changes of these in the presence of in-medium modifications of the ω-meson in particular.

The tool for these numerical simulations of nuclear reactions is the hadronic transport model GiBUU (for further details see [61], [62], [63] and [64]) which provides a unified framework for various types of elementary reactions on nuclei in a broad energy range. This model takes care of the correct transport-theoretical description of the hadronic degrees of freedom in nuclear reactions, including propagation, collisions and the decay of particles in the energy regime of MeV to GeV. As it is a hadronic model, the basic degrees of freedom are baryons and mesons. The model currently includes 61 baryons and 22 mesons in total. It is based on a set of semi-classical kinetic equations, which describe the dynamics of a hadronic system explicitly in phase space and time.

The general Boltzmann-Uehling-Uhlenbeck (BUU) equation, representing the basis of the transport model, is given by:

$$[p_0 - H, g^<] + [Re(g), \Sigma^<] = \Sigma^< g^> - \Sigma^> g^< \tag{6.1}$$

$$I_{Vlasov} + I_{off-shell} = I_{collision} \tag{6.2}$$

Here $g^<$ denotes the Wigner transform of the real-time Green's function, g is the retarded Green's function and $g^>$ represents the density of hole states in phase space. H

is the one-particle Hamiltonian, $\Sigma^<$ and $\Sigma^>$ are self energies (gain and loss term). For details see [65] and [66]. A full derivation can be found in [67]. The square brackets denote the Poisson brackets. The BUU equation consists of three parts: The collision term $I_{collision}$ on the right hand side which governs the decays and collisions of particles. It includes a gain term which corresponds to the creation of particles and the loss term which corresponds to particle destruction. The first Poisson bracket on the left hand side (I_{Vlasov}) is the most basic part of the equation ("Vlasov term"). In the absence of the other terms, it describes the propagation of stable non-interacting particles through a mean field. The second Poisson bracket is the off-shell term $I_{off-shell}$ because it contains the off-shell dynamics of broad resonances or vector mesons inside the nuclear medium.

The model can be used to investigate the sensitivity of experiments for measuring the impact of in-medium modifications on the ω-meson. All these effects depend on the nuclear density. Detailed studies of the density decay profile and momentum distributions can enlighten the possible measurable effects in an experiment. Although it cannot describe the population of quantum-mechanical (bound) states, GiBUU can be used to calculate effective branching ratios of these states (see section 1.4) into the final state which is required in the analysis of the experimental data. In that way it links theoretical predictions of quantum-mechanical ω-mesic bound states to experimental observables.

As input parameters a whole set of production cross sections, decay widths, inelastic cross sections, vacuum masses etc. are included in the GiBUU simulation framework.

6.1 Access to in-medium decays of ω-mesons

A first investigation of the density profile of the produced ω-mesons was performed using the GiBUU code. For these simulations the real branching ratio of the ω-meson into $\pi^0\gamma$ as well as the decay of the neutral pions into two photons are considered. A collisional broadening of $\Gamma(\rho_0)$ = 150 MeV is assumed and thus off-shell transport allowed. The in-medium width is assumed to be independent of the ω-momentum,

as found experimentally in [12]. In [12] no significant momentum dependence of the in-medium width was observed; but the average ω-momentum was 1.1 GeV/c. This has to be considered in the comparison to experimental data for low momentum mesons. In figure 6.1(a) one finds the density spectrum of photoproduced ω-mesons on a ^{12}C nucleus for the incoming photon energies of 1250 - 3050 MeV with an $1/E_\gamma$ distribution. The black curve shows the densities at the production points. Here one sees that ω-mesons are produced over the whole volume of the nucleus. The average density is about $0.5\rho_0$. These mesons do propagate and have the possibility of being absorbed by collisions with nucleons (inelastic reactions) or they can decay either inside or outside of the nucleus. The blue line shows the densities for the decay points into $\pi^0\gamma$. The fraction which decays outside of the nucleus (ρ = 0) is clearly visible. Apparently only a small fraction of ω-mesons probes the nucleus. Here the effect of the strong in-medium collisional broadening of the ω-meson is visible: The free width of 8.4 MeV has to be compared to 150 MeV for full nuclear matter density. After finishing the propagation with 200 time steps with 0.1 fm/c, all ω-mesons are forced to decay as well as all neutral pions.
From this final state (three photons and a nucleon) not all events can be reconstructed in an experiment. Hence, a cut on the reconstructed $\pi^0\gamma$-invariant mass of 700 - 850 MeV/c^2 was applied. Because of the high background (see section 4.4), ω-mesons with lower masses cannot be identified. Due to the neutral pion final state interaction, the number of reconstructed ω-mesons is further reduced (see figure 6.1(a) red line). Since the probability for an absorption or scattering of the decay pion depends on the density, the events for higher densities are suppressed. The average density at the decay points is already down to $0.19\rho_0$. A final restriction that a forward going proton is required ($1^\circ < \Theta_p < 11^\circ$) does not affect the probed densities, but only the intensity (green line). In figure 6.1(b) one sees the corresponding spectra for ω-photoproduction on a ^{93}Nb nucleus for an incoming photon energy range of 900 -1300 MeV with an $1/E_\gamma$ distribution. Because this nucleus is larger, the production yield within the nucleus is higher, resulting in an average density for production of $0.73\rho_0$ (black line). The same holds true for the decay points (blue line) with an average density of $0.54\rho_0$. Requiring the reconstruction of an ω-meson has a stronger impact than in the carbon case and the average density which is probed is only $0.25\rho_0$ (red line), comparable to the carbon case. The simulations on a niobium nucleus were

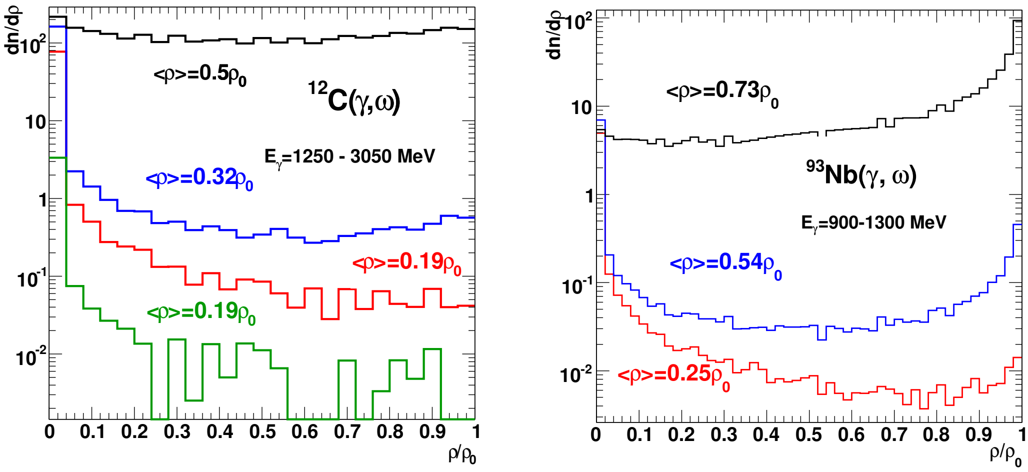

(a) (b)

Figure 6.1: GiBUU simulations: Nuclear density distributions for ω-photoproduction on (a) carbon and (b) niobium nucleus.
Black: produced mesons, blue: decays into $\pi^0\gamma$, red: reconstructed mesons from three photons within 700 < $m_{\pi^0\gamma}$ < 850 MeV, green: an additional forward going proton is required ($1^\circ < \Theta_p < 11^\circ$).

performed for a photoproduction experiment at the accelerator MAMI in Mainz (see [68]).

It has to be stressed that in the experiment ω-mesons are produced at high nuclear matter densities, but only a small fraction of them can be reconstructed. This important information leads to the question what measures have to be taken in the analysis to enhance the number of mesons which decay at a point of reasonable density.

Figure 6.2 shows the sensitivity of the distributions for reconstructed ω-mesons on a momentum cut. In black the spectrum for all momenta is shown and in red the spectrum for ω-momenta lower than 500 MeV/c. Clearly the fraction of decays at higher densities is enhanced since the selected slow mesons cannot leave the nucleus before their decay. In figure 6.3 the fraction of ω-mesons which decay inside the nucleus is shown as a function of their momentum. Thus, a strict cut on the momentum of the reconstructed meson improves the possibility to probe in-medium effects and thus enables measuring in-medium modifications of experimental observables.

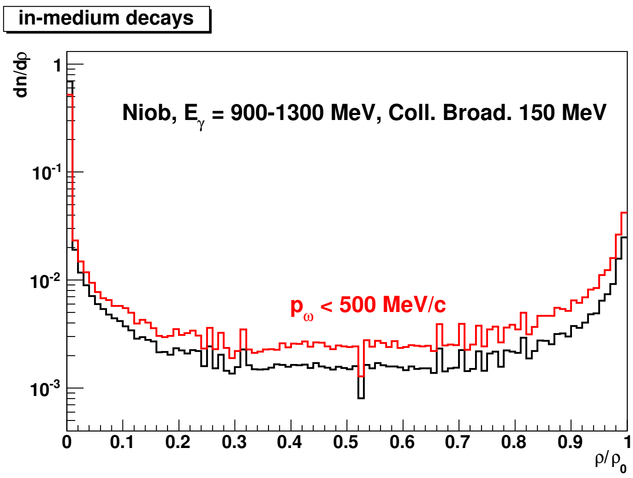

Figure 6.2: Nuclear density distribution for decaying ω-mesons for all momenta (black) and momenta p_ω < 500 MeV/c (red). This condition reduces the total ω-yield by 25%, but enhances the average density at the decay point.

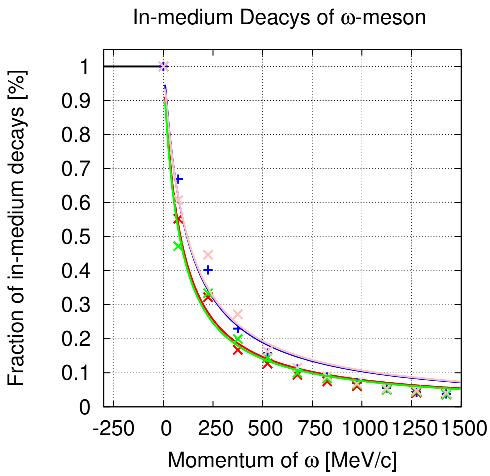

Figure 6.3: In-medium fraction of ω-meson decays as a function of momentum for calculations on carbon for the incident photon energies of 1250 - 3100 MeV. In red and blue the scenario with collisional broadening only ($\Gamma(\rho_0)$ = 150 MeV), in green and pink with additional mass shift ($V_0(\rho_0)$=-125 MeV) are displayed. Blue and pink show the fraction of in-medium decays ($\rho > 0.1\ \rho_0$), red and green the fraction after reconstruction.

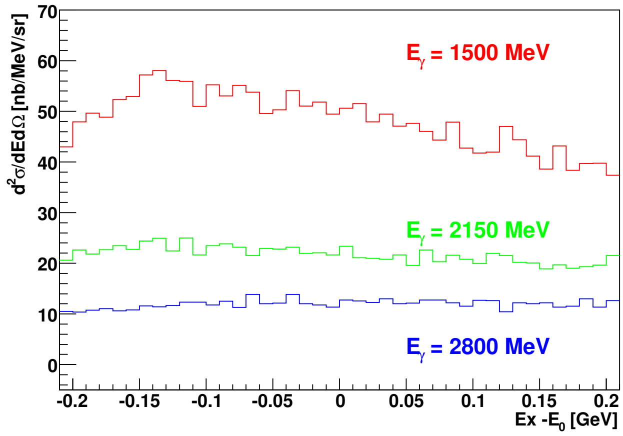

Figure 6.4: Double differential cross section for a forward going proton assuming photoproduction of an η'-meson. Three different incoming photon energies are plotted.

6.2 Background determination

With the GiBUU simulation framework one can determine the cross section of a reaction under various circumstances, but also determine the contributing background cross sections for a certain reaction. To investigate the background for photoproduction of η'-mesons a GiBUU simulation was performed with all possible initial states switched on. All kind of mesons and resonances could be produced or excited. The η'-meson itself is not included in the simulation code. A planned experiment at the electron accelerator ELSA in Bonn at the BGO-OD setup (for details see [69]) aims at an inclusive measurement of η'-mesons by determining the momentum of the forward going proton on which the meson was produced. With a high resolution magnetic spectrometer ("open dipole") the momentum of the proton can be measured and figure 6.4 shows the double differential cross section of a forward going proton for all background channels for three different incoming photon energies as a function of the excitation energy of the residual nucleus subtracting the invariant mass of a free η'-meson of 958 MeV/c^2. From that knowledge and a known η'-production cross section one can deduce the necessary statistics and thus the required beam time for a certain significance of the η'-signal.

6.3 Simulation of bound states

The main focus on the GiBUU calculations was to link the quantum-mechanical calculations to the experimental observables. Simulations were performed for two in-medium modification scenario of the ω-meson: A scenario with collisional broadening of $\Gamma(\rho_0)$ = 150 MeV and a scenario with the same broadening and an attractive potential of $V_0(\rho_0)$= - 125 MeV (attractive mass shift of $\frac{\Delta m}{m_0}$ = -0.16). Since in the analysis of the experimental data (see section 4.4) a forward going proton is requested, the same was applied here. It is always requested that together with the ω-meson (reconstructed or not) exactly one proton goes to the angular range covered by the MiniTAPS detector while there is no other proton elsewhere. This proton must have a kinetic energy larger than 100 MeV, since during the beamtimes the thresholds were approximately that high on average in MiniTAPS (see chapter 3).
In the first step the production cross section for ω-photoproduction is checked under the conditions described above. For this purpose, a calculation without any propagation nor final state interaction (FSI) of the ω-meson is performed. In both calculations the final state interaction of the participant proton is taken into account. The resulting distribution for the double differential cross section as function of the kinetic energy is shown in figure 6.5. It is plotted together with the theoretical predictions by Nagahiro et al. (see section 1.4) for the formation of ω-bound states. Both calculation roughly agree in yield and shape of the distributions.

Because these quantum-mechanical calculations do neither contain the decay of the populated (bound) state nor final state interaction of the decay products, they have to be multiplied with a kinetic energy dependent factor representing an effective branching ratio for the populated state to undergo a decay into $\pi^0\gamma$ and to be identified as such. The denominator of this branching ratio is the distribution of all mesons at the time of their destruction; either by absorption, i.e. inelastic collisions within the nucleus or by normal decay. Both distributions are available in the GiBUU code. Figure 6.6(a) shows the kinetic energy spectra of ω-mesons at the time of absorption; note that it is not the distribution at a given time step. Figure 6.6(b) shows the distributions of the decaying mesons into any final state. For both cases, the forward going proton undergoes final state interaction and the ω-mesons are not reconstructed. The

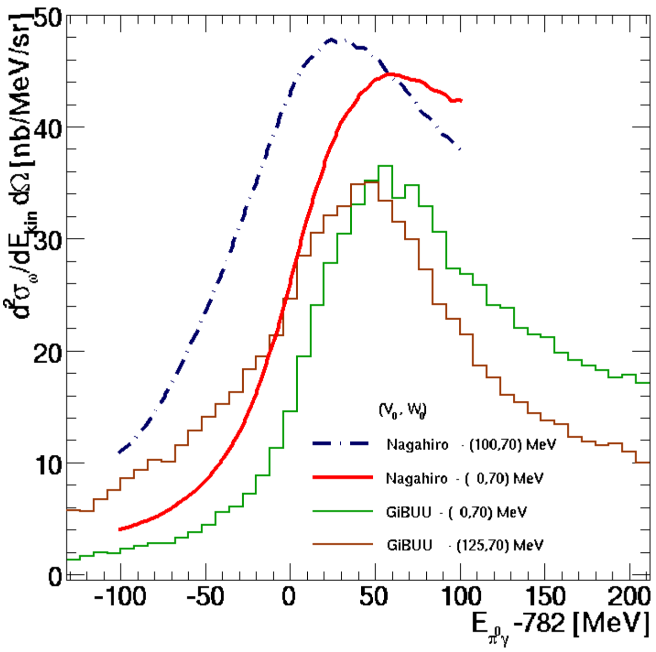

Figure 6.5: Double differential formation cross section (histograms) of ω-photoproduction in coincidence with a forward going proton in Mini-TAPS ($1^\circ < \Theta_p < 11^\circ$) for two different in-medium scenarios, using GiBUU: Collisional broadening only $\Gamma(\rho_0)$ = 150 MeV (green) and in addition an attractive potential of $V_0(\rho_0)$ = -125 MeV (brown). For comparison the quantum-mechanical calculations by Nagahiro et al. (see section 1.4) are shown (lines).

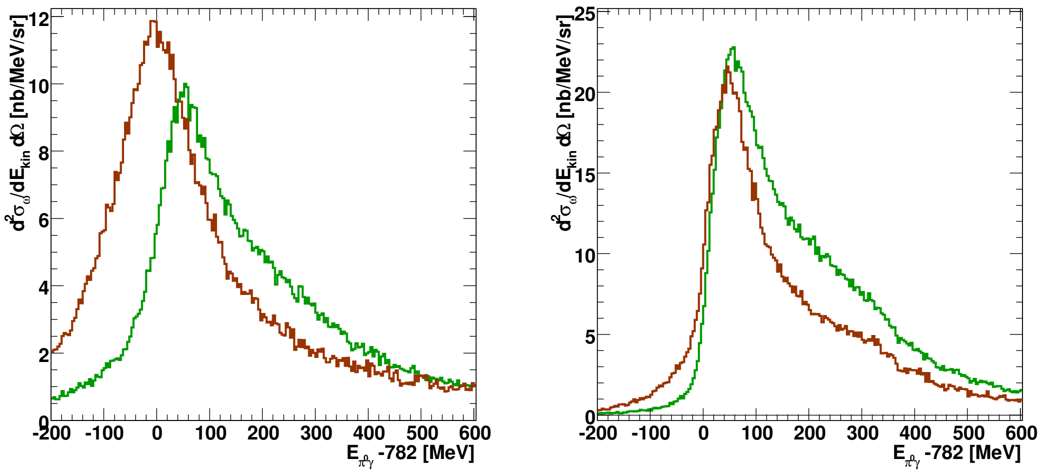

(a) (b)

Figure 6.6: Energy spectra of ω-mesons in coincidence with a forward going proton (with proton FSI) for two different in-medium scenarios: Collisional broadening only (green) and in addition an attractive potential of -125 MeV (brown). (a): Energy spectrum of ω-mesons at the time of absorption. (b): Energy spectrum of ω-mesons at the time of decay.

information is taken directly from the four-vector of the meson.

For calculating the effective branching ratio both plots have to be added. This is shown in figure 6.7(a). The numerator is just the distribution of ω-mesons after final state interaction of the decaying fraction into $\pi^0\gamma$. Here the meson has to be reconstructed from exactly three photons as described above. From these three photons the ω is reconstructed by requiring that at least one two-photon combination has the invariant mass of $110 < m_{\gamma\gamma} < 160$ MeV/c^2 and that the $\pi^0\gamma$-invariant mass fulfills $700 < m_{\pi^0\gamma} < 850$ MeV/c^2. The free branching ratio for a decay into $\pi^0\gamma$ is included here. Again, the coincident proton undergoes a possible final state interaction.

The figure 6.8 shows the effective branching ratio as a function of the kinetic energy. Since it is used as a correction factor for the theoretical calculations, an average for both scenarios is taken (blue line) in order to avoid biasing the result. One clearly sees that the branching ratio changes fast at zero kinetic energy which is the limit between bound and quasi-free production. For higher energies the ratio tends towards the free

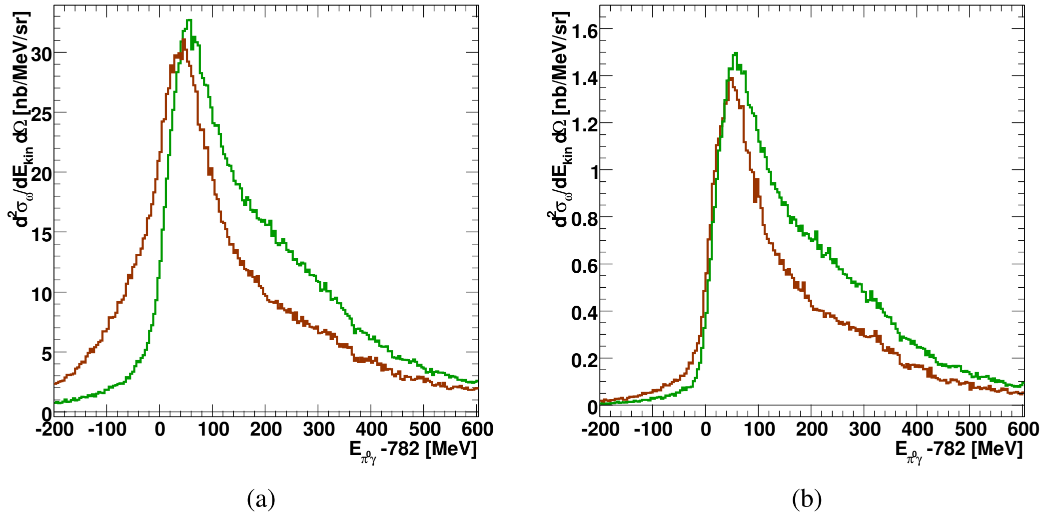

Figure 6.7: Spectra of ω-mesons in coincidence with a forward going proton (with proton FSI) for two different in-medium scenarios: Collisional broadening only (green) and in addition an attractive potential of -125 MeV (brown). (a): Spectrum of the sum of figures 6.6(a) (absorption) and 6.6(b) (decay) (denominator). (b): Spectrum after FSI of all particles and reconstruction of $\pi^0\gamma$-pairs (numerator).

branching ratio of 0.083.
But can the numerical value for negative energies be understood? A rough estimate gives the answer to that. The total width Γ_{tot} is the sum of the free and the in-medium width. The branching ratio is defined by :

$$BR = \frac{\Gamma_{free}}{\Gamma_{tot}(\rho)} = \frac{8.4\ \mathrm{MeV} \cdot 0.083}{\Gamma_{med}(\rho) + 8.4\ \mathrm{MeV}} \tag{6.3}$$

Since the in-medium width is only 150 MeV for normal nuclear matter density, one has to assume an average density at which the decay of the bound states happens. As described in section 6.1 we assume a value of $0.6\rho_0$. With that equation 6.3 yields:

$$BR = \frac{8.4\ \mathrm{MeV} \cdot 0.083}{\Gamma_{med}(\rho) + 8.4\ \mathrm{MeV}} = \frac{8.4\ \mathrm{MeV} \cdot 0.083}{90\ \mathrm{MeV} + 8.4\ \mathrm{MeV}} = 7.1 \cdot 10^{-3} \tag{6.4}$$

This is close to the value for negative energies a obtained by the GiBUU simulation. For a small positive kinetic energy, we perform the same estimate. Here, we have to take the momentum dependence of the in-medium width into account, as it is implemented in the GiBUU code (see figure 1.10). For a kinetic energy of 50 MeV, which corresponds to a momentum of 284 MeV/c, the in-medium width for normal nuclear matter density is 80 MeV. Assuming an average density for the decays of $0.1\rho_0$ (see figure 6.3), equation 6.3 yields:

$$BR = \frac{8.4\ \mathrm{MeV} \cdot 0.083}{\Gamma_{med}(\rho, p) + 8.4\ \mathrm{MeV}} = \frac{8.4\ \mathrm{MeV} \cdot 0.083}{80\ \mathrm{MeV} \cdot 0.1 + 8.4\ \mathrm{MeV}} = 0.043 \tag{6.5}$$

This is again consistent with the value derived by GiBUU simulations (see figure 6.8). For high energies Γ_{med} tends to zero and the branching ratio approaches the free value.

In figure 6.9 the energy distribution for the reconstructed ω-mesons is shown. Since it contains all final state effects, the reconstruction of the meson and the resriction on the angular range of the proton, it can be directly compared to the experimental data (see section 7.1).

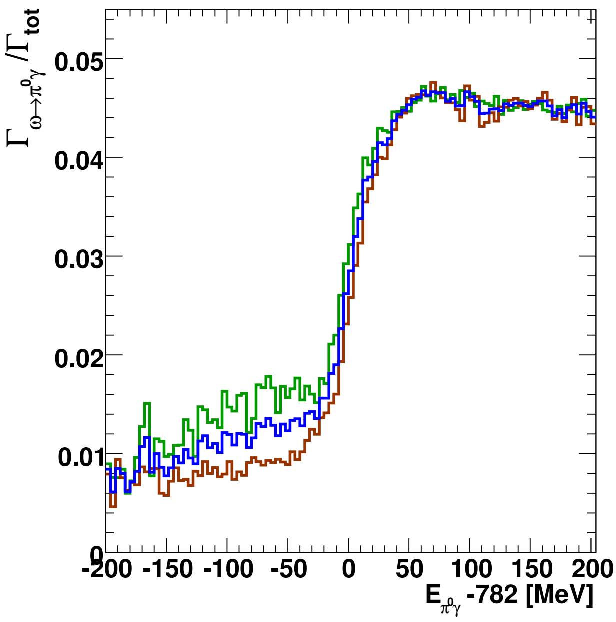

Figure 6.8: Effective branching ratio as function of the ω-kinetic energy for two different in-medium scenarios. Green: Collisional Broadening only, brown: additional attractive potential of -125 MeV, blue: average of both spectra. The green and brown curves are the ratio of the two spectra 6.7(b) and 6.7(a).

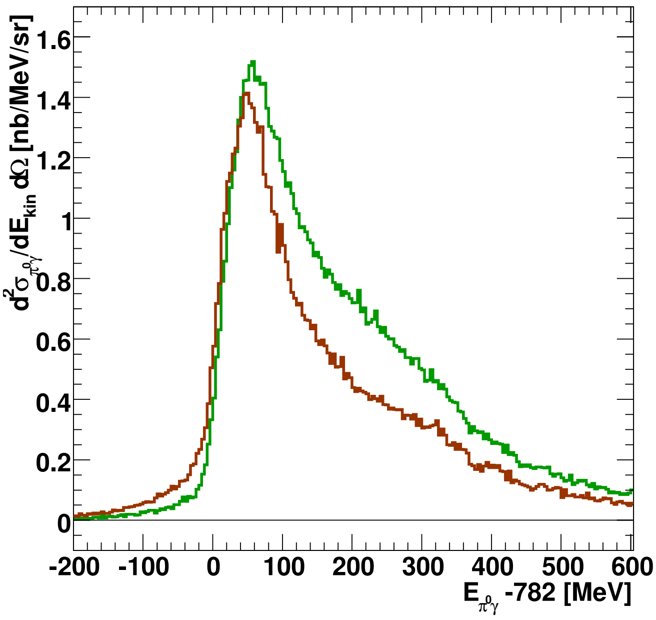

Figure 6.9: Spectra of ω-mesons in coincidence with a forward going proton with kinetic energy larger than 100 MeV after FSI of all particles for two different in-medium scenarios: Collisional broadening only (green) and in addition an attractive potential of -125 MeV (brown).

Chapter 7

Results and discussion

7.1 Results

With the information of the previous chapters, it is possible to determine an absolute cross section. The resulting two-dimensional plane of counts (see figure 4.27) is acceptance corrected bin by bin with the detection efficiencies calculated in section 5.2 (see figures 5.8 and 5.9). Dividing the result by the calculated photon flux (see section 4.5), the target density (see section 2.5) and the solid angle of the MiniTAPS detector one yields a double differential cross section according to the formula

$$\frac{d^2\sigma}{dEd\Omega} = \frac{d^2N_{event}}{dEd\Omega} \cdot \frac{1}{\epsilon \cdot n_{target} \cdot N_\gamma \cdot BR} \tag{7.1}$$

The results are shown in figures 7.1 and 7.2.

A direct comparison of the cross section measured on carbon and hydrogen is shown in figure 7.3. In addition, the result of a Monte Carlo simulation, requesting a proton in the polar angular range $1^\circ < \Theta_p < 11^\circ$, is shown (compare to figures 5.2(b)). One can see immediately that both experimental distribution peak almost at the same energy. A fit with a Novosibirsk function (see equation 4.9 [54, 55]) yields for the peak position of the distributions in the carbon case (60.5 $\pm$ 7) MeV and for the hydrogen target (60 $\pm$ 3) MeV. This value corresponds to a momentum of about 300 MeV/c which is almost as low as momenta of bound nucleons within the nucleus.

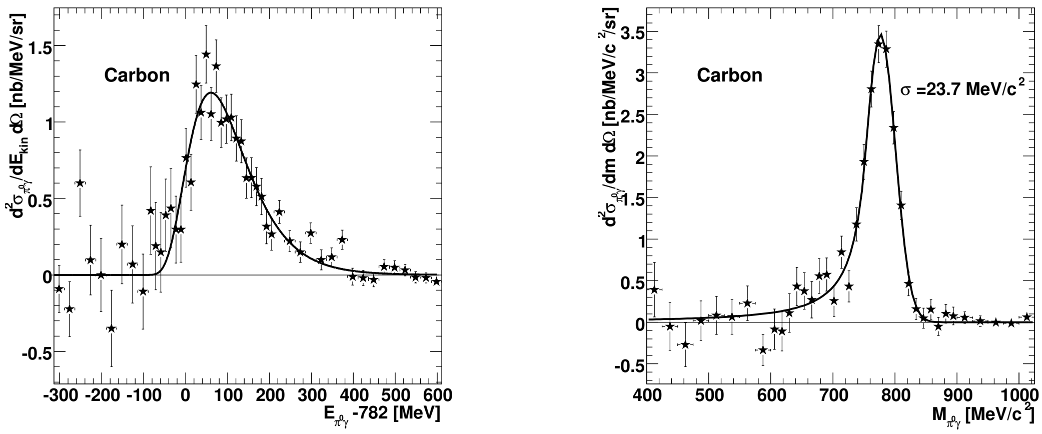

(a) Kinetic energy distribution. (b) $\pi^0\gamma$-invariant mass.

Figure 7.1: Double differential cross section for the photoproduction of ω-mesons off carbon in coincidence with a proton within $1^\circ < \Theta_p < 11^\circ$ (a) as a function of the total energy of the $\pi^0\gamma$-pair minus 782 MeV and (b) as a function of the $\pi^0\gamma$-invariant mass, fitted with the Crystal Ball function [59]. The width is σ_{carbon} = 23.7 MeV/c^2.

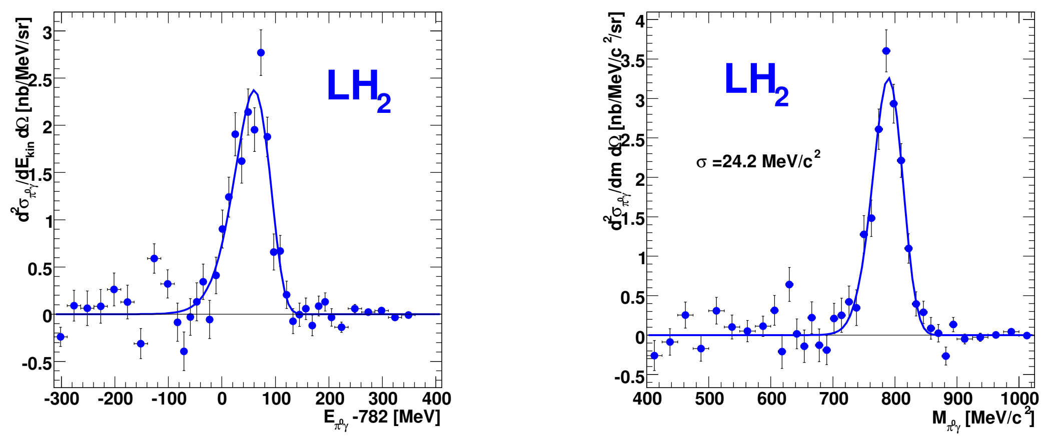

(a) Kinetic energy distribution. (b) $\pi^0\gamma$-invariant mass.

Figure 7.2: Double differential cross section for the photoproduction of ω-mesons off the free proton in coincidence with a proton within $1^\circ < \Theta_p < 11^\circ$ (a) as a function of the total energy of the $\pi^0\gamma$-pair minus 782 MeV and (b) as a function of the $\pi^0\gamma$-invariant mass, fitted with the Novosibirsk function [54, 55]. The width is σ_{LH_2} = 24.2 MeV/c^2.

As discussed in sections 1.4.2 and 6.3, a detailed comparison of the experimental cross sections to dedicated theoretical calculations can only be done after taking into account the effective branching ratio for $\omega \rightarrow \pi^0\gamma$, including final state interaction. Starting from the distributions in figure 7.4(a), which are derived in section 1.4.2, multiplication with the effective branching ratio in figure 7.4(b), determined in section 6.3, yields the cross sections in 7.4(c). The calculated distributions show a clear sensitivity of the peak position in the total energy distribution to the real part of the optical potential. By plotting the peak position against the potential depth, one obtains the blue points in figure 7.4(d). A parabola fit describes the dependence quite well (blue curve). With the experimental determined peak position of the carbon data one can now derive the potential depth using this correlation. The statistical uncertainty of the fit results directly translates into the statictical error of the potential depth (red lines and red dashed area): the result is $V_0(\rho = \rho_0)$= (-15 $\pm$ 35) MeV. The real part of the ω-nucleus optical potential is only small and the ω-nucleus potential is - if at all - weakly attractive. Since this result indicates a small real part compared to the large imaginary part of W_0=150 MeV of the optical potential, the ω-meson is not suited to observe bound states in contrast to the negative pions (see section 1.3) and η'-mesons which appear to be better suited to measure bound states [70, 71].

A direct comparison of the data to the modified calculations is shown in figure 7.5. Due to the large errors of the data points, one cannot determine which scenario fits the data best, since each absolute yield for negative energies agrees with the data points. The absolute height of the predictions agrees, within the model uncertainties [22], with the data. Figure 7.6 shows the carbon data compared to GiBUU simulations for two in-medium scenarios. On the positive side the data agree better with the scenario of an attractive potential of V_0 = -125 MeV. For the negative energies none of the curves can describe the observed yield adequately.

The average cross section in the bound state region of -100 to 0 MeV is measured to (0.3 $\pm$ 0.1) nb/MeV/sr, corresponding to a formation cross section of (22 $\pm$ 7) nb/MeV/sr obtained by correcting for the effective $\omega \rightarrow \pi^0\gamma$ branching ratio. This yield may be produced by the large in-medium width of the ω-meson. The predicted production cross section by Marco and Weise (see section 1.4.1) in the negative energy range is about 3 nb/MeV/sr in average. Corrected by the branching ratio, a value

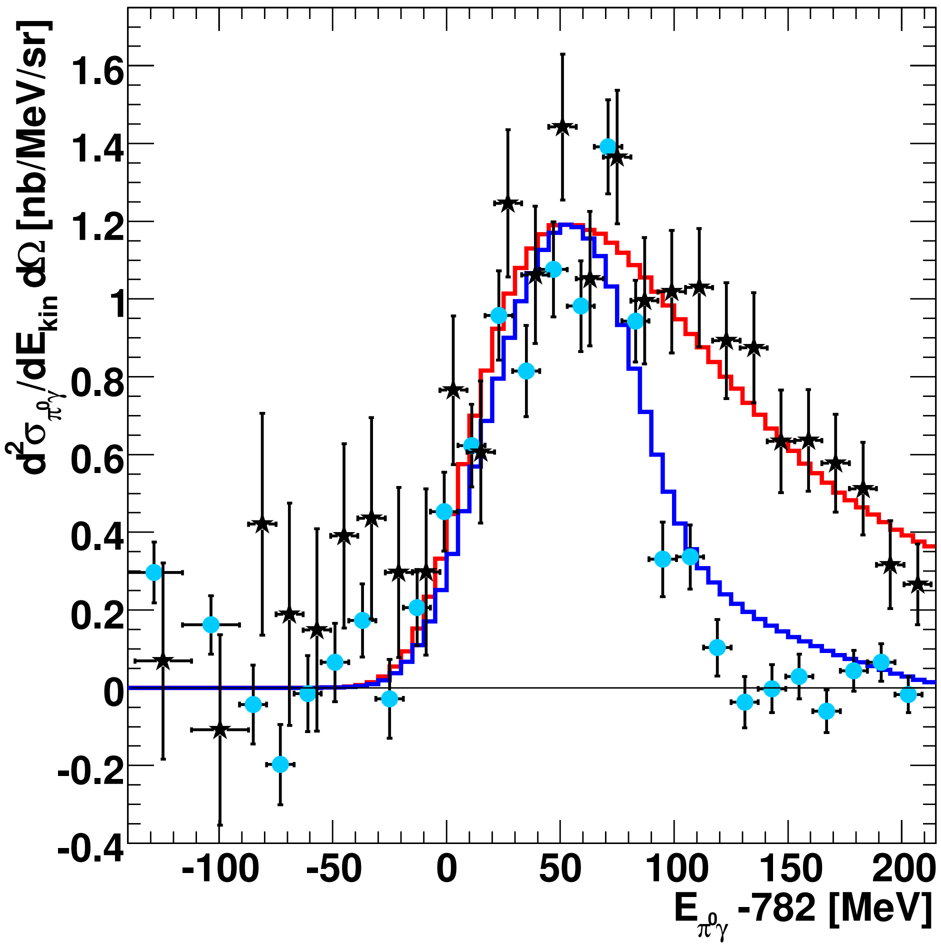

Figure 7.3: Comparison of the experimental double differential cross section (light blue points: LH_2 data, black stars: carbon data) to Monte Carlo calculations (blue histogram: LH_2 target, red histogram: carbon target with Fermi motion). The histograms and the blue data points are scaled to the maximum of the fit to the carbon data (see figure 7.1(a)); data points are shifted by $\pm$ 2 MeV with respect to each other to avoid overlap. For all distributions a polar angle range of the proton $1° < \Theta_p < 11°$ is requested. For details see figure 5.2 and section 5.1.

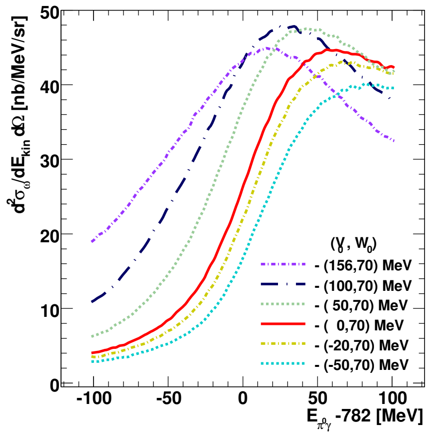

(a) Double differential cross section for ω-production for different real potential depths and an imaginary potential of $W_0(\rho_0)$ = -70 MeV.

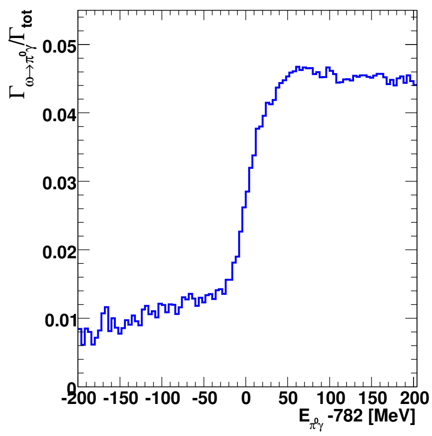

(b) Branching ratio for the decay of bound and quasi-free ω-mesons into the $\pi^0\gamma$-channel, deduced by GiBUU calculations.

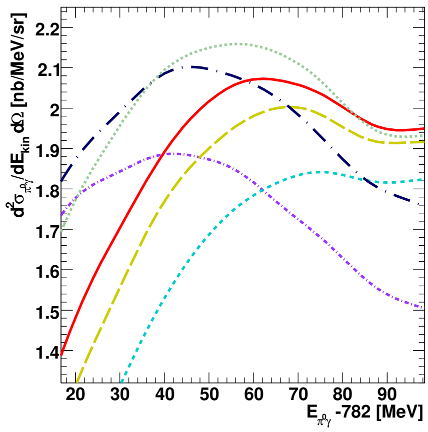

(c) Double differential $\pi^0\gamma$-cross sections derived from (a) by multiplying with (b).

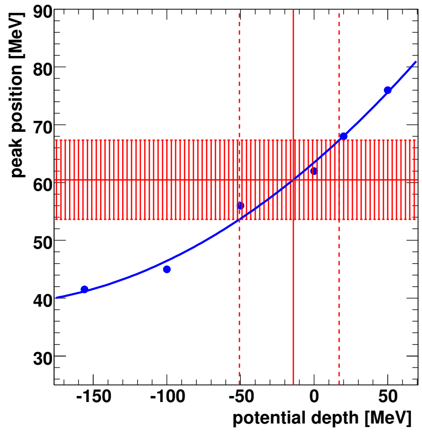

(d) Correlation between the potential depth and the peak position of the total energy distribution (blue points). The blue curve represents a fit. The dashed red area corresponds to the measured peak position, including the error band.

Figure 7.4: Detailed comparison of the predicted cross sections to the experimental data.

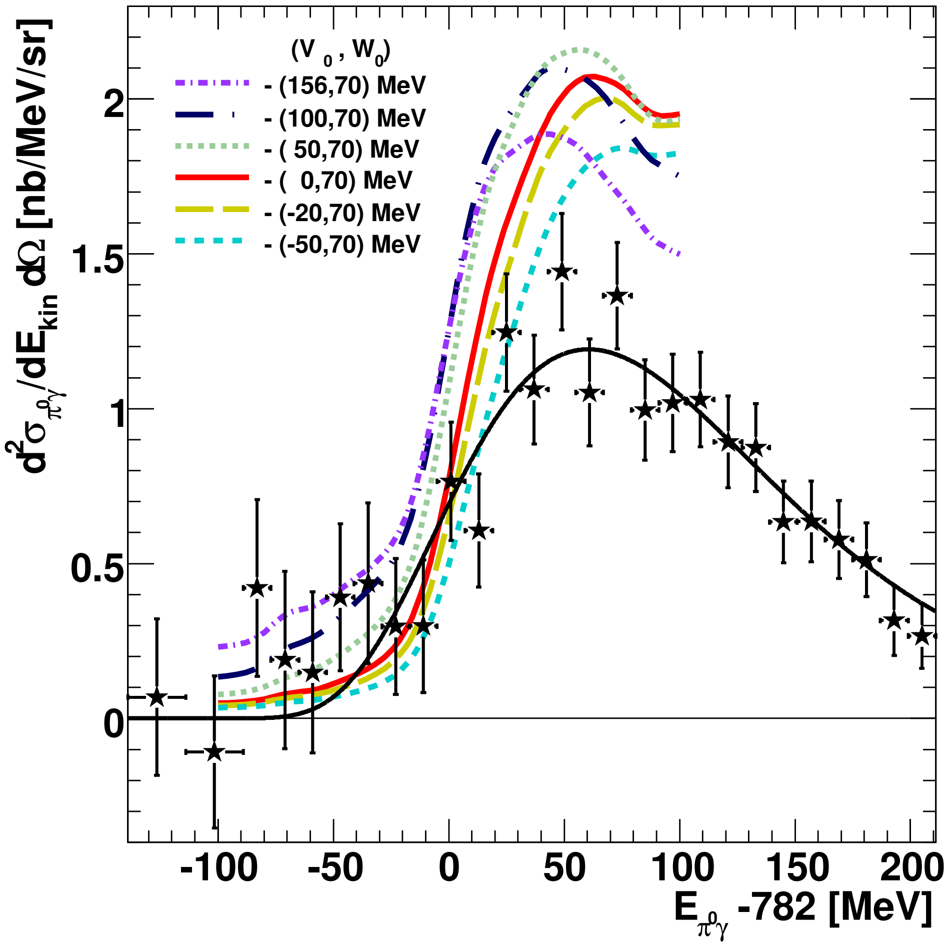

Figure 7.5: Comparison of the predictions by Nagahiro et al. multiplied by the branching ratio of figure 7.4(b) to the carbon data.

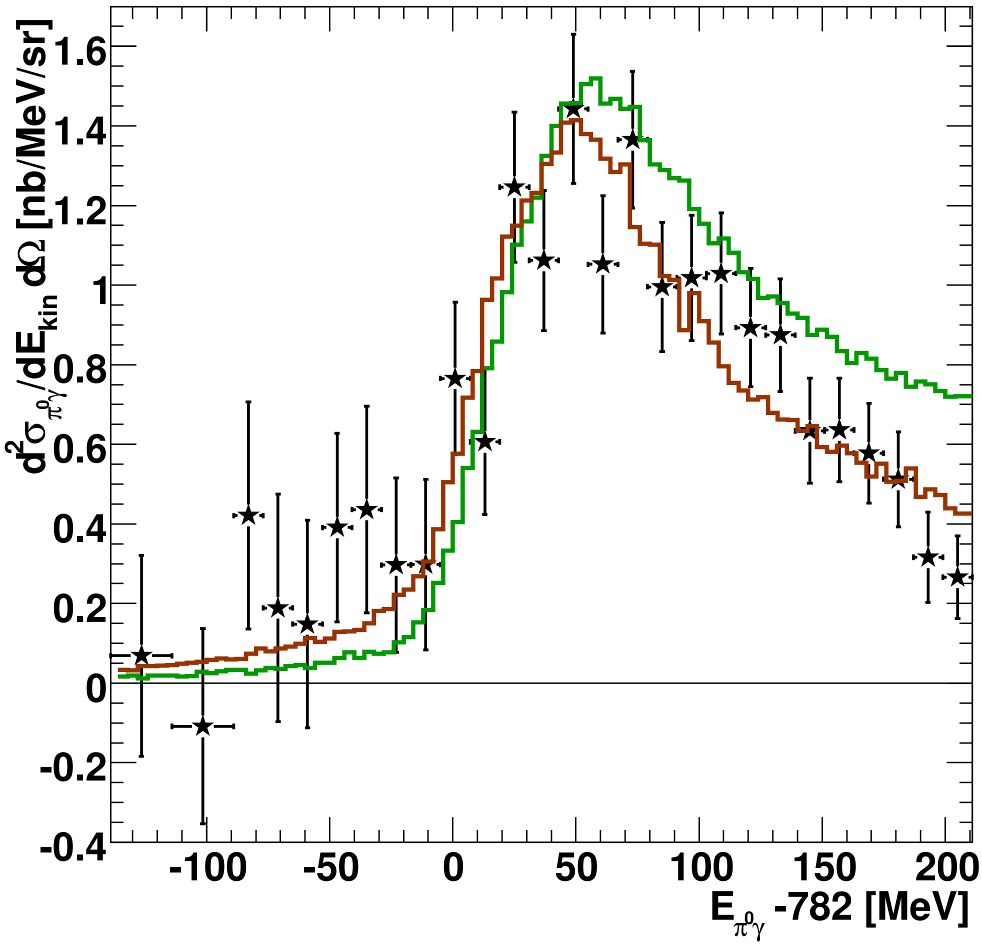

Figure 7.6: Comparison of the GiBUU calculations to the carbon data for two different in-medium modification scenarios (brown histogram: collisional broadening and mass shift of -125 MeV/c^2; green histogram: only collisional broadening with width $\Gamma(\rho = \rho_0)$ = 150 MeV).

of 0.25 nb/MeV/sr is obtained which is comparable to the measured value.

7.2 Systematic uncertainties

The systematic uncertainties for the analysis of the experimental data have various sources. In the following, each of them will be described:

Uncertainty of the background subtraction The background is normalized in momenta bins in regions outside of the ω-signal. Since there are only three momentum bins, a systematic uncertainty is introduced by this method. The estimated error is about 10 to 15%.

Uncertainty of photon flux determination The photon flux determination includes systematic uncertainties due to dead time and saturation effects of the Gamma Intensity Monitor and involved elctronics. Especially for the LH_2 beamtime in October 2008, the detector rates were very high, resulting in inaccuracies in the photon flux determination. An uncertainty of 5 to 10% is estimated.

Uncertainty of the acceptance correction The determination of the acceptance correction derived by a GEANT3 Monte Carlo simulation has a maximum uncertainty of 10%.

Uncertainty of the fits The systematic uncertainty of the fit curve originated in the choice of the function to describe the shape of the data points for the kinetic energy. There is no preferred mathematical function to follow the shape of the data points. Therefore, by varying the fit curve one can determine the stability of the determined maximum value. From that procedure an uncertainty of 10 to 15% can be derived.

Photon shadowing Since a photon has the same quantum numbers as a vector-meson, it can quantum-mechanically fluctuate into a ρ-meson which in turn may interact strongly with nucleons. In that way the effective number of nucleons for interaction with photons is reduced [72]. The effect itself is about 10%,

Source	Size
Background subtraction	$\approx$ 10-15%
Photon flux	5-10%
Acceptance determination	$\lesssim$ 10%
Fits	$\approx$ 10-15%
Photon shadowing	2%
Total	$\approx$ 20%

Table 7.1: Sources of systematic errors.

so that a relative uncertainty of 20% results in a systematic uncertainty of 2%. The relative systematic errors σ_i^{syst} add up quadratically to about 20% in total.

$$\sigma_{total}^{syst} = \sqrt{\sum_i \sigma_i^2} \tag{7.2}$$

Taking these systematic errors into account, the final result for the real part of the ω-nucleus potential is $V_0(\rho_0)$= (-15 $\pm$ 35(stat) $\pm$ 20(syst)) MeV.

Bibliography

[1] **Particle Data Group** Collaboration, J. Beringer *et al.*, "Review of particle physics," *Phys. Rev. D* **86** (July, 2012) 010001. http://link.aps.org/doi/10.1103/PhysRevD.86.010001.

[2] Particle Data Group website. http://pdg.lbl.gov.

[3] B. Povh, K. Rith, C. Scholz, and F. Zetsche, *Teilchen und Kerne*. Springer, 7th ed., June, 2006.

[4] K. Makonyi, *Searching for ω-mesic state in Carbon*. PhD thesis, Justus-Liebig-Universität Gießen, 2011.

[5] S. Klimt, M. Lutz, and W. Weise, "Chiral phase transition in the SU(3) Nambu and Jona-Lasinio model," *Physics Letters B* **249** no. 3-4, (1990) 386–390. http://www.sciencedirect.com/science/article/pii/037026939091003T.

[6] V. Bernard and U. G. Meissner, "Properties of Vector and Axial Vector Mesons from a Generalized Nambu-Jona-Lasinio Model," *Nucl.Phys.* **A489** (1988) 647.

[7] Y. Nambu and G. Jona-Lasinio, "Dynamical Model of Elementary Particles Based on an Analogy with Superconductivity. I," *Phys. Rev.* **122** no. 1, (April, 1961) 345–358.

[8] T. Hatsuda and S. H. Lee, "QCD sum rules for vector mesons in nuclear medium," *Phys.Rev.* **C46** (1992) 34–38.

[9] G. Brown and M. Rho, "Scaling effective Lagrangians in a dense medium," *Phys.Rev.Lett.* **66** (1991) 2720–2723.

[10] K. Saito, K. Tsushima, and A. Thomas, "Nucleon and hadron structure changes in the nuclear medium and the impact on observables," *Progress in Particle and Nuclear Physics* **Volume 58** (2007) 1–167.

[11] M. Lutz, G. Wolf, and B. Friman, "Scattering of vector mesons off nucleons," *Nucl.Phys.* **A706** (2002) 431–496.

[12] **CBELSA/TAPS** Collaboration, M. Kotulla *et al.*, "Modification of the ω-Meson Lifetime in Nuclear Matter," *Phys.Rev.Lett.* **100** (2008) 192302.

[13] D. Cabrera and R. Rapp, "The $\pi\rho$ cloud contribution to the ω width in nuclear matter," *Physics Letters B* **729** (2014) 67–71.

[14] T. Yamazaki, R. Hayano, K. Itahashi, K. Oyama, A. Gillitzer, *et al.*, "Discovery of deeply bound π^- states in the ^{208}Pb(d, ^{3}He) reaction," *Zeitschrift für Physik A Hadrons and Nuclei* **355** no. 3, (1975) 219–221.

[15] K. Itahashi, K. Oyama, R. S. Hayano, H. Gilg, A. Gillitzer, M. Knülle, M. Münch, W. Schott, P. Kienle, H. Geissel, N. Iwasa, G. Münzenberg, S. Hirenzaki, H. Toki, and T. Yamazaki, "Deeply bound π^- states in ^{207}Pb formed in the ^{208}Pb(d,^{3}He) reaction. II. Deduced binding energies and widths and the pion-nucleus interaction," *Phys. Rev. C* **62** (July, 2000) 025202. `http://link.aps.org/doi/10.1103/PhysRevC.62.025202`.

[16] K. Suzuki *et al.*, "Precision Spectroscopy of Pionic 1s States of Sn Nuclei and Evidence for Partial Restoration of Chiral Symmetry in the Nuclear Medium," *Phys. Rev. Lett.* **92** (February, 2004) 072302. `http://link.aps.org/doi/10.1103/PhysRevLett.92.072302`.

[17] R. S. Hayano and T. Hatsuda, "Hadron properties in the nuclear medium," *Rev. Mod. Phys.* **82** (Oct, 2010) 2949–2990. `http://link.aps.org/doi/10.1103/RevModPhys.82.2949`.

[18] H. Nagahiro, D. Jido, and S. Hirenzaki, "Formation of mesic nuclei by (γ,p) reactions," *Nuclear Physics A* **761** no. 1-2, (2005) 92–119. `http://www.sciencedirect.com/science/article/pii/S0375947405009899`.

[19] E. Marco and W. Weise, "Photoproduction of quasi-bound ω-mesons in nuclei," *Physics Letters B* **502** no. 1-4, (2001) 59–62. `http://www.sciencedirect.com/science/article/pii/S0370269301001885`.

[20] O. Morimatsu and K. Yazaki, "The formation probabilities of Σ-hypernuclei and the "unstable bound state"," *Nuclear Physics A* **435** no. 3-4, (1985) 727–737.

[21] O. Morimatsu and K. Yazaki, "A study on the formation of Σ-hypernuclei by $(\bar{K}, \pi)$ reaction," *Nuclear Physics A* **483** no. 3-4, (1988) 493–513.

[22] H. Nagahiro. Private communications, 2013.

[23] H. Nagahiro, M. Takizawa, and S. Hirenzaki, "η- and η'-mesic nuclei and $\mathrm{U}_A(1)$ anomaly at finite density," *Phys. Rev. C* **74** (Oct, 2006) 045203.

[24] B. Krusche, "Photoproduction of π^0 and η mesons from nucleons and nuclei in the second resonance region." Habilitation, 1995.

[25] W. Hillert, "The Bonn electron stretcher accelerator ELSA: Past and future," *Eur. Phys. J.* **A28S1** (2006) 139–148.

[26] D. Walther. Private communications, 2010.

[27] K. Fornet-Ponse, *Die Photonenmarkierungsanlage für das Crystal-Barrel/TAPS-Experiment an ELSA*. PhD thesis, Universität Bonn, PI, 2009.

[28] M. Grüner, "Modifikation und Test des Innendetektors für das Crystal Barrel Experiment," Master's thesis, Universität Bonn, HISKP, 2006.

[29] D. Elsner, *Untersuchung kleiner Partialwellenbeiträge in der Nähe dominierender Resonanzzustände des Protons mit linear polarisierten Photonen*. PhD thesis, Universität Bonn, PI, 2007.

[30] **CBELSA/TAPS** Collaboration, C. Wendel, "The Crystal-Barrel/TAPS experiment at ELSA: Current status of the CsI(Tl) calorimeters," *J. Phys. Conf. Ser.* **160** (2009) 012006.

[31] E. Aker *et al.*, "The Crystal Barrel spectrometer at LEAR," *Nuclear Instruments and Methods in Physics Research A* **321** (1992) 69.

[32] I. Horn, *The decay of the γ p system into the $p\pi^0\eta$ final state*. PhD thesis, Universität Bonn, 2005.

[33] D. Trnka, *Investigation of in-medium modifications of the ω meson in photonuclear reactions*. PhD thesis, Justus-Liebig-Universität Gießen, 2006.

[34] A. R. Gabler *et al.*, "Response of TAPS to monochromatic photons with energies between 45 MeV and 790 MeV," *Nucl. Instrum. Meth.* **A346** (1994) 168–176.

[35] **TAPS** Collaboration, R. Novotny, "The BaF_2 Photon Spectrometer TAPS," April, 1991. IEEE transactions on nuclear science.

[36] **Particle Data Group** Collaboration, C. Amsler *et al.*, "Review of particle physics," *Phys. Lett. B* **667** (July, 2008) 1.

[37] P. Drexler, *Entwicklung und Aufbau der neuen TAPS-Elektronik*. PhD thesis, Justus-Liebig-Universität Gießen, 2004.

[38] M. Kotulla. Private communications, 2008.

[39] S. Materne, "Ein Aerogel-Čerenkov-Detektor für das CBELSA/TAPS-Experiment," Master's thesis, Universität Bonn, PI, 2007.

[40] S. Friedrich, "Teilchenidentifikation mittels Čerenkov- und Szintillationsdetektoren," Master's thesis, Justus-Liebig-Universität Gießen, 2007.

[41] M. Ayers and A. Hunt, "History of Silica Aerogels." Lawrence Berkeley National Laboratory website. `http://eande.lbl.gov/ECS/Aerogels`.

[42] E. Nappi *et al.*, "Aerogel and its applications to RICH detectors." SLAC National Accelerator Laboratory website. `http://www.slac.stanford.edu/pubs/icfa/fall98/paper3`.

[43] J. Bähr *et al.*, "Silica aerogel radiators for bunch length measurements,"

Nuclear Instruments and Methods in Physics Research A **538** (2005) 597 – 607.

[44] T. Kuske. Private communications, 2008.

[45] C. Schmidt *et al.* CBNote in preparation, 2014.

[46] R. Brun and F. Rademakers, "Root - an object oriented data analysis framework," *Nuclear Instruments and Methods in Physics Research Section A: Accelerators, Spectrometers, Detectors and Associated Equipment* **389** no. 1-2, (1997) 81–86. `http://www.sciencedirect.com/science/article/pii/S016890029700048X`.

[47] J. Hartmann, "Zeitkalibrierung und Photonenflussbestimmung für das Crystal-Barrel-Experiment an ELSA," Master's thesis, Universität Bonn, HISKP, 2008.

[48] M. E. Robig, "Eichung des TAPS-Detektorsystems mit Höhenstrahlung," Master's thesis, Justus-Liebig-Universität Gießen, 1991.

[49] R. Castelijns, *Photoproduction of strange mesons and hyperons on the proton*. PhD thesis, Rijksuniversiteit Groningen, 2006.

[50] T. Seifen, "Verbesserung der Rekonstruktion und Entwicklung eines First-Level-Triggerschemas für das Crystal-Barrel-Kalorimeter," Master's thesis, Universität Bonn, HISKP, 2009.

[51] T. Seifen. Private communications, 2010.

[52] T. C. Awes *et al.*, "A simple method of shower localization and identification in laterally segmented calorimeters," *Nuclear Instruments and Methods in Physics Research A* **311** (January, 1992) 130–138.

[53] K. Molenaar, "Performance of TAPS in the Tagged Photon Beam of MAMI," Master's thesis, Rijksuniversiteit Groningen, 1992.

[54] P. D. Strother, *Design and application of the reconstruction software for the BaBar calorimeter*. PhD thesis, London, 1998.

[55] **BABAR** Collaboration, B. Aubert *et al.*, "Measurement of branching fractions,

and CP and isospin asymmetries, for $B \to K^*\gamma$," *Phys. Rev.* **D70** (2004) 112006.

[56] J. Junkersfeld, *Photoproduktion von $\pi^0\omega$ am Proton bei Energien bis zu 3 GeV*. PhD thesis, Universität Bonn, HISKP, 2005.

[57] M. Kaskulov, H. Nagahiro, S. Hirenzaki, and E. Oset, "Possible ω bound states in nuclei produced with the (γ,p) reaction," *Phys.Rev.* **C75** (2007) 064616.

[58] J. Messchendorp, A. Sibirtsev, W. Cassing, V. Metag, and S. Schadmand, "Studying the ω mass in-medium in $\gamma + A \to \pi^0\gamma + X$ reactions," *Eur.Phys.J.* **A11** (2001) 95–103.

[59] J. E. Gaiser, *Charmonium spectroscopy from radiative decays of the J/ψ and ψ', SLAC-R-255*. PhD thesis, Stanford Linear Accelator Center, Stanford University, 1982.

[60] J. Barth *et al.*, "Low-energy photoproduction of ω-mesons," *The European Physical Journal A - Hadrons and Nuclei* **18** no. 1, (2003) 117–127. `http://dx.doi.org/10.1140/epja/i2003-10061-y`.

[61] GiBUU website. `https://gibuu.hepforge.org/trac/wiki`.

[62] O. Buss, T. Gaitanos, K. Gallmeister, H. van Hees, M. Kaskulov, O. Lalakulich, A. Larionov, T. Leitner, J. Weil, and U. Mosel, "Transport-theoretical description of nuclear reactions," *Physics Reports* **512** no. 1-2, (2012) 1–124. `http://www.sciencedirect.com/science/article/pii/S0370157311003619`.

[63] J. Weil, *Vector Mesons in Medium in a Transport Approach*. PhD thesis, Justus-Liebig-Universität Gießen, 2013.

[64] J. Weil, "Dilepton Production in Elementary Nuclear Reactions within a BUU Transport Model," Master's thesis, Justus-Liebig-Universität Gießen, 2008.

[65] J. Lehr, *In-medium Eigenschaften von Nukleonen und Nukleonresonanzen in einem semiklassischen Transportmodell*. PhD thesis, Justus-Liebig-Universität Gießen, 2003.

[66] M. Effenberger, *Eigenschaften von Hadronen in Kernmaterie in einem vereinheitlichten Transportmodell*. PhD thesis, Justus-Liebig-Universität Gießen, 1999.

[67] L. Kadanoff and G. Baym, *Quantum Statistical Mechanics*. Addison Wesley, 1994.

[68] **A2** Collaboration, M. Thiel *et al.*, "In-medium modifications of the ω meson near the production threshold," *Eur. Phys. J. A* **49** (2013) 132.

[69] **BGO-OD** Collaboration, V. Metag, "Search for η'-mesic states at BGO-OD." approved proposal ELSA/03-2012-BGO-OD, 2012.

[70] **CBELSA/TAPS** Collaboration, M. Nanova *et al.*, "Determination of the η'-nucleus optical potential," *Physics Letters B* **727** no. 4-5, (2013) 417–423. `http://www.sciencedirect.com/science/article/pii/S0370269313008691`.

[71] H. Nagahiro, D. Jido, H. Fujioka, K. Itahashi, and S. Hirenzaki, "Formation of η'(958)-mesic nuclei by the (p,d) reaction," *Phys. Rev. C* **87** (April, 2013) 045201. `http://link.aps.org/doi/10.1103/PhysRevC.87.045201`.

[72] N. Bianchi, V. Muccifora, *et al.*, "Total hadronic photoabsorption cross section on nuclei in the nucleon resonance region," *Phys. Rev. C* **54** (Oct, 1996) 1688–1699. `http://link.aps.org/doi/10.1103/PhysRevC.54.1688`.

[73] P. Drexler. Private communications, 2009.

Appendix A

List of abbreviations

Abbreviation	Meaning
ADC	**A**nalog-to-**D**igital-**C**onverter
BUU equation	**B**oltzmann-**U**ehling-**U**hlenbeck equation
CB	**C**rystal **B**arrel
CFD	**C**onstant **F**raction **D**iscriminator
CM	**C**enter-of-**M**ass
DAQ	**D**ata **Acq**uisition
ELSA	**El**ektronen-**S**tretcher-**A**nlage
FACE	**Fa**st **C**luster **E**ncoder
FSI	**F**inal **S**tate **I**nteraction
FWHM	**F**ull **W**idth at **H**alf **M**aximum
FwPlug	**F**or**w**ard **Plug**
GEANT	**Ge**ometry **an**d **T**racking
GiBUU	**Gi**essen **B**oltzmann-**U**ehling-**U**hlenbeck transport model
GIM	**G**amma **I**ntensity **M**onitor

Abbreviation	Meaning
LED	**L**eading **E**dge **D**iscriminator
LH_2	**L**iquid **H**ydrogen
MC	**M**onte **C**arlo
MiniTAPS	Mini **T**wo **A**rm **P**hoto-**S**pectrometer
NJL model	**N**ambu and **J**ona-**L**asinio model
PDG	**P**article **D**ata **G**roup
PED	**P**article **E**nergy **D**eposit
QCD	**Q**uantum **C**hromo**D**ynamics
QDC	**C**harge-to-**D**igital-**C**onverter
QED	**Q**uantum **E**lectro**D**ynamics
QMC model	**Q**uark-**M**eson **C**oupling model
TDC	**T**ime-to-**D**igital-**C**onverter
TOF	**T**ime-**o**f-**F**light

Appendix B

Theoretical calculations

The figures in this section of the appendix show the results of calculations of the ω-kinetic energy by H. Nagahiro [22] for different incident photon energies and specific angles of the coincident proton.

Figure B.1: Calculated spectra of the ^{12}C(γ,p) reactions for the ω-mesic nucleus formation as function of the kinetic energy of the ω-meson for three different energies and three different angles of the outgoing proton for a potential of (V_0, W_0) = (-100, 70) MeV. Individual states are indicated by the colored lines. The sum is drawn in black. [22]

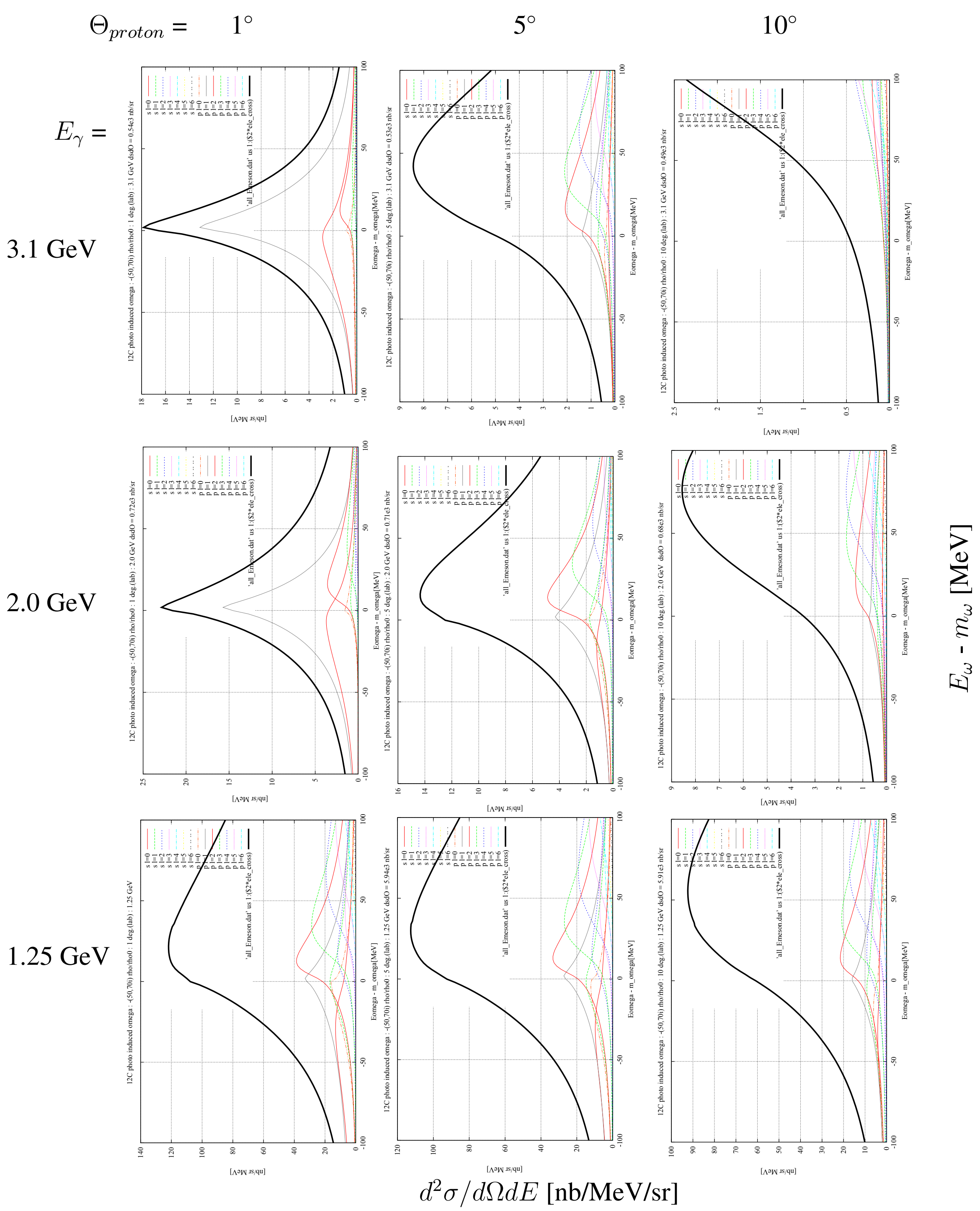

Figure B.2: Calculated spectra of the ^{12}C(γ,p) reactions for the ω-mesic nucleus formation as function of the kinetic energy of the ω-meson for three different energies and three different angles of the outgoing proton for a potential of (V_0, W_0) = (-50, 70) MeV. Individual states are indicated by the colored lines. The sum is drawn in black. [22]

Θ_{proton} = 1° 5° 10°

E_γ =

3.1 GeV

2.0 GeV

1.25 GeV

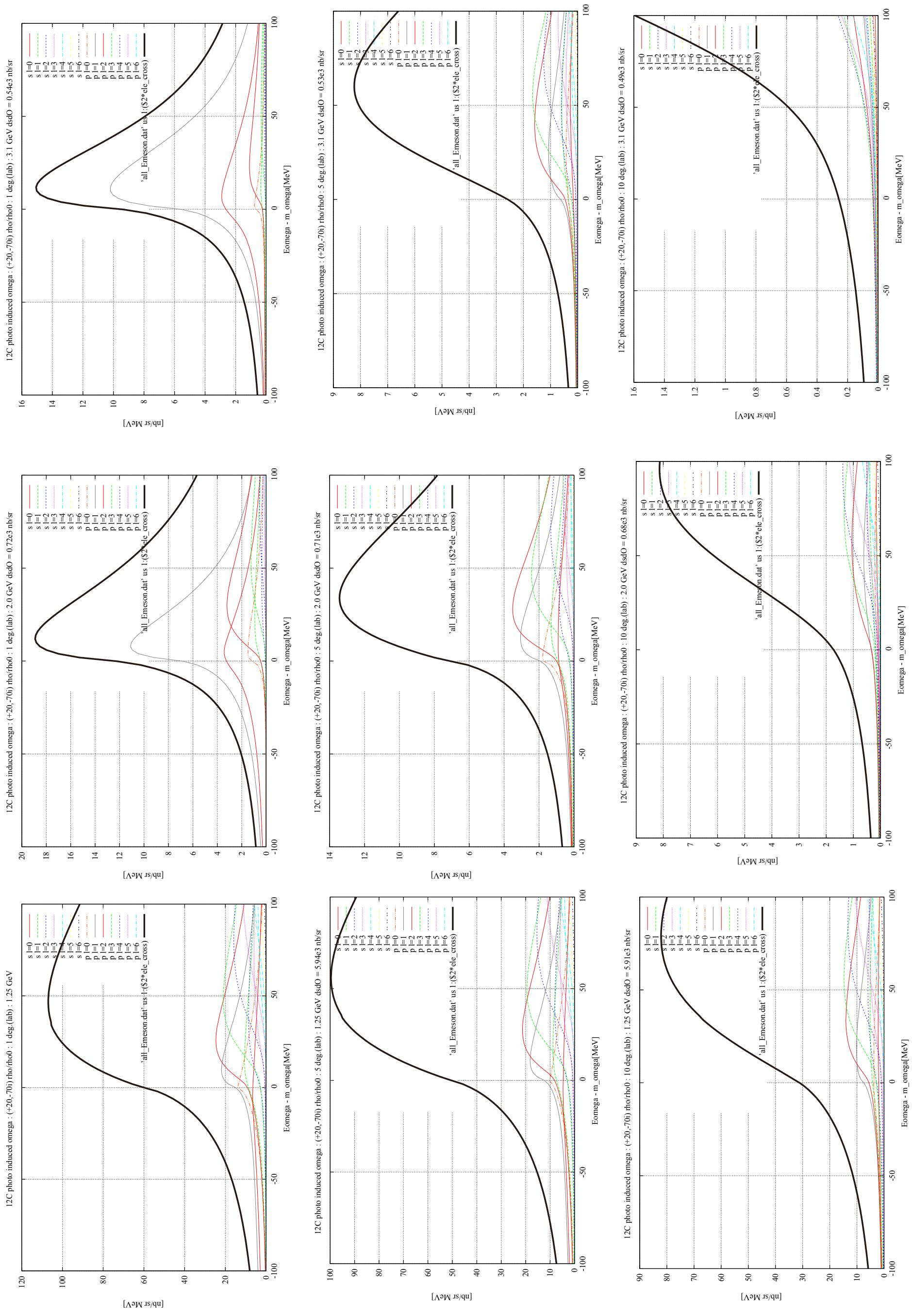

E_ω - m_ω [MeV]

$d^2\sigma/d\Omega dE$ [nb/MeV/sr]

Figure B.3: Calculated spectra of the ^{12}C(γ,p) reactions for the ω-mesic nucleus formation as function of the kinetic energy of the ω-meson for three different energies and three different angles of the outgoing proton for a potential of (V_0, W_0) = (+20, 70) MeV. Individual states are indicated by the colored lines. The sum is drawn in black. [22]

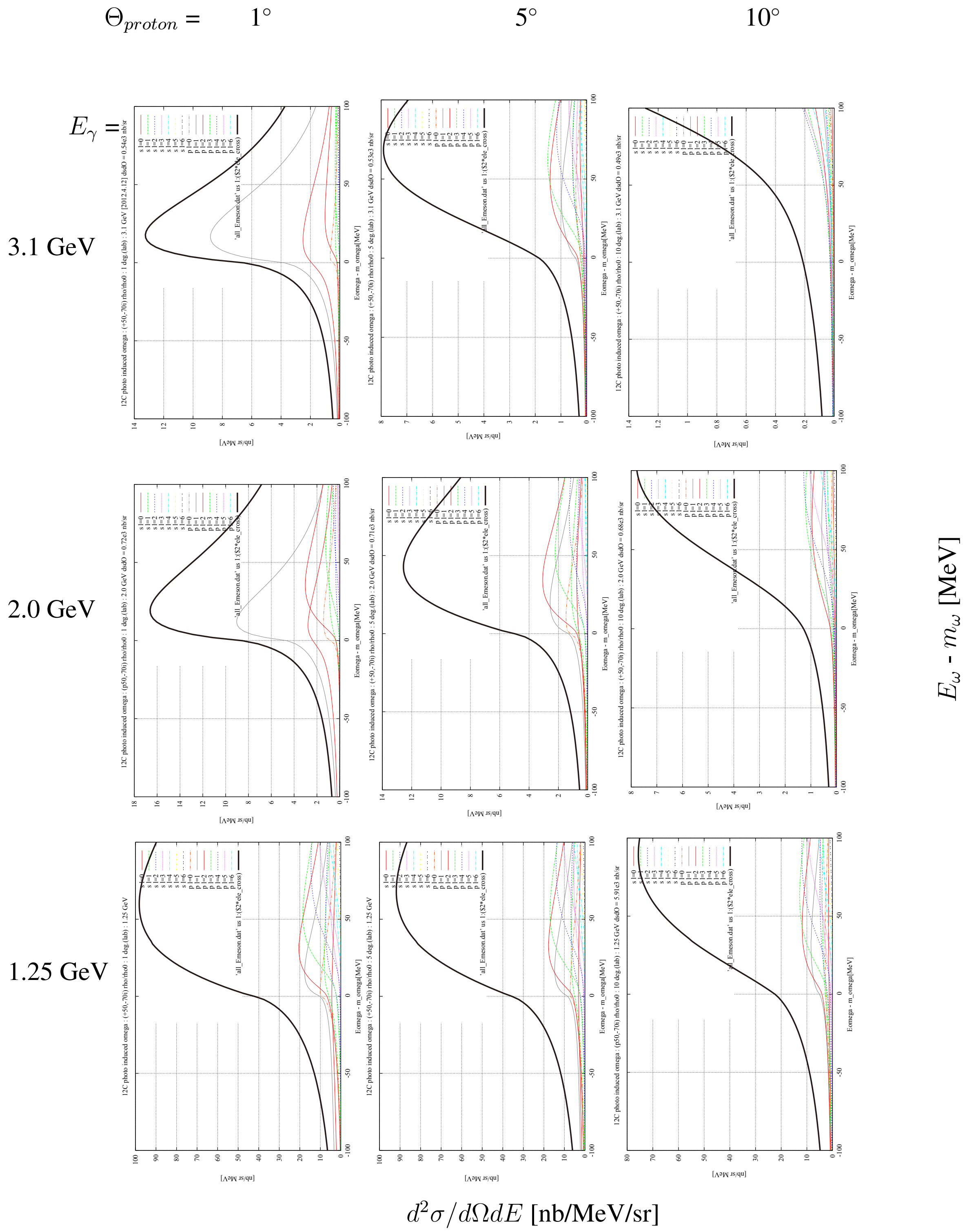

Figure B.4: Calculated spectra of the ^{12}C(γ,p) reactions for the ω-mesic nucleus formation as function of the kinetic energy of the ω-meson for three different energies and three different angles of the outgoing proton for a potential of (V_0, W_0) = (+50, 70) MeV. Individual states are indicated by the colored lines. The sum is drawn in black. [22]

Appendix C

Trigger scheme of the MiniTAPS detector

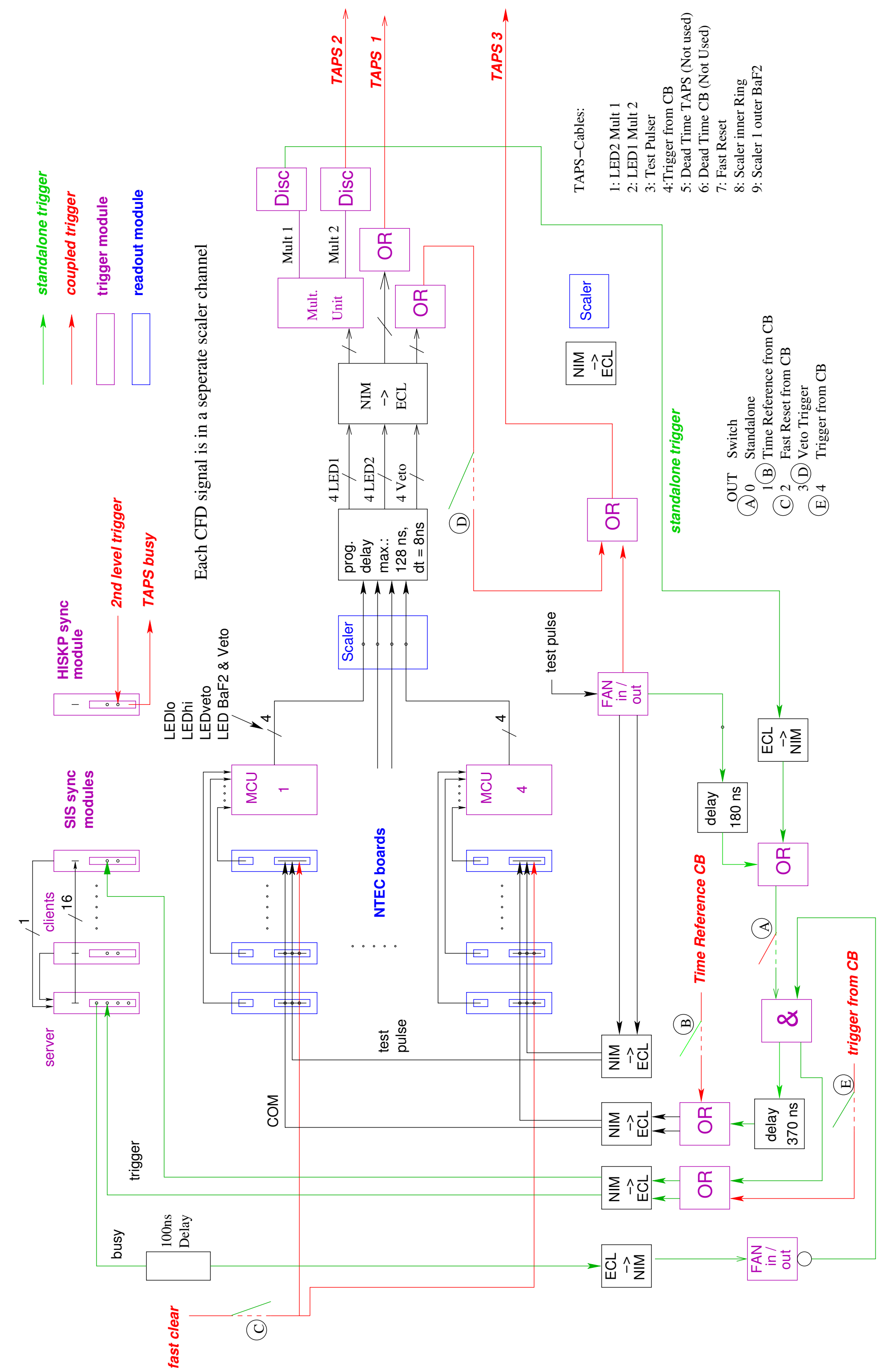

Figure C.1: Trigger scheme of the MiniTAPS detector [73].

Appendix D

Trigger conditions

The following tables list the trigger conditions for the different beamtimes.

(a)

omega_prime = carbon_omega_prime		
1st level		FACE
Tagger &	MiniTAPS (LED 1)	>=2
	FwPlug2 & MiniTAPS (LED 1)	>=0
	FwPlug1 & MiniTAPS (LED 1)	>=1
	FwPlug2	>=1
	FwPlug1	>=2

(b)

omega = carbon_omega_prime		
1st level		FACE
Tagger &	MiniTAPS (LED 1)	>=3
	FwPlug2 & MiniTAPS (LED 1)	>=1
	FwPlug1 & MiniTAPS (LED 1)	>=2
	FwPlug2	>=2
	FwPlug1	>=3

(c)

trig41		
1st level		FACE
Tagger &	Inner Detector	>=2
	Inner Detector& MiniTAPS (LED 1)	>=1
	FwPlug1 & MiniTAPS (LED 1)	bypass
	FwPlug2	bypass
	FwPlug1	>=1

(d)

trig42c		
1st level		FACE
Tagger &	Inner Detector& !Čerenkov	>=2
	MiniTAPS (LED 1) & !Čerenkov	>=1
	FwPlug1 & MiniTAPS(LED 1) & !Čerenkov	bypass
	FwPlug2 & !Čerenkov	bypass
	FwPlug1& !Čerenkov	>=1
	MiniTAPS (LED 2) & !Čerenkov	bypass

Table D.1: Trigger conditions used in LH_2 and carbon beamtimes: (a) Three-particle trigger, (b) four-particle trigger, (c) two-particle trigger, (d) two-particle trigger with gas-Čerenkov detector as hardware veto.

(a)

eta4nc		
1st level		FACE
Tagger &	MiniTAPS (LED 1)	>=3
	FwPlug2 & MiniTAPS (LED 1)	>=1
	FwPlug1 & MiniTAPS (LED 1)	>=2
	FwPlug2	>=2
	FwPlug1	>=3
	MiniTAPS (LED 2)	>=2
	FwPlug1 & MiniTAPS (LED 2)	>=1
	FwPlug2 & MiniTAPS (LED 2)	bypass

(b)

eta4		
1st level		FACE
Tagger &	MiniTAPS (LED 1) & !Čerenkov	>=3
	FwPlug2 & MiniTAPS (LED 1)& !Čerenkov	>=1
	FwPlug1 & MiniTAPS (LED 1) & !Čerenkov	>=2
	FwPlug2 & !Čerenkov	>=2
	FwPlug1 & !Čerenkov	>=3
	MiniTAPS (LED 2)& !Čerenkov	>=2
	FwPlug1 & MiniTAPS (LED 2)& !Čerenkov	>=1
	FwPlug2 & MiniTAPS (LED 2) & !Čerenkov	bypass

Table D.2: Trigger conditions used only during carbon beamtime (January 2009): (a) Four-particle trigger, (b) four-particle trigger with aerogel-Čerenkov detector as hardware veto.

Appendix E

Energy calibration

The following figures show control spectra for the energy calibration of the Crystal Barrel and the MiniTAPS detectors for the LH_2 beamtime (October 2008).

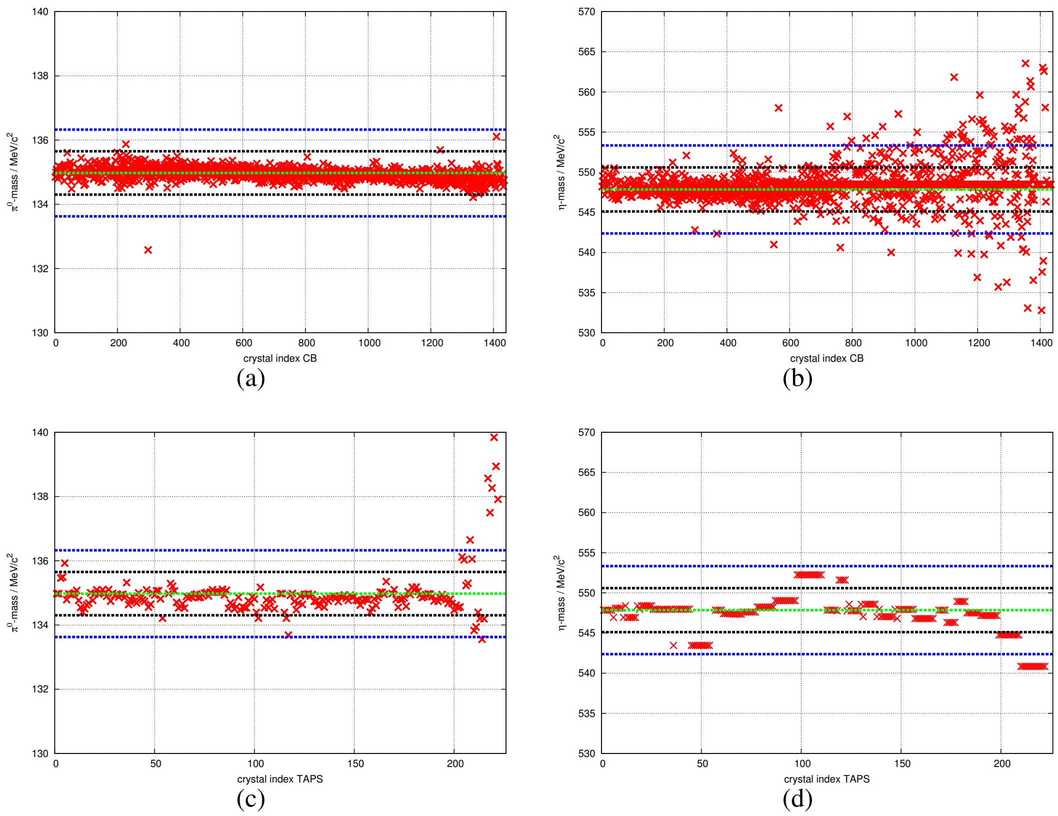

Figure E.1: Energy calibration check for each crystal (LH_2 beamtime, October 2008). For figures (a) and (b) the index range between 1 and 180 refers to the FwPlug. Green lines show the position of the nominal masses of the meson. The other lines show relative deviations: 0.5 % (black) and 1.0% (blue).
(a) and (b): Reconstructed π^0-/η-invariant mass for two photons in CB + FwPlug.
(c) and (d): Reconstructed π^0-/η-invariant mass for one photon in CB + FwPlug and one photon in MiniTAPS. Except for the inner most crystals in MiniTAPS, most crystals are calibrated within 1.0% relative deviation of the meson mass. Please note that for (d) the MiniTAPS crystals are calibrated ringwise due to low statistics.

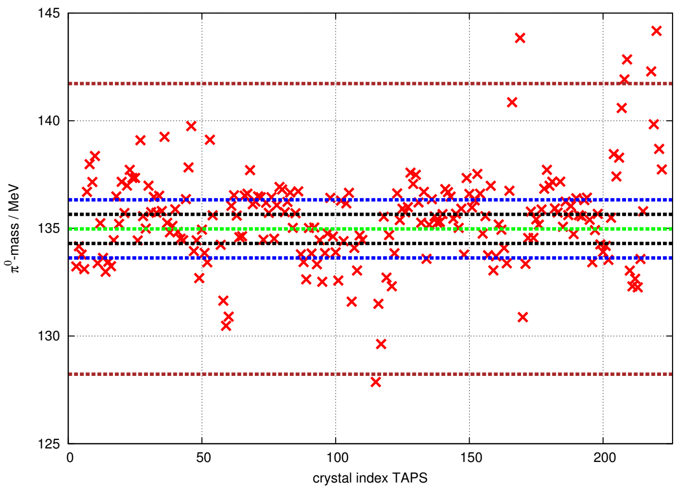

Figure E.2: Reconstructed π^0-invariant mass for two photons in MiniTAPS (LH_2 beamtime, October 2008). The green line shows the position of the nominal pion mass. The other lines show relative deviations: 0.5 % (black), 1.0% (blue) and 5.0% (brown).
Almost all crystals are calibrated within 5.0% relative deviation of the pion mass.

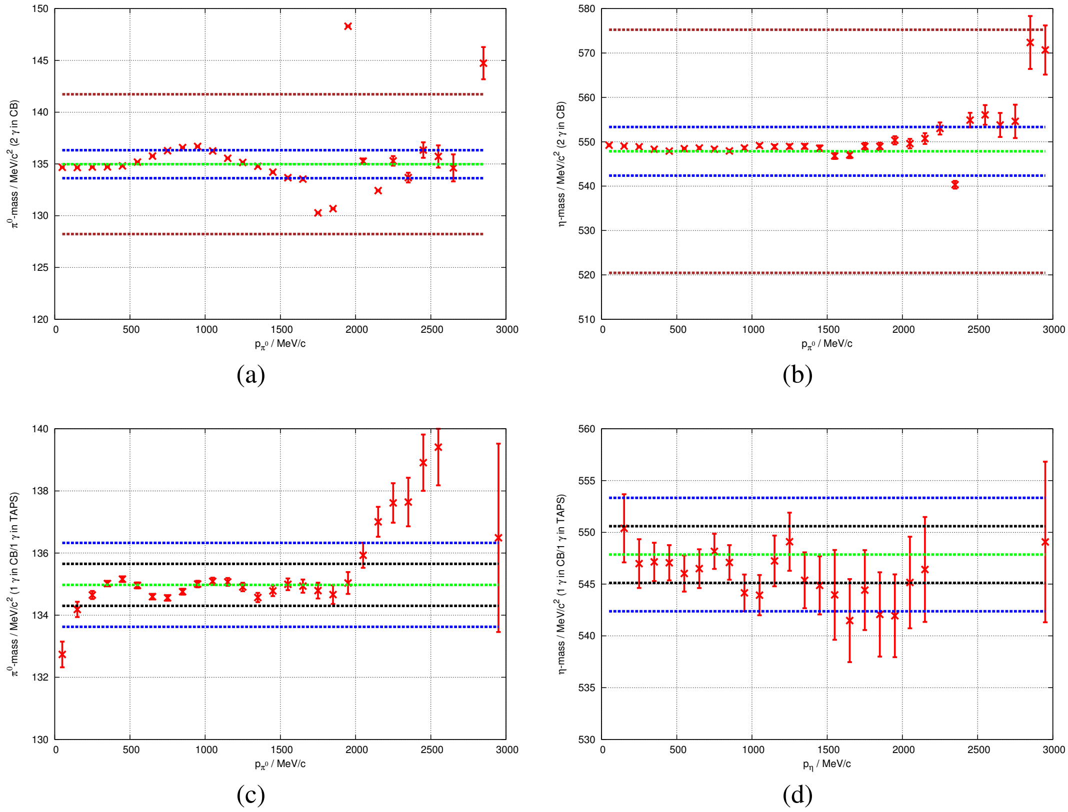

Figure E.3: Reconstructed π^0-/η-invariant mass as function of the reconstructed meson momentum (LH_2 beamtime, October 2008). Green lines show the position of the nominal meson masses. The other lines show relative deviations: 0.5 % (black) and 1.0% (blue).
(a) and (b): Reconstructed π^0-/η-invariant mass for two photons in CB + FwPlug.
(c) and (d): Reconstructed π^0-/η-invariant mass for one photon in CB + FwPlug and one photon in MiniTAPS.
The invariant masses are stable within $\pm 1.5\%$ in the momentum range of 100 MeV/c < $p_{\gamma\gamma}$ < 1700 MeV/c.

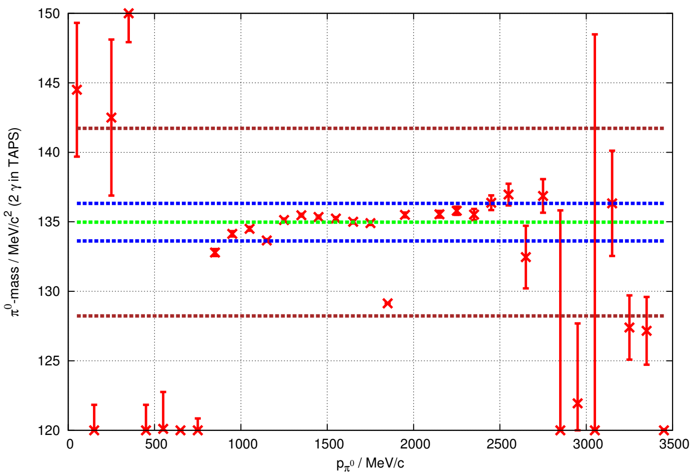

Figure E.4: Invariant mass of π^0-mesons as a function of their momenta for two photons in MiniTAPS (LH_2 beamtime, October 2008). The error bars show the fitting error of the peak position. The green line shows the position of the nominal pion mass. The other lines show relative deviations: 0.5 % (black) and 1.0% (blue).
The invariant masses are stable within $\pm 1.5\%$ in the momentum range of 900 MeV/c < $p_{\gamma\gamma}$ < 2500 MeV/c.

Appendix F

Acceptance simulations

The follwoing figures show simulations for the acceptance of $\pi^0\gamma$-pairs with a coincident proton in MiniTAPS ($1° < \Theta_{proton} < 11°$). The Fermi motion of nucleons as well as the geometry of the detector system and the detector response are taken into account (see section 5.2).

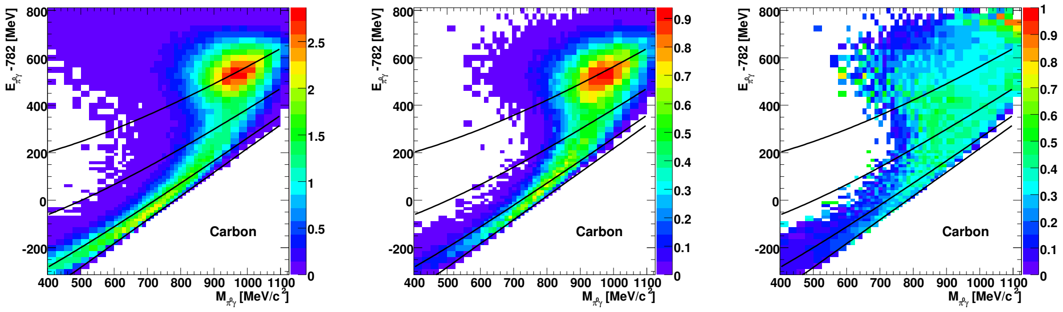

(a) Start distribution. (b) Reconstructed distribution. (c) Acceptance.

Figure F.1: $\pi^0\gamma$-simulation for E_γ = 1450 - 1650 MeV on carbon.

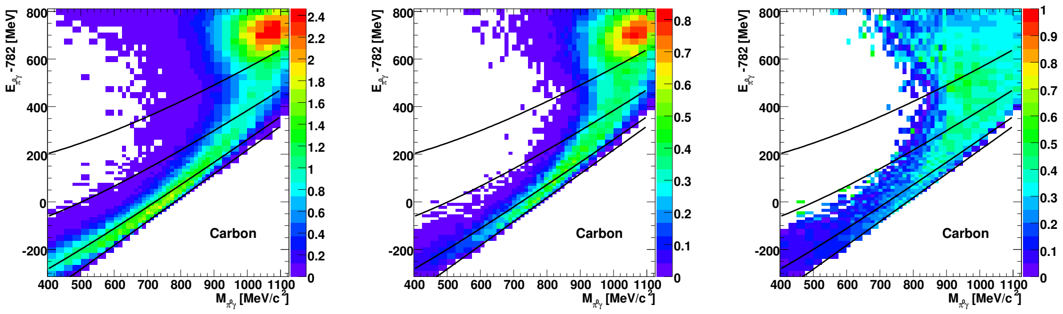

(a) Start distribution. (b) Reconstructed distribution. (c) Acceptance.

Figure F.2: $\pi^0\gamma$-simulation for E_γ = 1650 - 1850 MeV on carbon.

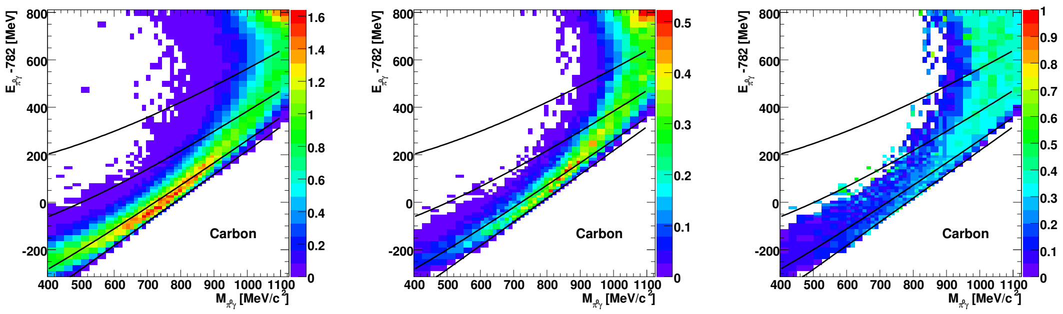

(a) Start distribution. (b) Reconstructed distribution. (c) Acceptance.

Figure F.3: $\pi^0\gamma$-simulation for E_γ = 1850 - 2050 MeV on carbon.

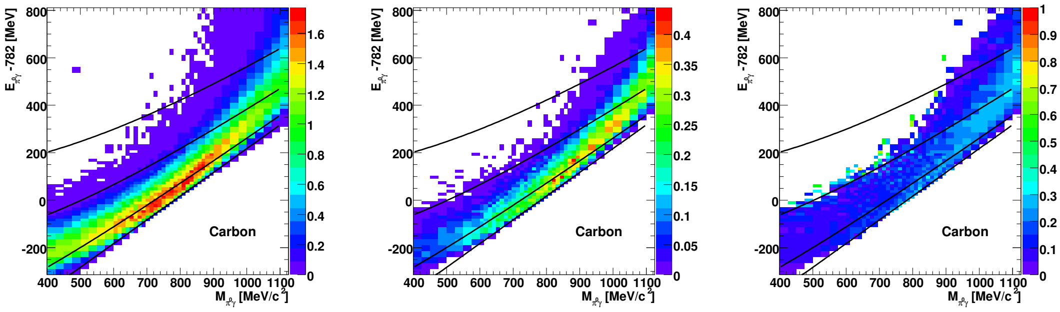

(a) Start distribution. (b) Reconstructed distribution. (c) Acceptance.

Figure F.4: $\pi^0\gamma$-simulation for E_γ = 2250 - 2450 MeV on carbon.

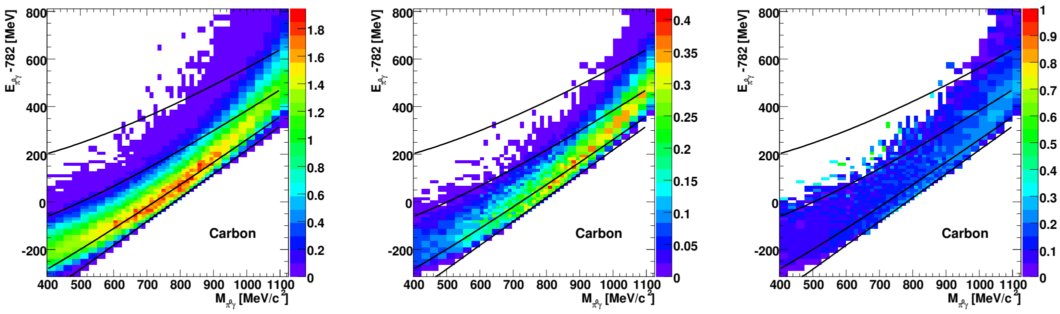

(a) Start distribution. (b) Reconstructed distribution. (c) Acceptance.

Figure F.5: $\pi^0\gamma$-simulation for E_γ = 2450 - 2650 MeV on carbon.

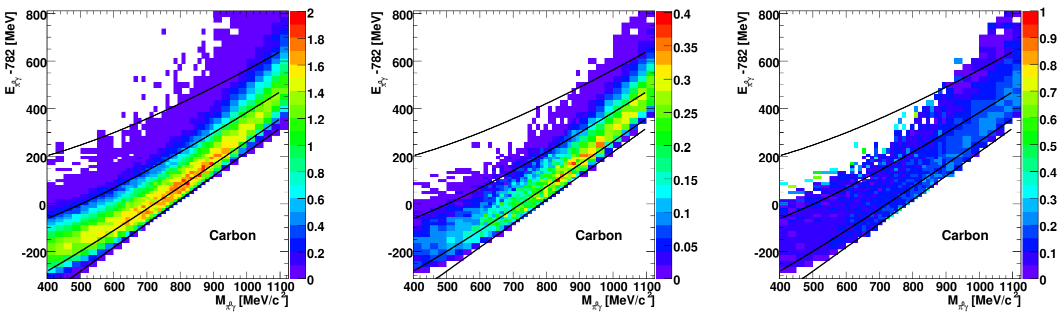

(a) Start distribution. (b) Reconstructed distribution. (c) Acceptance.

Figure F.6: $\pi^0\gamma$-simulation for E_γ = 2650 - 2850 MeV on carbon.

Danksagung

Mein Dank gilt an erster Stelle all denen, die es mir ermöglicht haben, diese Dissertation zu verfassen. Das angenehme Miteinander in der gesamten Arbeitsgruppe war ein Schlüssel zum Erfolg. Vielen Dank!
Meinem Betreuer Prof. Dr. Volker Metag möchte ich meinen Dank für die Bereitstellung dieser Arbeit aussprechen; es warteten immer neue Herausforderungen auf mich, die es zu bewältigen galt und mich im positiven Sinne forderten und förderten.
Des Weiteren möchte ich mich bei Karoly bedanken, der für die vielen aufkommenden (Software-)Fragen stets die Antworten finden musste, und dies auch bereitwillig tat sowie für seine immer neuen Ideen zur Herangehensweise an auftauchende Probleme. Ohne seine Hilfe wäre vieles schwieriger gewesen.
Ich bedanke mich bei Uli und Peter für die Unterstützung bei der Wartung der TAPS-Boards im Besonderen und bei Fragen zu Elektronik im Allgemeinen.
Bei Janus möchte ich mich für die fortlaufende Unterstützung bei allen GiBUU-Simulationen bedanken; ohne seine Bereitschaft, neue Funktionen zu implementieren und mir zugänglich zu machen, hätte ich GiBUU nicht nutzen können.
Daniel danke ich für das Korrekturlesen der gesamten Arbeit und seiner Geduld, mir alle Fragen zu diversen Programmierproblemen zu beantworten.
Zum Schluss möchte ich meiner Freundin Aleksandra danken, dass sie mir in der recht anstrengenden Zeit zur Seite stand sowie für all die anderen großen und kleinen Dinge.

Erklärung

Ich erkläre: Ich habe die vorgelegte Dissertation selbständig und ohne unerlaubte fremde Hilfe und nur mit den Hilfen angefertigt, die ich in der Dissertation angegeben habe.
Alle Textstellen, die wörtlich oder sinngemäß aus veröffentlichten Schriften entnommen sind, und alle Angaben, die auf mündlichen Auskünften beruhen, sind als solche kenntlich gemacht.
Bei den von mir durchgeführten und in der Dissertation erwähnten Untersuchungen habe ich die Grundsätze guter wissenschaftlicher Praxis, wie sie in der "Satzung der Justus-Liebig-Universität Gießen zur Sicherung guter wissenschaftlicher Praxis" niedergelegt sind, eingehalten.

Stefan Friedrich
Gießen, Juni 2014